2018

Understanding Early Amyloid-ß Aggregation to Engineer Polyacid-Functionalized Nanoparticles as an Inhibitor Design Platform

Nicholas Vander Munnik
University of South Carolina

Understanding Early Amyloid-β Aggregation to Engineer Polyacid-Functionalized Nanoparticles as an Inhibitor Design Platform

by

Nicholas Van der Munnik

Bachelor of Science
Clarkson University 2013

Submitted in Partial Fulfillment of the Requirements

for the Degree of Doctor of Philosophy in

Chemical Engineering

College of Engineering and Computing

University of South Carolina

2018

Accepted by:

Mark J. Uline, Major Professor

Melissa A. Moss, Major Professor

Jochen Lauterbach, Committee Member

Andrew Greytak, Committee Member

John Weidner, Committee Member

Cheryl L. Addy, Vice Provost and Dean of the Graduate School

Abstract

Alzheimer's disease (AD) is characterized by the presence of amyloid-β (Aβ) protein aggregates in the brains of those afflicted. This protein aggregates via a complex pathway to progress from monomers to soluble oligomers and ultimately insoluble fibrils. Due to the dynamic nature of aggregation, it has proven exceedingly difficult to determine the precise interactions that lead to the formation of transient oligomers. A statistical thermodynamic model has been developed to elucidate these interactions. Aβ was simulated using fully-atomistic replica exchange molecular dynamics. We use an ensemble of 5×10^5 configurations taken from these simulations as input for a self-consistent field theory (SCFT) that explicitly accounts for the size, shape and charge distribution of the amino acids comprising Aβ as well as all molecular species present in solution. The solution of the model equations provides a prediction of the probabilities of the configurations of the interacting Aβ monomers and the potential of mean force between two monomers during the dimerization process. This model constitutes a powerful methodology to elucidate the underlying physics of the Aβ dimerization process as a function of pH, temperature and salt concentration.

Gold nanoparticles (NPs) are a promising class of materials for medical applications due to the unique properties that particles in this size range have on biological systems. Moreover, these NPs can be functionalized with ligands to effect a veritable cornucopia of biological responses. We have performed a central composite design of experiment to determine the effects of NP size and the length of end-grafted polyacrylic acid (PAA) molecules on the aggregation of Aβ. We find that a complex interplay exists between these two physical properties with respect to Aβ interactions

that is dependent on the bulk ion concentration. In particular, a regression analysis of the measured data indicates that NP diameter is negatively correlated with Aβ aggregation lag time and that an optimum length of PAA exists at low ion concentrations with respect to this response. We develop another SCFT to model the behavior of the PAA on the NPs' surface. We present this theory with two distinct formulations each employing a different polymer model and discuss the implications and practicality of their respective use. These theories allow us to make predictions regarding the effects that the polymers have on local solution conditions as a function of the same bulk solution conditions that modulate Aβ aggregation and to put our experimental observations in a more general theoretical context. The capacity to synthesize, characterize and test the efficacy of PAA-functionalized NPs as Aβ aggregation inhibitors coupled with accurate theoretical modeling of the thermodynamics and molecular organization of the system at the nanoscale constitutes a robust platform with which to design AD therapeutics.

Table of Contents

List of Tables

List of Figures

List of Symbols

a	Statistical Segment Length of Chain
e	Elementary Charge
D	Diameter of Nanoparticle
$E[\boldsymbol{r}_j]$	Internal Energy of Chain Molecule j with Space Curve $\boldsymbol{r}_j$
F	Generalized Free Energy Functional
f_i	Fraction of Charge for Chemical Equilibrium Site i
$f_{H^+,i}$	Fraction of Protonation for Chemical Equilibrium Site i
$f_{i,pH\,7}$	Fraction of Charge for Isolated Chemical Equilibrium Site i at pH 7
$K^o_{a,i}$	Acid Dissociation Constant for Chemical Equilibrium Site i
k_B	Boltzmann Constant
N	Degree of Polymerization
$P_j(\alpha)$	Probability of Chain Molecule j in Configuration α
$P[\boldsymbol{r}_j]$	Probability of Chain Molecule j with Space Curve $\boldsymbol{r}_j$
Q	Full Single Chain Partition Function
Q_j	Full Single Chain Partition Function of Molecule j

q	Partial Partition Function
$q^{\dagger}$	Complementary Partial Partition Function
q_i	Spectral Coefficients for Partial Partition Function
$q_i^{\dagger}$	Spectral Coefficients for Complementary Partial Partition Function
v_i	Volume of Molecular Species i
w	External Field
w_k	Spectral Coefficients of External Field
z_i	Valence of Molecular Species i
β	Reciprocal of the Thermodynamic Temperature $1/k_BT$
γ	Surface Tension
ϵ_o	Permittivity of Free Space
ϵ	Relative Dielectric Constant
ϵ_g	Average of Distribution of Polymer Tethering Distance from Surface
ϵ_i	Bulk Relative Dielectric Constant of Molecular Species i
ζ	Polymer Surface Depletion Parameter
κ	Non-Dimensionalized Radius of Nanoparticle Core
λ_i	Eigenvalues
μ_i	Exchange Chemical Potential of Molecular Species i

μ_i^o	Standard State Chemical Potential of Molecular Species i
$\mu_{i,c}^o$	Standard State Chemical Potential of Charged Chemical Equilibrium Site i
$\mu_{i,o}^o$	Standard State Chemical Potential of Neutral Chemical Equilibrium Site i
π	Lagrange Multipliers
ρ_i	Density of Molecular Species i
$\rho_{i,j}$	Density of Chemical Equilibrium Site i of Chain Molecule j
$\rho_{A\beta\,\delta,j}$	Density of Partial Atomic Charges on Aβ Molecule j at pH 7
σ	Grafting Density of Polyacrylic Acid on Gold Nanoparticle Surface
σ_g	Standard Deviation of Distribution of Polymer Tethering Distance from Surface
Φ_i	Basis Functions for Fourier Series Expansion
ϕ_i	Volume Fraction of Molecular Species i
$\phi_{A\beta,j}(\alpha)$	Volume Fraction of Aβ for Chain j in Configuration α
ψ	Electrostatic Potential

List of Abbreviations

Aβ	Amyloid-β
$A\beta_{1-42}$	Amyloid-β 1-42 Isoform
AD	Alzheimer's Disease
AIBN	Azobisisobutyronitrile
ATRP	Atom Transfer Radical Polymerization
AuNP	Gold Nanoparticle
CCD	Central Composite Design
CTA	Chain Transfer Agent
DCLM	Double-Cubic Lattic Method
DIW	De-Ionized Water
DLS	Dynamic Light Scattering
DOE	Design of Experiment
GPC	Gel Permeation Chromatography
LEF	Lag Extension Factor
MC	Monte Carlo
MD	Molecular Dynamics
MEHQ	4-Methoxyphenol

MF . . . . . Mean Force

MM-PBSA . . . . . Molecular Mechanics-Poisson Boltzmann Surface Area

MPI . . . . . Message Passing Interface

NP . . . . . Nanoparticle

PAA . . . . . Polyacrylic Acid

PDI . . . . . Polydispersity Index

PMF . . . . . Potential of Mean Force

ptBA . . . . . Poly tert-Butyl Acrylate

RAFT . . . . . Reversible Addition-Fragmentation Chain-Transfer

REMD . . . . . Replica-Exchange Molecular Dynamics

RIS . . . . . Rotational Isomeric States

SASA . . . . . Solvent-Accessible Surface Area

SCFT . . . . . Self-Consistent Field Theory

tBA . . . . . tert-Butyl Acrylate

TEM . . . . . Transmission Electron Microscopy

TGA . . . . . Thermogravimetric Analysis

THF . . . . . Tetrahydrofuran

TOAB . . . . . Tetraoctylammonium Bromide

Chapter 1

Introduction

1.1 The Specter of Alzheimer's Disease

Alzheimer's disease (AD) is the most common neurodegenerative disease in the world. It is the sixth leading cause of death in the United States. Notably, AD is the only disease of the top ten most lethal diseases with no known prevention or cure. While the incidence of heart disease, stroke, HIV and numerous types of cancers has gone down between 2000 and 2014, that of AD increased by 89%.[1, 2] Additionally, the number of people with AD in the United States is projected to more than double in the next three decades.[3] This prediction is attributed primarily to the aging of the so called Baby Boom generation and an increase in life expectancy. Age is the greatest risk factor in the development of the disease.

AD is characterized by neurological changes taking place in the brain and the onset of dementia. Alzheimer's dementia features a decline of several cognitive faculties including problem solving, memory and language. These faculties continue to worsen until the individual requires constant care to perform all activities. Ultimately, AD results in death.

AD is a tremendous and tremendously terrible phenomenon plaguing mankind. It is a deterioration of the mind and consciousness to the extent that a person knows not where they are, where they've been or anyone that they've ever loved. Compounding the insidious properties of this disease, those afflicted are often aware of their mind slipping away. They are audience to the slow and steady loss of everything that made

them who they are; acting as horrified and helpless onlookers of their own irreversible depersonalization. Humans who have lived for decades with otherwise indomitable spirits find themselves victims of a most sinister rotting of the mental faculties that most of us take for granted. Ultimately, AD results in the death of the individual, but in truth, the person is already dead. It is by this problem that we frame our efforts: to preserve the consciousness and dignity of those we have known and loved.

Efforts to tackle the monster that is AD have been ongoing for nearly a century, spearheaded largely by medical science and increasingly through assorted engineering disciplines.[4, 5] The fact that the pathology of AD remains unclear in spite of billions of dollars and millions of man hours of research serves as a testament to the complexity of the biochemical problem that AD poses as well as the ostensible obscurity of any solution relative to our present tools. One of the characteristic molecular processes of AD that has received abundant interest is the aggregation of amyloid-β (Aβ). Aβ is a small polypeptide fragment, ranging from 37 to 43 amino acids in length. It is cleaved from the Amyloid Precursor Protein through a series of secretases and released into the extracellular space (cerebrospinal fluid). It should be noted that Aβ is present in the brains of all humans; however, in those with AD, conditions and concentrations of Aβ are such that these small polypeptide fragments begin to aggregate. A single Aβ molecule is often referred to as a monomer due to its function as the single unit in larger aggregate structures. This gives rise to an interesting hierarchical structure present in the language describing amyloid processes in which the fundamental unit (or monomer from the perspective of polymer physics) of an amyloid molecule is an amino acid while the same notion for an amyloid aggregate is the amyloid molecule itself.

In the common parlance used to describe the Aβ aggregation process, monomers first combine to form dimers, trimers, etc. All aggregate structures comprised of less than 20 monomeric units are referred to as oligomers. However, the selection of 20 is

somewhat arbitrary and some researchers may refer to larger aggregates as oligomers. Under certain conditions, oligomers will continue to grow either via combination or monomer addition into soluble fibrils. These fibrils bear the characteristic cross β-sheet secondary structure perpendicular to the fibril axis that is characteristic of amyloid proteins in general. However, Aβ fibrils may contain either two or three strands of these aggregates associated laterally. This is an area in which the field has not unanimously converged on which structure is correct and it is the opinion of this researcher that different structures can form and stabilize under different conditions. These soluble aggregates can elongate and associate to form insoluble fibrils. These insoluble fibrils can deposit in the brain, constituting the amyloid plaques commonly associated with AD.

The presence of Aβ aggregates in the brains of those afflicted with AD led researchers to posit what is referred to as the Amyloid Cascade Hypothesis. This hypothesis proposes that Aβ aggregates are an etiological factor in AD.[6] This hypothesis is currently over 25 years old and in that time has seen its share of both support and detractors of its legitimacy. However, in the time since the hypothesis' inception, most studies continue to support the veracity of the Amyloid Cascade Hypothesis.[7] Consequently, disrupting the aggregation process of Aβ has retained its status as a preeminent strategy in the pursuit of potential AD therapeutics. Though, as shall be discussed, the story has developed substantially since Hardy and Higgins first reported their seminal idea.

1.2 Amyloid-β Oligomers: The Elusive Culprit

More recent studies have shown that the extent of the disease and severity of symptoms are better correlated with the presence of Aβ oligomers than that of Aβ fibrils.[8] As such, research has largely shifted toward attempting to understand the formation and structures of oligomer species as well as understanding the transition that is

made from oligomers to fibril structures. Despite the lack of consensus on Aβ fibrils, these species appear to possess considerably more order than do their oligomeric counterparts and these more so than the intrinsically disordered Aβ monomer. It is the intrinsically disordered nature of the Aβ monomer and the related instability and multiplicity of the myriad oligomer structures that has resulted in their defiance to characterization. Nonetheless, some progress has been made in this endeavor. The transition from Aβ oligomer to fibril is a process that has received considerable interest. It has also been hypothesized that there are oligomers that are somewhat stable though do not ultimately develop into fibrils, deemed *off-pathway* oligomers.

Amyloid-β (Aβ) is a short polypeptide with isoforms ranging from 37 to 43 amino acid residues. When Aβ proteostasis becomes disrupted *in vivo*, its concentration can increase to promote aggregation.[9] This aggregation process is exceedingly complex and involves a dynamic equilibrium including myriad sizes and conformations of aggregated Aβ. Single Aβ monomers coalesce into small aggregates, commonly referred to as oligomers. The formation of these early oligomeric aggregates, some of which are nuclei, is the rate limiting step in the aggregation process. This limitation is evidenced by the presence of a lag during the aggregation process as well as the cessation of this lag upon the introduction of preformed seeding nuclei.[10] The overall aggregation process culminates in the formation of insoluble aggregates, or fibrils, that exist in dynamic equilibrium with monomeric protein and smaller aggregates. For several decades, a mounting body of research has implicated Aβ aggregates as an etiological factor in AD.[7] However, more recent studies suggest that the most pathogenic aggregate species are the oligomers.[11] Additionally, the nucleation-limited nature of the aggregation process indicates that the formation of a certain oligomer species may be the necessary event triggering exponential growth of aggregates. For these reasons, recent work toward developing AD therapeutics has focused on identifying molecules that can inhibit the formation of Aβ oligomers. This endeavor necessitates

an understanding of the atomic structure of oligomers as well as their formation both in general and in the presence of inhibitors.

Current understanding of early Aβ oligomers stems primarily from experimental techniques and molecular dynamics (MD) and Monte Carlo (MC) simulations.[12] These studies aim to clarify oligomer structures and kinetic pathways of oligomer formation. Collectively, these works report a multitude of prospective structural motifs for each mass of oligomer species and numerous potential kinetic schemes for oligomer formation.[13, 14] In spite of this increased interest in oligomers, the exact structures of these species have remained ambiguous.[8] Moreover, information regarding the relative propensity of various oligomer species to form and their importance in the aggregation process are also unclear.

In this work, the dimerization of two $A\beta_{1-42}$ monomers is considered. Of the many MD simulation studies focusing on intermolecular interactions of Aβ, only select examples use an explicit solvent model, are fully atomistic and treat the full length $A\beta_{1-42}$ molecule.[15, 16] We believe that all of these methodological properties are necessary in simulation studies to accurately capture the relevant configurations; however, even when combined with traditional post-processing tools, these techniques are insufficient to accurately capture the thermodynamics of intermolecular interactions. Furthermore, a recent study found that the choice of force-field used in simulation of the Aβ dimer can significantly impact the predicted equilibrium secondary structure.[17]

We have implemented a novel approach that combines Aβ conformations obtained from MD simulations with a statistical thermodynamic model to directly address the multiplicity of relevant structures during the aggregation process. Chong and Ham have similarly approached this issue, aiming to capture the thermodynamics of Aβ.[18] However, their methodology and assumptions vary drastically from our own. Using our approach, the potential of mean force (PMF) between two interacting

monomers is calculated for several bulk solution conditions, providing insight into the thermodynamics of this interaction. This analysis yields results for the dimer that are consistent with well-established experimental understanding of the influence of solution conditions on the total aggregation process while providing molecular-level detail that is experimentally inaccessible.

1.3 The Fashionable and Wrong Tool for the Job

Over the past few decades computational implementations of molecular dynamics simulations have been truly transformative across numerous scientific disciplines.[19, 20] From identifying viable drug candidates in pharmaceutical settings to chemical vapor deposition, a veritable galaxy of molecular systems have been studied using simulation techniques leading to novel discoveries and indisputably pushing fields to new frontiers.[21, 22] The increase in the capability and consequent applicability of MD simulations is inextricably tied to the increased economy and performance of computational resources.

As is appropriate in emerging technologies, many of those who have created software to facilitate MD simulations and calibrated force fields for given physical situations disseminate the tools that they've created.[23–26] This encourages peer review and a more generally communicative culture. However, a side effect of the emerging order in the field is that there is a growing divide between the tool makers and the tool users. Indeed, it is now possible for a layman to simulate molecular processes using available simulation packages with absolutely no understanding of chemistry or physics whatsoever. Such extreme circumstances are not common in the technical research community. Unfortunately however, the general paradigm of those using MD simulation techniques not fully appreciating nor expounding upon the theoretical limitations of the methodology is unacceptably pervasive and it is precisely this tool maker/user dichotomy that has exacerbated the problem.

It is worth quickly pointing out the distinction between the lack of appreciation for the limitations of simulation that exists in academic research and efforts that amount to outreach or recruiting. In this latter camp, exists programs such as Foldit, one of the very objectives of which is to expose the uninitiated to science in a productive way.[27, 28] Foldit is a puzzle game involving protein folding the results of which have actually led to scientific successes.[29] Provided that conclusions arising from these types of programs are sufficiently vetted, they serve a largely beneficial and arguably necessary role in the development of the scientific community.

Returning to the discussion of simulations conducted by the intelligentsia, the ever expanding frontier of what can presently be simulated due to newly available computational capabilities has created a sort of obsession in the field with running larger and grander simulations. There often exists a mentality that if one simply had incrementally more computational power, the fundamental physics might present itself and a sudden clarity would be achieved.

It is unfortunate that the described simulation vogue has been so prevalent in theoretical studies of Aβ interactions when in truth it is a quintessential physical system for which MD simulation is ineffective. The unsuitability of the class of techniques is evident from the incredibly common compromises and simplifications that are made in these studies. Aβ aggregation is extremely sensitive to substitution and truncation of the amino acid sequence of the involved monomers. This property has been definitively established experimentally; nonetheless, a large number of studies have made just these types of compromises under the guise of simplifying the problem in order to understand aspects of the larger aggregation processes. The extrapolation of these findings to the full Aβ interacting system is suspect in the extreme.

Additionally, all implementations of MD simulation of Aβ utilize some degree of coarse-graining. On the furthest end of this spectrum, entire amino acids have been treated as a single entity identified by one position in space. At the finest reso-

lution, every atom is treated uniquely within a force-field that has been tuned to reproduce protein behavior. Furthermore, some researchers choose to use explicit water models whereas others have employed implicit solvation techniques. Given the experimentally-determined sensitivity of Aβ to even slight amino acid substitutions and bulk solution conditions, it is inconceivable that accuracy is retained across the full spectrum of coarse-graining techniques that have been employed in the literature. However, it must be stressed that ultimately the accuracy of an MD simulation is irrelevant with respect to predicting the types of thermodynamic information necessary to cut the molecular Gordian knot that is Aβ oligomerization. Imagine that one could simulate Aβ interactions perfectly, which philosophically perhaps is not a simulation at all. The most accurate map of a continent is the continent itself and at that point, is it still a map? Even with such a realistic account of an Aβ interaction, what one would possess is simply one of millions, if not more, of the relevant trajectories through phase space. The phrase relevant trajectories is used in this context to indicate trajectories the probability of which is non-negligible to the extent that their exclusion would skew the thermodynamic character of the process. With this information alone, very little can be gleaned about the thermodynamics of this interaction. Accordingly, one would need all of the relevant trajectories in order to capture the music of this interaction. This is precisely the perspective in which we have framed our statistical thermodynamic model. Statistical thermodynamics is the most appropriate language in which to describe these types of stochastic processes.

The statistical thermodynamic model that we have developed is the conceptual manner in which to approach the Aβ aggregation problem. The diversity of the Aβ monomer's configuration space and related diversity of dimer interactions necessitates a more statistical perspective in an accurate physical treatment. While the structure of fibrils is comparatively more ordered than that of monomers and dimers, the most pathological oligomer species possess a multiplicity of structures. Further-

more, the efficient engineering of therapeutics requires more than understanding these structures and processes for a single set of bulk conditions but rather across a wide range of temperatures, pH, ionic concentrations and geometries. It is for these reasons that molecular dynamics simulations are simply the wrong tool for this application.

Chapter 2

Statistical Thermodynamics of Aβ Oligomer Interactions

2.1 Background

A self-consistent field theory (SCFT) was developed and implemented to model the relevant physics of Aβ both in isolation and in the process of oligomer formation. The theory consists of formulating the relevant thermodynamic potential for isolated Aβ molecules in terms of the energy and entropy within a bath of solvent and ionic species. Extremization of this potential yields expressions for all equilibrium properties. The model explicitly accounts for the size, shape and charge properties of all species present. The model was developed to treat the presence of sodium and chloride ions (subscripted Na^+ and Cl^-) as well as hydronium and hydroxide ions (H^+, OH^-) in aqueous solvent (w).

The conceptual framework of the model closely follows that developed by Szleifer and coworkers to treat weak polyelectrolytes end-tethered to surfaces.[30, 31] This theory has proven robust in its ability to match experimentally observable properties for a variety of physical situations while providing insight into molecular organization not accessible by experiment.[32, 33] However, in the realization of the general theory used in this study, the center of mass of all conformations of the ensemble, rather than the terminus of the chain molecule, is constrained to a point in space. Additionally, unlike a homopolyelectrolyte, Aβ possesses 16 unique units (amino acids) in a molecule bearing only 42 units in total. Some of these amino acids possess either

Residue #						5					10					15				
AA Code		D	A	E	F	R	H	D	S	G	Y	E	V	H	H	Q				
pKa	Acid	3.7		4.3				3.7			10.1	4.3								
	Base	9.6				12.5	6.0							6.0	6.0					

Residue #						20					25					30				
AA Code		K	L	V	F	F	A	E	D	V	G	S	N	K	G	A				
pKa	Acid							4.3	3.7											
	Base	10.5												10.5						

Residue #						35					40					
AA Code		I	I	G	L	M	V	G	G	V	V	I	A			
pKa	Acid											2.3				
	Base															

Figure 2.1: Amino acid sequence and pKa values for chemical equilibrium sites of $A\beta_{1-42}$. pKa's for acidic and basic sites are shown in red and blue, respectively.

acidic or basic chemical equilibrium sites with varying acid dissociation constants, as shown in Figure 2.1. This characteristic of Aβ invalidates many of the assumptions commonly made in polymer physics that rely on the homogeneity of the chain molecule.

Thus, the theoretical model has been developed to account for the relevant physical properties of Aβ: the volume filling capacity or shape of the molecule, the position and characteristics of the chemical equilibrium sites, the charge density and the differing hydrophobicity of the amino acids. All of these properties are accurately captured in this framework. The manner in which these properties are manifest in the theory is illustrated in Figure 2.2.

2.2 Theoretical Methodology

2.2.1 Molecular Dynamics Simulations

To generate a structural ensemble for monomeric $A\beta_{1-42}$, fully atomistic replica exchange molecular dynamics (REMD) simulations of $A\beta_{1-42}$ were performed using the Gromacs (version 4.6.5) software package.[26] $A\beta_{1-42}$, referred to henceforth as Aβ,

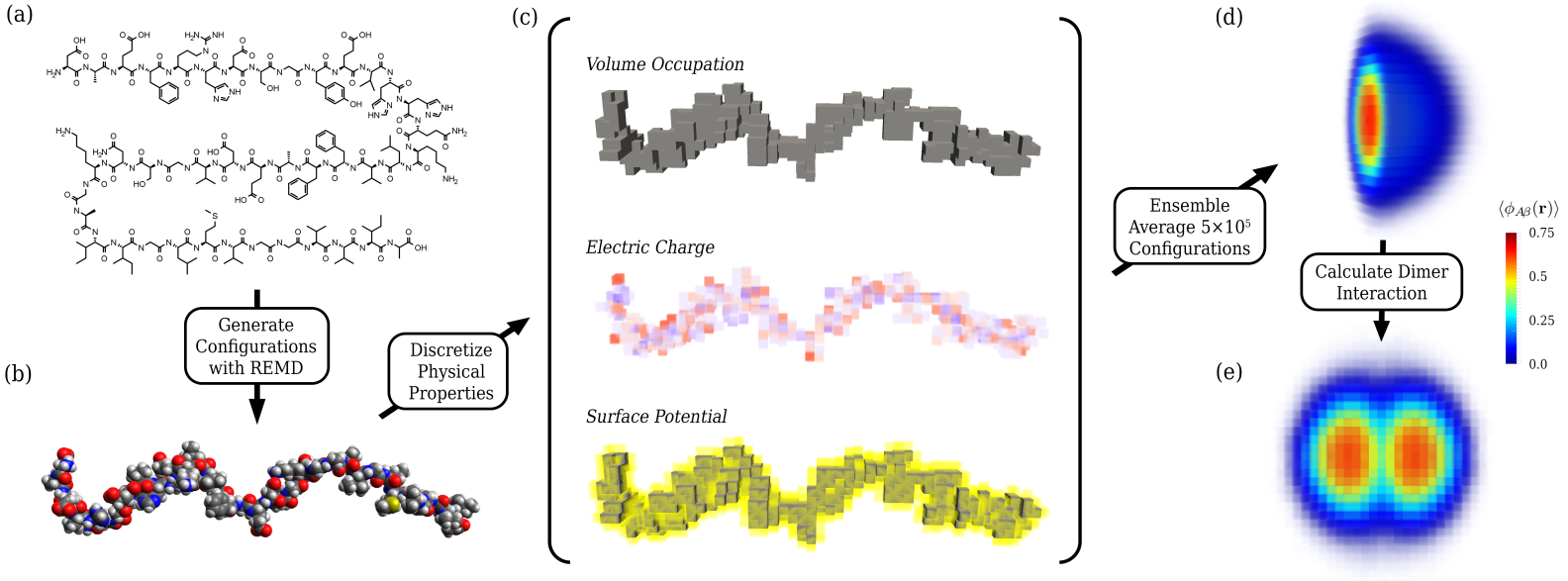

Figure 2.2: Schematic illustration of the calculation of thermodynamically equilibrated ensembles for $A\beta_{1-42}$. (a) Chemical structure of $A\beta_{1-42}$; hydrogens bound to nitrogens on the protein backbone have been omitted for illustrative purposes. (b) REMD simulations are performed using this chemical structure to generate 5×10^5 configurations. (c) For each configuration, physical properties (volume occupation, electric charge and surface potential) are discretely represented. These physical properties define a unique probability for each configuration in a given set of external conditions. (d) Said probabilities are used to calculate the ensemble average properties of an Aβ molecule. The local volume fraction of an Aβ ensemble is plotted according to the color scale on the right. (e) By constraining the centers of mass of two Aβ molecules to different relative separations, the potential of mean force (PMF) is determined.

was selected as the focus of this study due to its high propensity to form oligomers proposed to serve as the pathogenic species in AD.[34] The Charmm 36 force field parameters were used in all simulations.[25] The solvent was explicitly modeled using the TIP3P water model.[35] An Aβ monomer was simulated using REMD in a periodic cell at two different salt concentrations, 0 and 250 mM NaCl, and was assigned a net charge of $-3e$ at pH 7. A total of 53 replicas were simulated ranging in temperature from 270 to 601 K in a manner similar to the REMD study of the ensemble of Aβ monomer by Sgourakis et al.[36] In addition, two interacting Aβ monomers were simulated at 298 K and 150 mM NaCl. The interacting monomers simulation was initialized with the conformations of residues $1-16$ randomly generated and the conformations of residues $17-42$ matching those of two consecutive monomers in a fibril structure (pdb code: 2BEG).[37] This initialization point is consistent with two consecutive monomers excised from a typical Aβ fibril structure for which the first 16 residues are relatively unstructured while the remaining residues assume the cross β-sheet motif characteristic of amyloids. In one instance, residues $17-42$ were held fixed in space while residues $1-16$ were allowed to translate according to the force field. In a second instance, the entire protein was allowed to relax in space. It is very important to note that the fibril configuration is only used as an initial condition. The initial structure is almost immediately lost in the interacting monomer simulations due to the REMD.

For all simulations, conformations of Aβ were obtained by outputting the atomic coordinates of the protein at a frequency of 200 ps following equilibration of the system over 8 ns. To clarify, before using the isolated monomer and two interacting monomers in the REMD simulation we equilibrated both of them for 200 ns. Our simulations for the isolated monomer and interacting monomers included 627 atoms and 1254 atoms, respectively, which are surrounded by explicit water molecules and ions. There are around 30,000 water molecules for the both cases of isolated monomer

and interacting monomers REMD simulations. Ions are added according to the target concentration and the need to neutralize the system. These conformations were then subjected to rigid body rotations. In this way, a configurational ensemble of 5×10^5 configurations was constructed that contained relevant structures for the isolated monomer over a range of temperatures and at two ionic strengths as well as those for the interacting monomers simulations both during the process of binding and while bound.

2.2.2 Statistical Thermodynamic Model

The Helmholtz free energy is the thermodynamic potential minimized at equilibrium when the number of molecules, volume and temperature are held constant.[38] For this system, the free energy is expressed in the following generalized functional form:

$$
\begin{aligned}
\beta F = & \sum_j \sum_\alpha P_j(\alpha) \ln P_j(\alpha) \\
& + \sum_{i=\{H_2O, Na^+, Cl^-, H^+, OH^-\}} \int d\boldsymbol{r}\ \rho_i(\boldsymbol{r})(\ln \rho_i(\boldsymbol{r}) v_{H_2O} - 1 + \beta\mu_i^o) \\
& + \int d\boldsymbol{r}\ \beta\Big[\langle\rho_q(\boldsymbol{r})\rangle\psi(\boldsymbol{r}) - \frac{1}{2}\epsilon_o\epsilon(\boldsymbol{r})\big(\nabla\psi(\boldsymbol{r})\big)^2\Big] \\
& + \sum_j \sum_\alpha P_j(\alpha) \oint d\boldsymbol{S}_{j\alpha}\ \beta\gamma(1 - \langle\phi_{A\beta,\neq j}(\boldsymbol{S})\rangle) \\
& + \sum_{i=\{AA'\}} \int d\boldsymbol{r}\ \langle\rho_i(\boldsymbol{r})\rangle\Big[f_i(\boldsymbol{r})(\ln f_i(\boldsymbol{r}) + \beta\mu_{i,c}^o) \\
& \qquad + (1 - f_i(\boldsymbol{r}))(\ln(1 - f_i(\boldsymbol{r})) + \beta\mu_{i,o}^o)\Big] \\
& - \sum_{i=\{Na^+, Cl^-, OH^-\}} \int d\boldsymbol{r}\ \beta\mu_i\rho_i(\boldsymbol{r}) \\
& - \int d\boldsymbol{r}\ \beta\mu_{H^+}\Big(\rho_{H^+}(\boldsymbol{r}) + \sum_{i=\{AA'\}} f_{H^+,i}(\boldsymbol{r})\langle\rho_i(\boldsymbol{r})\rangle\Big) \\
& + \int d\boldsymbol{r}\ \beta\pi(\boldsymbol{r})\Big[\langle\phi^*_{A\beta}(\boldsymbol{r})\rangle + \sum_{i=\{H_2O, Na^+, Cl^-, H^+, OH^-\}} \phi_i(\boldsymbol{r}) - 1\Big]
\end{aligned}
\tag{2.1}
$$

The first term contributing to the free energy accounts for the configurational entropy associated with the Aβ molecules. $P_j(\alpha)$ denotes the probability of configuration α for Aβ monomer j, and the summations are performed over all monomers and all configurations. Consequently, the theory is generalized such that an arbitrary number of monomers can be modeled using the same framework. In the case of a single monomer, the ensemble of configurations is simply the conformations obtained from simulation translated such that they share a common center of mass. In contrast, when considering multiple interacting monomers, direction is no longer isotropic. In this work, the term conformation is used to define the relative positions of atoms in the protein, while configuration denotes both conformation and its spatial orientation. For multiple interacting monomers, an ensemble of configurations is generated by performing rigid body rotations on the conformations obtained from simulation. This same ensemble is used for all monomers in the system being modeled, meaning different monomers are distinguished from one another only by the location of their center of mass.

The second term in Equation 2.1 accounts for the translational or mixing entropy of the mobile species in solution. Here, $\rho_i(\boldsymbol{r})$ denotes the density of species i at position $\boldsymbol{r}$ and v_{H_2O} the volume of a solvent molecule.

The third term in Equation 2.1 accounts for free energy arising from electrostatic interactions. $\psi(\boldsymbol{r})$ is the electrostatic potential, ϵ_o is the permittivity of free space and $\epsilon(\boldsymbol{r})$ is the position dependent relative dielectric constant. The latter we define as a volume fraction weighted average of constant dielectrics for Aβ and the solvent: $\epsilon(\boldsymbol{r}) = \epsilon_{A\beta}\langle\phi_{A\beta}(\boldsymbol{r})\rangle + \epsilon_{H_2O}(1 - \langle\phi_{A\beta}(\boldsymbol{r})\rangle)$. The local ensemble average charge density, $\langle\rho_q(\boldsymbol{r})\rangle$, is given by the summation of the densities of all charged species:

$$\langle \rho_q(\boldsymbol{r}) \rangle = \sum_{i=\{Na^+,Cl^-,H^+,OH^-\}} \rho_i(\boldsymbol{r}) q_i + \sum_j \sum_\alpha P_j(\alpha) \Big[\sum_{i=\{AA'\}} \rho_{i,j}(\alpha;\boldsymbol{r})(f_i(\boldsymbol{r}) - f_{i,pH\,7}) q_i + \rho_{A\beta\,\delta,j}(\alpha;\boldsymbol{r}) \Big] \tag{2.2}$$

where the set AA' includes all amino acid residues in Aβ that are capable of bearing net charge, or more specifically the chemical equilibrium sites on those residues. This set includes those residues located at the N- or C- terminus and those residues containing an acidic or basic R-group. $f_i(\boldsymbol{r})$ represents the ensemble average fraction of charge of the chemical equilibrium site of amino acid i. q_i stands for the magnitude and sign of the charge of site or species i. $f_{i,pH\,7}$ represents the fraction of charge of equilibrium site i when the bulk pH is 7, and $\rho_{A\beta\,\delta,j}(\alpha;\boldsymbol{r})$ is the local density of partial atomic charges also at pH 7. These partial charges are the same as those used for the Charmm 36 force field. Using this method, the second term in Equation 2.2 ensures that the net charge for a given amino acid accurately reflects the local pH while preserving the variability of electron density in a manner consistent with our REMD simulations.

Treating the electrostatic energy through the Poisson equation, wherein the occupied volume of the protein and the solvent are defined by two distinct dielectric constants and the variation in charge density is treated by partial charges with delta functions located on the atomic centers, is equivalent to what is referred to as the polar component of solvation energy. The non-polar component of the free energy of solvation of the Aβ molecule is accounted for in the fourth term of the free energy functional presented in Equation 2.1, constituting an incorporation of hydrophobic interactions. This term involves a surface integral over the solvent accessible surface area (SASA) of configuration α multiplied by a surface tension, $\gamma = 5\ cal/mol \cdot \text{Å}^2$. This parameter is defined as the experimentally-fit free energy per SASA for small hydrocarbons in

an aqueous environment, which serve as the definition of a solvated non-polar surface.[39] In practice, we use an effective surface tension that adjusts for the disparity between the true SASA and the surface area of the configuration's discrete representation to calculate this term. Specifically, we calculate the SASA for each configuration using Gromacs, which utilizes the double cubic lattice method (DCLM), denoted $A_{DCLM}(\alpha)$.[40] We also calculate the discrete area of the surface, $A_{disc}(\alpha) = \oint \boldsymbol{S}_{j\alpha}$. We then define the effective surface tension as 5 $cal/mol \cdot \text{Å}^2(A_{DCLM}(\alpha)/A_{disc}(\alpha))$. In this way, the more accurate calculation of the SASA obtained using the DCLM is preserved even when using the discrete representation of the configuration's surface, which is necessary for computational tractability.

The non-polar free energy for configuration α, molecule j is $\oint d\boldsymbol{S}_{j\alpha}\ \beta\gamma$. This term, referred to in this work as the intramolecular solvation of a configuration, represents the non-polar intramolecular contribution to the free energy of solvation. This value is discounted by the amount of a configuration's surface that is concealed by the ensemble average presence of other Aβ molecules, $\neq j$. This modifying term is referred to herein as intermolecular solvation. Thus, the total non-polar free energy of solvation for configuration α, molecule j in its present local environment is given as $\oint d\boldsymbol{S}_{j\alpha}\ \beta\gamma(1 - \langle\phi_{A\beta,\neq j}(\boldsymbol{S})\rangle)$, the sum of intra and intermolecular solvation. Sitkoff, Sharp and Honig showed in the early 1990's that calculation of the solvation energy using an equivalent method can predict experimentally measured solvation energies.[39] This methodology has continued to develop and is now implemented in the simulation post-processing tool known as molecular mechanics Poisson Boltzmann Surface Area (MM-PBSA).[41]

The fifth term in the free energy expression accounts for the free energy arising from chemical equilibrium.[42] $\mu^o_{i,c}$ and $\mu^o_{i,o}$ represent the standard state chemical potential of the charged and neutral states of site i, respectively. The model has been developed such that the centers of mass and number of Aβ molecules are constrained

to fixed values for any given realization of thermodynamic equilibrium. However, rather than fixing the number of molecules of the mobile species in the system, as has been implicitly assumed thus far, we wish to fix the chemical potential of these species. This constraint results in a bath of these species in which the presence and properties of Aβ effect fluctuations in their total number in the system. Accordingly, the chemical potentials of the mobile species are subtracted from the original expression yielding a semi-grand potential:

In the previous expression, incompressibility has been enforced at all positions in space by the inclusion of a set of Lagrange multipliers $\pi(\boldsymbol{r})$, which, in this context, take on the physical interpretation of local osmotic pressure.[31, 43] Physically, this incompressibility constraint serves to include the steric repulsions of Aβ felt by the mobile species. From a practical standpoint, it serves to reduce the degrees of freedom of the system of equations such as to make its solution tractable. The ensemble average volume fraction, $\langle\phi_{A\beta}(\boldsymbol{r})\rangle$, is defined:

$$\langle\phi_{A\beta}(\boldsymbol{r})\rangle = \sum_j \sum_\alpha P_j(\alpha)\phi_{A\beta,j}(\alpha;\boldsymbol{r}) \tag{2.3}$$

where $\phi_{A\beta,j}(\alpha;\boldsymbol{r})$ is the volume fraction of Aβ for molecule j in configuration α at position r. This variable can take on values of either 0 or 1 indicating that the given molecule and configuration either does or does not occupy that position in space. $f_{H^+,i}(\boldsymbol{r})$ is the fraction of protonation of chemical equilibrium site i at position r. For basic equilibrium sites present on Aβ , $f_i = f_{H^+,i}$, while for acidic sites, $f_i = 1 - f_{H^+,i}$.

The thermodynamic potential represented in Equation 2.1 is that which is minimized at equilibrium for Aβ . Taking the functional derivative of this potential with respect to variables of interest and setting the resulting expression equal to zero yields the equilibrium expression for those variables.[44]

The equilibrium expressions for the densities of the mobile species are given by:

$$\begin{aligned}
\rho_{H_2O}(\boldsymbol{r})v_{H_2O} &= \exp[-\beta\pi(\boldsymbol{r})v_{H_2O}] \\
\rho_{H^+}(\boldsymbol{r})v_{H_2O} &= \exp[-\beta(\mu^o_{H^+} - \mu_{H^+} + \pi(\boldsymbol{r})v_{H^+} + \psi(\boldsymbol{r})q_{H^+})] \\
\rho_{OH^-}(\boldsymbol{r})v_{H_2O} &= \exp[-\beta(\mu^o_{OH^-} - \mu_{OH^-} + \pi(\boldsymbol{r})v_{OH^-} + \psi(\boldsymbol{r})q_{OH^-})] \\
\rho_{Na^+}(\boldsymbol{r})v_{H_2O} &= \exp[-\beta(\mu^o_{Na^+} - \mu_{Na^+} + \pi(\boldsymbol{r})v_{Na^+} + \psi(\boldsymbol{r})q_{Na^+})] \\
\rho_{Cl^-}(\boldsymbol{r})v_{H_2O} &= \exp[-\beta(\mu^o_{Cl^-} - \mu_{Cl^-} + \pi(\boldsymbol{r})v_{Cl^-} + \psi(\boldsymbol{r})q_{Cl^-})]
\end{aligned} \tag{2.4}$$

Minimization of Equation 2.1 with respect to the ensemble average fraction of protonation of chemical equilibrium site i yields the expression:

$$f_{H^+,i} = \frac{1}{1 + \frac{K^o_{a,i}\phi_{H_2O}(\boldsymbol{r})}{\phi_{H^+}(\boldsymbol{r})}} \tag{2.5}$$

However, as mentioned previously, there is a disparity in the relationship between fraction of protonation and fraction of charge for the acidic and basic sites. Additionally, the acid dissociation constant, $K^o_{a,i}$, is defined as $K^o_{a,i} = \exp[-\beta(\mu^o_{c,i}+\mu^o_{H^+}-\mu^o_{o,i})]$ for acidic sites and $K^o_{a,i} = \exp[-\beta(\mu^o_{o,i} + \mu^o_{H^+} - \mu^o_{c,i})]$ for basic sites.

Extremization of Equation 2.1 with respect to the electrostatic potential yields the Poisson equation:

$$\epsilon_o\nabla\Big(\epsilon(\boldsymbol{r})\nabla\psi(\boldsymbol{r})\Big) = -\langle\rho_q(\boldsymbol{r})\rangle \tag{2.6}$$

where boundary conditions have been imposed such that the electrostatic potential is defined as zero in bulk solution. This results in a familiar boundary value problem

in potential theory in which boundary values of the electrostatic potential are set and the task at hand is to determine the consequent rearrangement of matter within those boundaries.[45]

Extremization of the probability of Aβ configuration α for molecule j is performed with a caveat. Specifically, taking the derivative with respect to the probability of the starred term in Equation 2.1 yields the following term in the Boltzmann factor: $-\int d\boldsymbol{r}\ \beta\pi(\boldsymbol{r})\phi_{A\beta,j}(\alpha;\boldsymbol{r})$. The issue with this term is that the osmotic pressure is dependent on configurations of molecule j other than α. This cross-microstate influence is unphysical and, in the case of free isolated chain molecules treated within this framework, results in a disruption of well-established scaling behavior.[46] The details of solution that we have adopted to address this issue are outlined in the Supporting Information. In this manner, extremization of Equation 2.1 with respect to the probability is performed in such a way as to avoid unphysical interactions yielding:

$$
\begin{aligned}
P_j(\alpha) = \frac{1}{Q_j}\exp\Big[\int d\boldsymbol{r} \sum_{i=\{AA'\}} \rho_{i,j}(\alpha;\boldsymbol{r})\Big(\beta\psi(\boldsymbol{r})f_{i,pH\ 7}q_i - \ln(1-f_i(\boldsymbol{r}))\Big)\Big] \\
\times \exp\Big[\int d\boldsymbol{r}\ \frac{1}{2}\beta\epsilon_o\frac{\partial\epsilon(\boldsymbol{r})}{\partial P_j(\alpha)}\big(\nabla\psi(\boldsymbol{r})\big)^2 - \int d\boldsymbol{r}\ \beta\psi(\boldsymbol{r})\rho_{A\beta\,\delta,j}(\alpha;\boldsymbol{r})\Big] \\
\times \exp\Big[-\oint d\boldsymbol{S}_{j\alpha}\ \beta\gamma(1-\langle\phi_{A\beta,\neq j}(\boldsymbol{r})\rangle) + \sum_{k\neq j}\sum_{\sigma} P_k(\sigma)\oint d\boldsymbol{S}_{k\sigma}\ \beta\gamma\phi_{A\beta,j}(\alpha;\boldsymbol{r})\Big] \\
\times \exp\Big[\int d\boldsymbol{r}\ \phi_{A\beta,j}(\alpha;\boldsymbol{r})\Big(\frac{1}{v_s}\ln(1-\langle\phi_{A\beta,\neq j}(\boldsymbol{r})\rangle) - \beta\pi_{bulk}\Big)\Big] \\
\times \exp\Big[-\int d\boldsymbol{r}\ \langle\phi_{A\beta,\neq j}(\boldsymbol{r})\rangle\frac{1}{v_s}\frac{\phi_{A\beta,j}(\alpha;\boldsymbol{r})}{1-P_j(\alpha)\phi_{A\beta,j}(\alpha;\boldsymbol{r})}\Big]
\end{aligned}
\tag{2.7}
$$

Where we have introduced the single-chain partition functions Q_j in order to normalize the probability expressions. The equilibrium expressions for the probabilities of Aβ configurations constitutes the final set of equations necessary to calculate values for all physical variables.

2.2.3 Practical Solution of Equilibrium Equations

In order to solve for the variables present in Equations 2.3 through 2.7, these equations are converted from those which are continuous in space to their discretized counterparts. Space is discretized to a cubic lattice with spacing of 0.2 nm. As input, the atomic coordinates of Aβ obtained from simulation are used to define a discrete occupation matrix. A lattice site is defined as occupied by the protein molecule if said lattice site is located less than the van der Waals radius of a given atom from that atom's spatial coordinates, thus specifying the discrete representation of $\phi_{A\beta,j}(\alpha;\boldsymbol{r})$ in Equation 2.1.[47] Similarly, the partial charges are discretely represented via assignment on the positions of the lattice site nearest their respective atomic centers. The net charges of chemical equilibrium sites, specified by $f_i(\boldsymbol{r})$, are also assigned to the nearest lattice site. In continuous space, the surface integral in the last term of Equation 2.1 involves integration over the differential surface elements $d\boldsymbol{S}_{j\alpha}$. In discrete space, this surface integral amounts to a summation over surface sites adjacent to lattice site $\boldsymbol{S}_{j\alpha}$. The process of converting the raw atomic coordinates of a configuration into discrete representations of relevant properties that can be expressed in the theoretical model is illustrated in Figure 2.2.

The discrete versions of Equations 2.3 through 2.7 constitute a system of coupled non-linear equations. Using the discrete representation of the configurational ensemble, this system of equations was solved numerically using KINSOL.[48] All of the variables present in the theoretical model are quantifiable. The volume that was treated for all cases had dimensions of 18 by 18 by 30 nm with the vector of Aβ separation oriented along the center axis of the right rectangular prism's long dimension. This amounts to approximately 1.25×10^6 discrete volume elements for which the incompressibility constraint and Poisson equation are solved by modifying the independent variables of osmotic pressure and electrostatic potential. Furthermore, inspection of Equation 2.7 reveals that $P_j(\alpha)$ depends on the probabilities of

other configurations which cannot be known *a priori*. We therefore establish another set of equations for the probability expressions themselves in which the part of the expression containing other probabilities (the last two lines of Equation (2.7)) is treated as an independent variable. Given that we are treating approximately 5×10^5 configurations, this results in a system of about 3×10^6 coupled non-linear equations that must be solved simultaneously. This has been accomplished with a program written in the modern Fortran programming language using free format Fortran 90. The suite of programs and modules makes use of the Message Passing Interface (MPI) for parallelization. With the described parameterization and 12 doubly-hyperthreaded central processing units operating at 2.50 GHz (Intel Xeon E5-2640), the calculation of equilibrium properties at a single center of mass separation typically takes anywhere from one half to three quarters of an hour. At this rate, a PMF for interacting monomers under a given set of bulk conditions can be generated in about 18 hours.

It is possible to substitute all of the equilibrium expressions derived in the previous sections into the original generalized free energy functional (Equation 2.1). Doing so results in a substantial simplification of the expression yielding Equation 2.8.

$$\begin{aligned}\beta F =& \beta \sum_j \sum_\alpha P_j(\alpha) \oint d\boldsymbol{S}_{j\alpha}\ \gamma \langle \phi_{A\beta,\neq j}(\boldsymbol{S}) \rangle + \frac{1}{2}\beta\epsilon_o \frac{\partial \epsilon(\boldsymbol{r})}{\partial P_j(\alpha)} \int d\boldsymbol{r}\ \Big(\nabla\psi(\boldsymbol{r})\Big)^2 \\ &+ \sum_j \int d\boldsymbol{r}\ \frac{\langle \phi_{A\beta,j}(\boldsymbol{r}) \rangle}{v_s} \Big(\ln(1 - \langle \phi_{A\beta,\neq j}(\boldsymbol{r}) \rangle) - \beta\pi_{bulk} v_s - \frac{\langle \phi_{A\beta,\neq j}(\boldsymbol{r}) \rangle}{1 - P_j(\alpha)\phi_{A\beta,j}(\alpha;\boldsymbol{r})} \Big) \\ &- \int d\boldsymbol{r}\ \Big(\frac{1}{2}\beta \langle \rho_q(\boldsymbol{r}) \rangle \psi(\rho_q(\boldsymbol{r}) + \sum_{i=\{H_20, Na^+, Cl^-, H^+, OH^-\}} \rho_i(\boldsymbol{r}) \Big) \\ &- \int d\boldsymbol{r}\ \beta(1 - \langle \phi_{A\beta,j}(\boldsymbol{r}) \rangle)\pi(\boldsymbol{r}) - \sum_j \ln Q_j\end{aligned} \tag{2.8}$$

As a final check to validate the accuracy of the program, the total thermodynamic potential is calculated using Equation 2.1 and compared to its simplified counterpart Equation 2.8. This provides a powerful internal check for consistency, requiring that

variables have been accurately expressed in both their in their generalized classical density functional theory representation and in that of thermodynamic equilibrium. This check for veracity was instrumental while trouble shooting and developing the Fortran program. It should be noted that the numerical disparity between these two expressions is usually about two orders of magnitude greater than that defining the convergence criteria, the L2-norm error, for the system of equations, $O(10^{-4})$ versus $O(10^{-6})$. The source of this increased inequivalence has invariably stemmed from the electrostatics term and has been attributed to the difference in the manner in which the gradient operators are numerically approximated in their two formulations.

When one constrains the centers' of mass of two Aβ monomers within the treated volume, the thermodynamic potential βF represents the total intermolecular pair potential or PMF between the two proteins, illustrated in Figure 2.2. The mean force (MF) between the two molecules is simply the negative gradient of the PMF.[49] The PMF and the resulting MF between two Aβ monomers have been evaluated at different separations of the monomers' center of mass. The resulting function provides information pertinent to the relative dynamics, stability and structure of this protein interaction.[50]

2.3 Theoretical Results

2.3.1 Potential of Mean Force Calculation

To explore the physics of Aβ dimerization, the total thermodynamic potential given in Equation 2.1 was considered for two Aβ monomers whose centers of mass were constrained to a fixed separation. The system of equations was iteratively solved for separations ranging from 0 to 12 nm to obtain the PMF between the two Aβ monomers as a function of separation. This potential function was first calculated for a solution of pH 8.0, 150 mM NaCl and 25 °C, as shown in Figure 2.3a. This set of bulk solution conditions was selected for its common use in experimental studies to facilitate

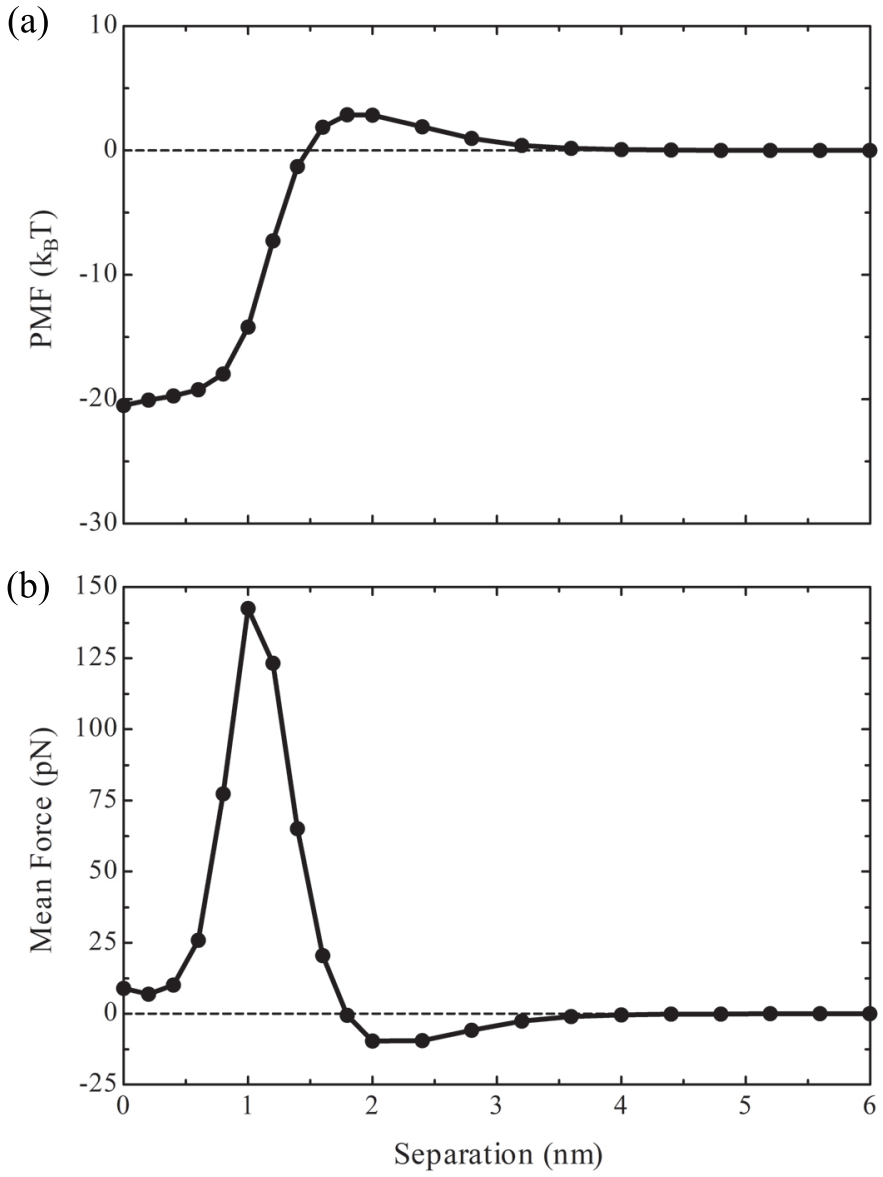

Figure 2.3: Potential of mean force (PMF) in k_BT (a) and mean force (MF) in pN (b) for two interacting $A\beta_{1-42}$ molecules calculated at pH 8, 150 mM NaCl and 25 °C, *Condition 1*. A potential or force of 0 has been defined as that which exists for two isolated $A\beta_{1-42}$ monomers.

comparison and is referred to in this work as *Condition 1*. In addition, the MF acting between two Aβ monomers, when the configurations of Aβ and positions of all mobile species are averaged in the relevant ensemble, was calculated from the PMF (Figure 2.3b).

Figure 2.3 indicates that the process of forming a dimer from two isolated monomers at *Condition 1* is kinetically limited but strongly favored thermodynamically. The PMF for this process exhibits a free energy barrier of 2.89 k_BT at a separation of 1.8 nm. A repulsive MF is present at separations greater than 1.8 nm and reaches its maximum magnitude of -9.66 pN at 2 nm. At separations less than 1.8 nm, a strong attractive MF pervades, which reaches its maximum of 142.5 pN at 1 nm separation. The PMF continues to decrease subtly from a separation of 0.6 nm to complete overlap of the monomers' center of mass, where the absolute minimum in the PMF is achieved at -20.05 k_BT. The deviation in this range is less than 1.5 k_BT.

The total potential function shown in Figure 2.3 is, at every separation, a sum of the individual free energy contributions corresponding to the terms in Equation 2.1 and the terms modifying this potential shown in Equation 2.1. Figure 2.4 shows these individual terms as functions of center of mass separation for *Condition 1*. It is important to note that the actual values of the free energy contributions are irrelevant to this analysis. However, the deviation of these terms from their value at large separations is indicative of how they either resist or benefit from localizing two Aβ molecules.

The free energy terms that deviate most from their bulk values at close separations are shown in Figure 2.4a. Of these terms, the translational entropy of the prevailing solvent species, water, constitutes the largest deviation. Interestingly, the translational entropy of water resists the dimerization process at large separations while favoring the process at closer separations, a behavior that mirrors that of the total PMF. The total ensemble average intra and intermolecular solvation energies are also significant contributors to the PMF. Intermolecular solvation favors the dimerization process. Conversely, intramolecular solvation constitutes a repulsive component of the PMF. The configurational entropy also contributes a repulsion to the PMF.

Free energy terms that contribute comparatively less to the PMF are shown in

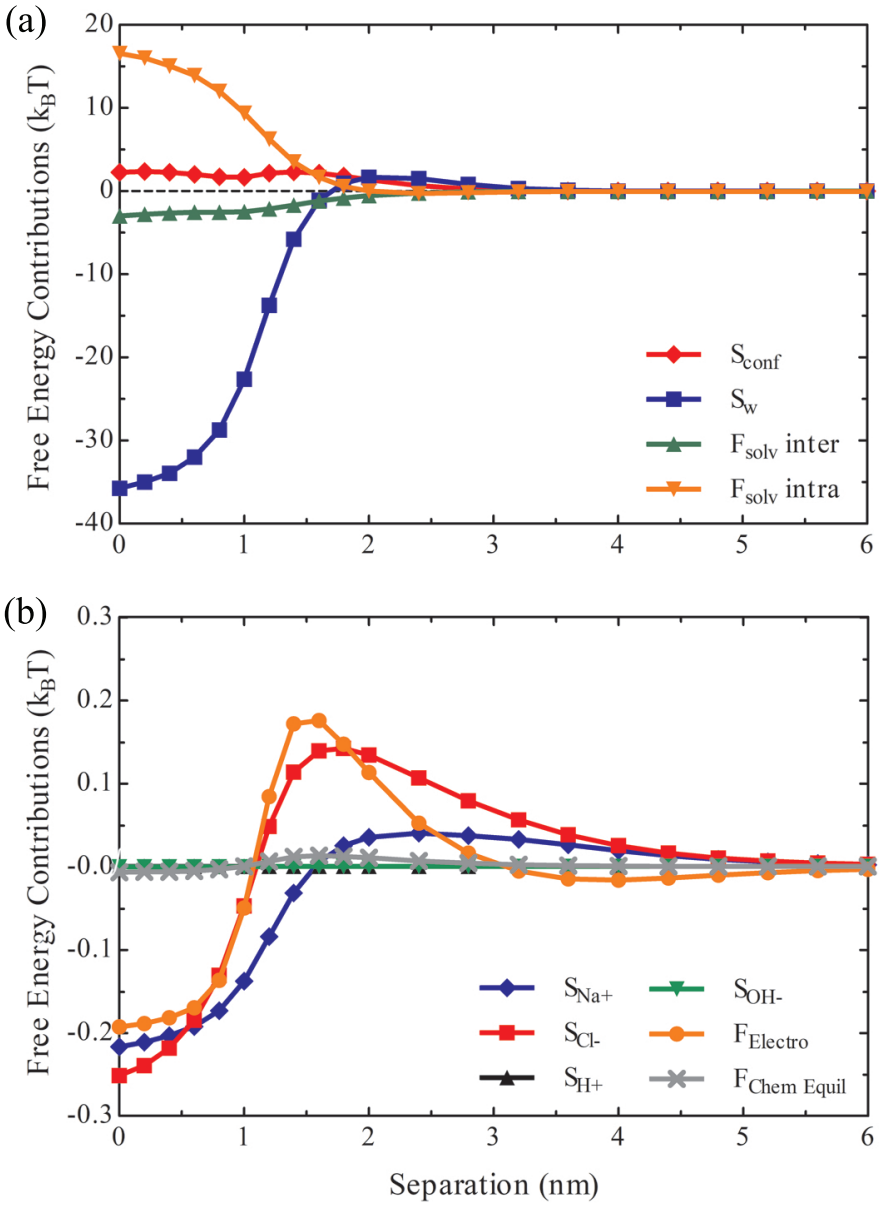

Figure 2.4: Individual free energy contributions to the PMF acting between two $A\beta_{1-42}$ molecules at pH 8, 150 mM NaCl and 25 °C, *Condition 1.* (a) Free energy terms with contributions to the PMF including the configurational entropy of the $A\beta_{1-42}$ molecules (red diamonds), the translational entropy of the water (blue squares), the intramolecular free energy of solvation (green up triangles) and the intermolecular free energy of solvation (orange down triangles). (b) Free energy terms with smaller contributions to the potential of mean force (MF), including the translational entropies of Na^+ (blue diamonds), Cl^- (red squares), H^+ (black up triangles) and OH^- (green down triangles) as well as the electrostatic free energy (orange circles) and the free energy of chemical equilibrium (gray times).

Table 2.1 Extrema of PMF and MF

Condition #		**1**	**2**	**3**	**4**
pH		8.0	8.0	8.0	***5.2***
Temp (°C)		25	25	***37***	25
[NaCl] (mM)		150	***25***	150	150
PMF (k_BT)	Min	-20.05	-20.42	-20.27	-21.29
	Max	2.89	3.21	2.91	2.78
MF (pN)	Min	-9.66	-9.74	-10.02	-10.20
	Max	142.53	139.59	145.66	157.29

Figure 2.4b. The translational entropies of the mobile ionic species largely parallel the qualitative trends the translational entropy of water, bearing a repulsive component at large separations and an attractive component at short separations. The same is true for the electrostatic free energy contribution. The chemical equilibrium free energy deviates comparatively little throughout the dimerization process.

2.3.2 Effect of Bulk Solution Conditions

To explore how the physics of Aβ dimerization is affected by conditions of the surrounding solution, PMF functions were also calculated for three separate bulk solution conditions that deviated in one parameter from *Condition 1*. One calculation was performed at a reduced ionic strength (25 mM NaCl, *Condition 2*), one at physiological temperature (37 °C, *Condition 3*) and one Aβ 's isoelectric point (pH 5.2, *Condition 4*). All unspecified bulk conditions for these calculations matched those of *Condition 1*. Both the PMF and MF plots for these calculations were qualitatively similar to that of the *Condition 1* calculation. However, these plots bear subtle but important quantitative differences in the magnitude of their extrema. These properties are summarized in Table 2.1. Collectively, this information demonstrates that bulk solution conditions are predicted to have a distinct effect on the thermodynamics of Aβ dimerization.

Relative to *Condition 1*, the reduced ionic strength of *Condition 2* results in a

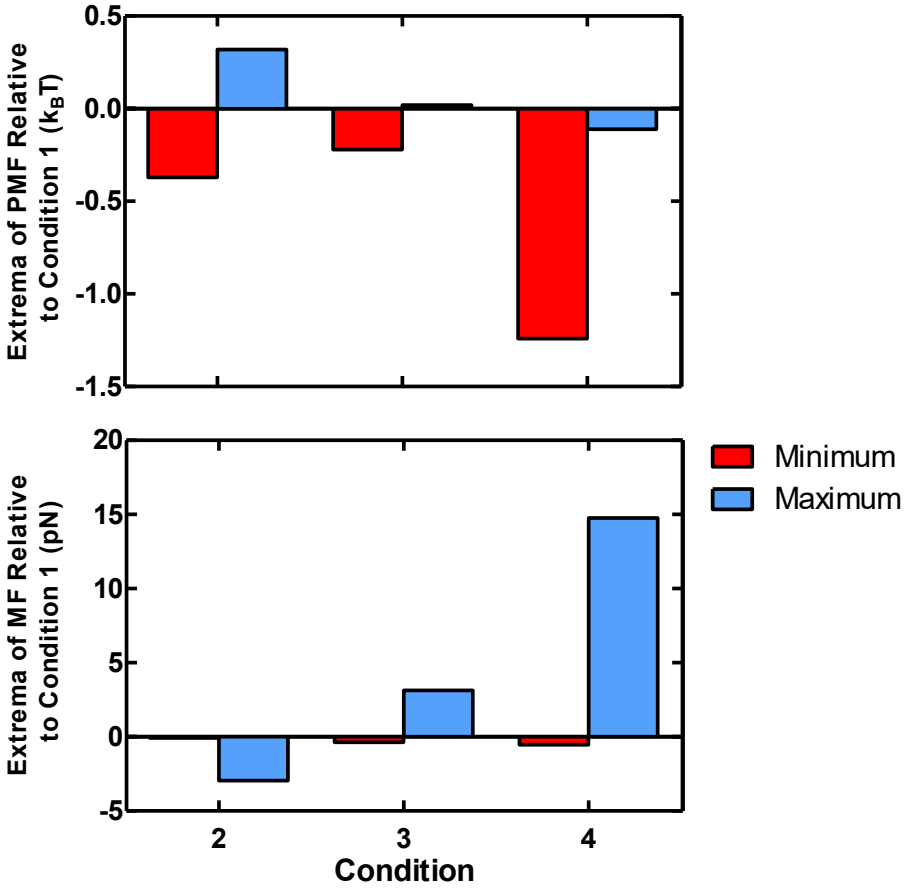

Figure 2.5: Deviations of extrema for PMF and MF from those calculated at pH 8, 150 mM NaCl and 25 °C, *Condition 1*.

greater free energy barrier by 0.32 k_BT, a deeper free energy well by 0.37 k_BT and negligible differences to the MF. This relative effect as well as those of *Conditions 3* and *4* are depicted in Figure 2.5. The elevated temperature of *Condition 3* made only minor differences to the PMF, increasing the free energy well by 0.22 k_BT. The PMF calculated at Aβ's isoelectric point, *Condition 4*, displayed a slightly reduced free energy barrier by 0.13 k_BT and a substantially deeper free energy well by 1.24 k_BT. Notably, the maximum MF for *Condition 4* was 14.76 pN greater than that calculated for *Condition 1*.

2.4 Discussion of Theoretical Predictions

2.4.1 Addressing Major Predictions

This study has developed and implemented a statistical thermodynamic model to analyze the binary interaction of two Aβ monomers. This theory takes as input a configurational ensemble obtained from REMD simulations and calculates the constrained equilibrium properties of all configurations that comprise this set. This approach has been expressly designed to account for the vast number of relevant structures of the oligomer formation process. The application of this theory to the Aβ dimerization process yields behavior that is both theoretically consistent and compatible with experimentally observed trends for the overall aggregation process.

All of the contributions to the total thermodynamic potential, shown in Equation 2.1, are highly coupled and in a delicate balance resulting in the overall minimization of this potential. If any one of these terms were removed, the others would display qualitatively different behavior. Furthermore, Figure 2.4 plots the difference between each of these terms and their values at a specified separation. In short, all of the terms and the physics that they represent are important in guiding the formation and structure of Aβ aggregates though not all of them deviate substantially in the dimerization process.

With this perspective in mind, Figure 2.4a clearly illustrates the components of the free energy that contribute most to the PMF as a function of center of mass separation: the translational entropy of water and the solvation energy. It is not surprising that these terms play such a large role in the interaction between two Aβ molecules. The behavior of the translational entropy of water, acting in a repulsive capacity at larger distances and an attractive capacity at shorter distances, is characteristic of chain molecules interacting through the excluded volume effects outlined herein. We observe for these binary interaction processes a spatial compaction of configurational

ensembles at intermediate distances and an expansion at closer distances. The expansion arises due to the strain on the configurational entropy to further compact, becoming untenable and taking on a more diffuse ensemble to avoid mutual overlap. This process is complicated when a potential is imposed on the molecule's surface. The hydrophobic character of this potential causes the ensemble to favor conformations that expose less of their surface to solvent. As a result, the negative contribution of the translational entropy of water is accompanied by a positive contribution from the intramolecular component of solvation. Configurations of one molecule are in a struggle between avoiding the presence of other molecules while minimizing solvent exposure. The intermolecular component of solvation always exhibits a negative contribution to the PMF because the ensembles can only increase their ability to mutually shield their surfaces from solvent when they are in close proximity to one another. A review of this term in Equation 2.1 confirms the negative-definite nature of this term in this context.

The configurational entropy is highly dependent on both the configurational ensemble provided as input and the physical situation in which the ensemble is allowed to equilibrate. For the ensemble and conditions presented here, the configurational entropy opposes the localization of two monomers, which indicates in a simplified sense that the probability distribution becomes less uniformly distributed as dimers are formed. An analysis of the sources of the relative probabilities of configurations reveals that those configurations obtained from simulations of interacting monomers become more probable as the molecules' centers of mass become closer. This point is elaborated upon in the Appendix.

The qualitative properties of the PMF functions generated for all conditions are consistent with experimental expectations. In general, a kinetically limited yet strongly thermodynamically stable picture of the Aβ dimer formation process is compatible with the current experimental state of knowledge. Crucially, there must exist

some amount of free energy barrier to the formation of a dimer in an accurate theoretical model of this process. At lower ionic strength conditions (25 mM NaCl), Aβ monomers persist for macroscopic time scales. The fact that we observe this energetic barrier in the predictions of our model is encouraging, as this behavior would simply not be possible without it.

To determine the effect of bulk solution conditions on binary interactions of Aβ, the model has been applied to the process at four distinct bulk conditions, listed in Table 2.1. Though this study focused solely on the binary interaction of Aβ monomers, the results obtained correlate with well-established experimental understanding of the overall Aβ aggregation process. The model predicts that dimer formation at lower ionic strength will be subject to an energetic barrier of approximately 0.37 k_BT greater than that which occurs at 150 mM NaCl. Experimentally, decreasing the ionic strength of an *in vitro* aggregation reaction correlates with a longer lag phase and slower aggregation, paralleling this greater energetic barrier.[51] From the theoretical results, it can be observed that fewer ions in *Condition 2* result in less screening of the perturbation to the electrostatic potential caused by the charges on Aβ.

The model also predicts that lowering the pH from 8.0 to 5.2 results in an increase in the stability of the dimer by 1.24 k_BT and an increase in the maximum attractive MF from 142.53 to 157.29 pN. This result correlates with experimental observations that Aβ aggregates most efficiently at its isoelectric point.[52] The model further indicates that the aggregates under these conditions are more stable. Finally, little difference exists between the PMF functions of *Condition 1* and that of the elevated temperature. Though the nucleation rate of Aβ aggregation is known to depend on temperature, we observed this bulk condition to have only a modest effect on the PMF of dimerization.[53]

2.4.2 Some Fine Details and Potential Misconceptions

At this point, some potential misconceptions pertinent to this theoretical model will be clarified. A prediction made by the model that may initially raise suspicion is the shear magnitude of the free energy change for the Aβ dimerization process. To put this prediction in context, it is worth describing the somewhat subtle implications of this free energy change through the lens of this statistical mechanical treatment. In order for this treatment to be accurate, one must assume that the time scales for equilibration of the mobile species are negligible relative to that of the proteins. This is a very reasonable assumption to make for the considered bulk conditions. In addition to the picture of two ensembles with constrained center's of mass being equilibrated at different distances, this PMF could also be thought of as the ensemble average of all of the trajectories of two interacting Aβ monomers. These are the types of trajectories that would be observed in simulation, some of which would feature more or less of a free energy disparity. Accordingly, the results of our calculation do not imply that one would never see dissociation of Aβ *dimers* in simulation nor that the probability of seeing dissociation thereof is non-zero but astronomically low. More accurately, it implies that the ensemble average of the trajectories that one might sample with simulation feature an overall drop in free energy of $20k_BT$. Such a large free energy well between two isolated Aβ monomers and an associated dimer does not directly imply that one would not observe monomers on macroscopic timescales in experiment.

Furthermore, this estimate of an approximately 20 k_BT free energy well is in fact comparatively small relative to other quoted values in the literature. Pouplana and Campanera simulated the 10-35 isoform of Aβ and used MM-GBSA to derive free energy values.[54] They quote a stability free energy for the dimer as -26.4 kcal/mol which at the simulation temperature of 298K is -48 k_BT. Chong and Ham used a *fluctuating thermodynamics* model to analyze the Aβ dimerization process.[18] Though

they do not quote an exact free energy disparity between isolated and associated dimers, one can see from Figure 4 in their work that the energy scales of this process are on the order of 100 k_BT. In principle, several assumptions and methodological decisions made in these studies are suspect, hence our desire to develop a more rigorous model. However, these results are mentioned to illustrate the point that all efforts of which we are aware to elucidate the free energy change of this process through a thermodynamic analysis have yielded large free energy values and in fact, our estimate is on the lower end of this spectrum.

Finally, since the SCFT outputs the changing probabilities of each Aβ configuration as the centers' of mass of the Aβ monomers are brought into close proximity, it is possible to map this onto a distribution of dimer structures. That is, one could quantify the ensemble average presence of the secondary structures frequently of interest in protein interaction studies (i.e. β-sheet, α-helix content). However, such an analysis would not influence the thermodynamic conclusions gleaned. A quantification of the relative ensemble average content of protein secondary structure could constitute a point of validation by experiment; though this connection would likely be most powerful if the methodology were extended to larger oligomer structures. However, this methodology is not actually capable of quantifying the probability of a dimer configuration. Rather, it quantifies the probability of a monomer configuration interacting with the ensemble average of another monomer. This is an important and subtle distinction that should be appreciated and understood as a word of caution should one aim to interpret the ensemble average secondary structure content predicted by this model for any structures larger than a single monomer. We have now arrived at what might be the most clear point of departure made by our methodology from that of the current state of the field: our methodology forgoes the accurate elucidation of oligomer secondary structure resolution in order to make accessible the thermodynamics of oligomer formation and ensemble average geometry as a function

of physiologically relevant bulk solution conditions.

2.5 Reflections on the Methodology and Future Directions

This statistical thermodynamic model has been applied to binary interactions of Aβ monomers for several relevant conditions, identifying key free energy contributions and yielding results that align qualitatively with Aβ aggregation. However, it should be emphasized that this model can be used to efficiently treat an arbitrary number of Aβ molecules interacting in bulk conditions that are completely tunable. The treatment of mobile species as field variables rather than particles allows one to precisely specify and capture the effects of bulk conditions much more easily than is possible in atomistic MD simulation.

This theory is capable of quantifying thermodynamic parameters of Aβ interactions that cannot be measured experimentally. Moreover, these thermodynamic relationships provide a rich description of the molecular organization and physics that guide these interactions. Though this study treated only the binary interactions of monomers, the results that are predicted correlate with expectations based on well-established experimental behavior.

Further work will extend this model to the treatment of the interactions of larger aggregate species in order to elucidate structural properties of these larger oligomers and characterize the thermodynamic pathways of their formation. Preliminary efforts to apply the model to higher order Aβ interactions have been met with two distinct obstacles both of which are ostensibly surmountable.

First, there is the possibility for the equation solver, which amounts to a specific implementation of KINSOL in this study, to transiently predict ensemble average Aβ volume fractions in excess of 1. This can cause an issue with the switching of the interpretation of the excluded volume interaction energy density $E_j(\boldsymbol{r})$ from that outlined in Equation 2.7 to the osmotic pressure $\pi(\boldsymbol{r})$. This is necessary to ensure

that incompressibility is not violated under any circumstance. The theoretical need for this special constraint is elaborated upon in the Appendix. In practice, this reinterpretation has proven difficult to implement algorithmically.

Secondly, we have shown first for the case of three interacting monomers and subsequently for the case of dimers that at least two solutions to the equilibrium equations exist for certain conditions. Preliminary attempts to apply the model to three interacting Aβ monomers were done in a linear arrangement. Two Aβ monomers were equilibrated and third's center of mass was then brought successively closer. At each point in this process, previous solutions to the equilibrium equations were used as an initial guess for the current calculation. It was found that depending on some subtle idiosyncrasies of this process, the third Aβ monomer's ensemble average volume fraction would either expand into a toroidal shape or into an even more expansive spherically symmetric object. The free energy of the torus was found to be higher than that of the sphere. Subsequently, it was found that through careful coaxing of the solver through the use of a succession of initial guesses it was possible to obtain multiple solutions for even dimeric interactions. In every case of multiple solutions being observed, the free energies of the solutions have deviated by more than one k_BT and that with the lowest free energy has been interpreted as physical.

A final note should be made on the sensitivity of the calculations to the input ensemble. It has been our intent to achieve two superficially paradoxical properties in the ensemble generated with REMD simulation. First, we desire that the ensemble contain those conformations that are relevant to the Aβ interaction. The motivation for this is clear: our statistical thermodynamic model is only able to determine the equilibrium probabilities of those conformations that it is provided as input. Secondly, we desire that the ensemble sample configuration space with equal *a priori* probability. Of course, neither of these properties are perfectly achievable in practice and in fact the latter ensemble property is gauranteed not to be perfectly achieved as long as a

constant force field is used. However, we believe that our use of REMD to avoid meta stable free energy wells and the selection of a series of bulk properties amounts to an excellent first approximation with respect to the achievement these two properties. In the future, a more thorough statistical analysis might be employed in an effort to quantify the discussed ensemble properties via methods similar to those used by Sgourakis et al.[36]

The unique flexibility of this theoretical framework to treat solution conditions and systems of arbitrary geometries renders this theory a promising tool in two important aspects. First, it could be used to further fundamental understanding of the Aβ oligomerization process and how this process depends on different factors. Secondly, this model could be used as an aggregation inhibitor design tool through the incorporation of inhibitor molecules into the framework.

Chapter 3

Nanoparticle Systems as an Alzheimer's Disease Therapeutic Platform

3.1 Background

In the last 50 years, research and understanding of nanoparticles (NPs) has grown immensely.[55] NPs are a promising prospect to biomedical engineers due to the unique effects that particles in this size range have on biological systems.

In the last few decades, NPs featuring a variety of material cores and surface functionalizations have been investigated for their effects on Aβ aggregation. Aβ is a small polypeptide fragment, ranging from 37 to 43 amino acids in length. It is present in the brains of all humans however, in certain cases, conditions and concentrations of Aβ are such that these small polypeptide fragments begin to aggregate. This biochemical process is characteristic of Alzheimer's disease (AD). Furthermore, the widely accepted Amyloid Cascade hypothesis posits that the presence of Aβ aggregates is an etiological factor for AD. Consequently, the identification and characterization of efficacy of agents capable of disrupting the Aβ aggregation process has emerged as a promising strategy in the search for a cure. In this regard, NPs have interestingly been shown to display either inhibition or promotion of the Aβ aggregation process depending on their physical properties. Significantly, those NPs that have displayed an effect on Aβ aggregation have done so at substoichiometric concentrations far below that of all other small molecule and peptide therapeutics that have been tested for this application. The remarkable potency of these agents is an extremely attrac-

tive characteristic as the ability to safely deliver therapeutic concentrations to the site of action is an absolute necessity for any successful therapeutic. Furthermore, the physical properties of NPs (size, shape and surface functionalization) are highly tunable, which could theoretically allow researchers to continuously adjust their effects on aggregation. However, the diversity both in physical properties and effects on Aβ aggregation that these NPs possess as well as the lack of clarity of the connection between these two observables necessitates a more fundamental understanding of the molecular mechanics at play.

For most of the studies reporting NPs that have an effect on Aβ aggregation, the authors' mechanistic hypothesis, if offered, involves some manner of physical contact between the protein and the NPs. A recent work published by our group studied the effects of spherical gold NPs (AuNPs) of different diameters (8, 18 and 40 nm) and surface functionalizations (successively electrostatically associated citrate, cetylammonium bromide, polyacrylic acid (PAA) and polyallylamine hydrochloride) on Aβ aggregation.[56] This study found that AuNP size and functionalization had significant and distinct effects on Aβ aggregation. In particular, when incubated in a solution 40 mM tris-HCl, PAA-functionalized AuNPs at substoichiometric ratios of 1:2,000,000 promoted Aβ aggregation in the presence of 150 mM NaCl while abrogating aggregation in the absence of this salt. At this ratio, the available surface area on the NPs is orders of magnitude smaller than what would be necessary to bind an appreciable quantity of the Aβ in solution. The sensitivity of these NPs' effects on solution conditions as well as their potency supports our mechanistic hypothesis: **these NPs modulate local solvent conditions, disrupting the configurations of Aβ such that the formation of stable nuclei occurs at an altered rate in a manner dependent on bulk solution conditions.**

The present study aims to further elucidate the connection between the physical properties of PAA-functionalized gold nanoparticles, referred to henceforth simply as

NPs, and their effect on the aggregation of Aβ.

A SCFT is then derived and discussed employing two different polymer chain models that can be used to make predictions of the local solvent conditions proximal to the NPs at thermodynamic equilibrium.

3.2 Experimental Methods

3.2.1 Motivating Factors for Experimental Design

We have synthesized spherical gold cores of various diameters (D), functionalized them with PAA of different degrees of polymerization (N) via end-grafting and tested the resulting NPs for their effects on Aβ aggregation. Preliminary studies conducted by our research group identified an interesting location of design space that ostensibly featured curvature with respect to the stated design parameters' effect on the response of Aβ aggregation. Following these studies, NP configurations were engineered in an attempt to achieve a central composite design (CCD) of experiment to further probe this part of design space.

Initially, several other orthogal dimensions of the NPs' physical properties configuration space were considered. These properties included NP morphology, polydispersity of NP morphology, polydispersity of size, polydispersity of the degree of polymerization of PAA, as well as PAA grafting density and the polydispersity thereof. Our preliminary work synthesizing and characterizing NPs bore evidence to the fact that we could reliably synthesize spherical NPs of high monodispersity as well as PAA with a satisfactorily low polydispersity index. During this period it was decided to assume that the grafting density of PAA was constant across the design space. This is perhaps one of the more tenuous assumptions made in this study. While this approximation is a justifiable assumption to make across this design space, it is certainly not rigorously accurate. However, the investment of time and capital required to make this measurement with the available facilities for every sample proved

prohibitive. This is disregarding the fact that if we did acknowledge deviations in grafting density and found that they were non-negligible, we would not be able to perform an experimental design capable of elucidating mechanistic information on Aβ modulation effects without making an effort to control this new parameter. Doing so is possible and essentially amounts to blocking sites for the gold-thiol bonds to form however, this would greatly increase the complexity of synthesizing an already complicated collection of experimental materials. For these reasons, PAA grafting density was measured for a representative sample and assumed to be common for all others.

Preliminary studies evidenced to the fact that NP concentration was an experimental condition that had an effect on Aβ aggregation. However, within the range that was tested in these studies, the effect on aggregation did not change in character though in some cases it was amplified. That is, those NP samples that inhibited aggregation tended to do so across the tested concentration did so in a proportionally dose-dependent manner. Consequently, it was decided to select a single concentration for the CCD, 1 nM NPs.

Following our previous study, the incumbent gold was selected as the material of construction for these particles for several reasons. Critically, there exists a range of gold NP sizes and surface functionalizations that have been shown to be non-toxic.[57] Gold yields the most stable metallic NPs.[58] Its facile synthesis makes achieving high monodispersity for a range of sizes and a variety of shapes relatively reliable. The surface of gold NPs can be functionalized with many different classes of molecules with a range of binding strengths.[59] Due to the inherent difficulty in characterizing the molecular architecture of chain molecules electrostatically-associated to a surface, we have opted to use a different method of binding PAA to the surface. In particular, we are using bidentate thiol bonds to end-graft PAA to the NPs' surface. This method of functionalizing the NPs' surface also possesses the desirable property that

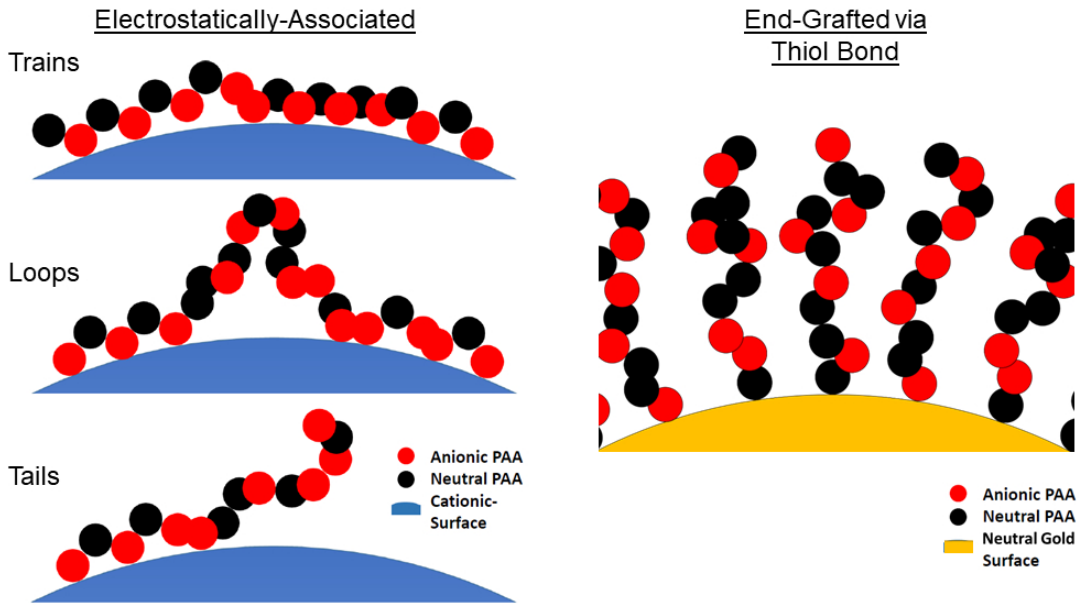

Figure 3.1: Illustration of disparate molecule architectures for electrostatically-associated polyacid layers vs. end-grafted binding motifs.

it is more uniform and stable in a wider range of bulk solution conditions than the electrostatically-associated layering. An illustration of the two discussed binding regimes is shown below in Figure 3.1.

As is depicted in Figure 3.1, there will exist populations of different molecular architectures in electrostatically-associated layers: loops, trains and tails. Furthermore, the distribution of polymer conformations among these different classifications is highly sensitive to pH and ion concentration.[60, 61] While in certain situations this type of molecular rearrangement may be desirable, it is simply too unpredictable to be used to elucidate the types of mechanistic solution effects that must be understood to engineer this potential AD therapeutic system. With this perspective, thiol mediated end-grafted PAA not only bears more attractive physical properties but is also considerably simpler to model theoretically.

3.2.2 Gold Nanosphere Synthesis

Gold nanoparticles have been heavily studied in colloidal science due to their excellent stability and utility in many applications.[62, 63] Synthesis methods are well established and applications range from those in catalytic science to biotechnology.[64–67] Early and impactful developments in gold nanoparticle synthesis were made by Turkevich and Frens followed by Brust.[68–70]

In the 1950s Turkevich published a method which could be used to synthesize monodisperse AuNPs with core diameters of 10-20 nm by reducing hot chloroauric acid with sodium citrate in water.[68] This method is very effective at the prescribed conditions due to the ability of sodium citrate to act both as a reducing agent and a capping agent. Frens later elaborated on this work by establishing a method of size control based on manipulating the ratio of sodium citrate to choloroauric acid used in the synthesis.[69]

Brust and Schriffin also pioneered a method in the 1990's which was integral in shaping modern gold colloidal synthesis. Their method addressed certain limitations of the Turkevich/Frens methodology such as accessing smaller particle sizes and stabilizing the AuNPs in an organic medium.[70] Brust and Schiffrin utilized tetraoctylammonium bromide (TOAB), a quaternary ammonium compound which can both cap the AuNPs and act as a phase transfer agent, together with a sodium borohydride reducing agent and the organic solvent toluene. This methodology allowed Brust and Schiffrin to carry out the reduction at room temperature due to the higher reducing power of sodium borohyride relative to citrate. Furthermore, their method is amenable to the use of alkanethiol protecting agents which provide excellent long term stability in solution.

The simple ingenuity of the Turkevich/Frens methodology, to use sodium citrate as both a protective and reducing agent, also presents its primary limiting factor. The low reduction potential of sodium citrate limits the minimum sizes which are

accessible via the methodology while the maximum sizes are limited due to the risk of destabilizing the gold colloid if the citrate concentration is reduced to a level too low to afford adequate protection. This has been the subject of many more recent studies regarding AuNP colloidal synthesis. Several promising strategies have been reported which lead to the synthesis of monodisperse NPs over a wide range of core diameters.[71–75].

An interesting example was reported by Sivaraman who found that simply reversing the order of reactant addition typically used in the Turkevich/Frens method (adding chloroauric acid to hot citrate) led to the formation of AuNP colloids with <10 nm average diameter and excellent monodispersity.[74] This is accomplished by simultaneously making the environment more favorable for nucleation and more effective for stabilization. This effect is hypothesized to be a result of the solution pH where maintaining a low pH initially is favorable for nucleation and maintaining a neutral pH is initially favorable for stabilization.[74] Others have employed stronger reducing agents with sodium citrate including sodium borohydride and ascorbic acid thus developing seeding growth methodologies involving the use of intermediate AuNP sizes as nucleation seeds to produce larger, monodisperse colloidal solutions.[66, 76]

Thermal Citrate Method

In this work, a thermal citrate method useful for synthesizing AuNPs between 10 and 20 nm modified based on a modified version of what was reported by Liang and coworkers.[66] Their method involved heating an aqueous solution containing 0.001M $HAuCl_4$ to reflux at 100 °C, adding 5 mL of aqueous sodium citrate solution to the hot $HAuCl_4$ solution and allowing the combined solution to reflux for 15 minutes. In order to elicit further size control over the colloid various citrate/gold molar ratios were tested including 10, 7.5, 5, 2.5, and 1. TEM images of the AuNPs synthesized with the modified thermal citrate method are shown in Figure 3.2. The most striking

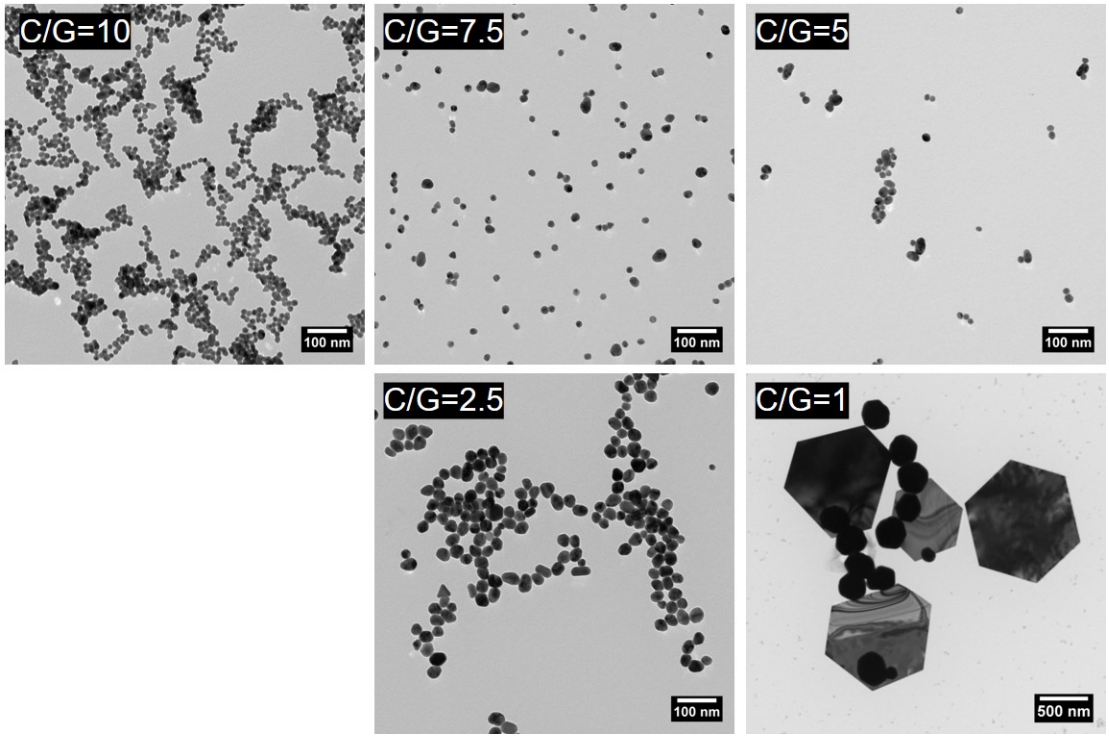

Figure 3.2: TEM micrographs showing size and morphology of AuNPs synthesized with thermal citrate methodology and varied C/G ratio. The author would like to acknowledge Kate Mingle for taking the TEM images.

effect of changing the citrate/gold molar artio is seen at a value of C/G=1 where the nucleation and growth kinetics have clearly changed leading to the formation of a polydisperse colloid containing two completely distinct morphologies including spheres and large faceted particles greater than 500 nm in size. At C/G ratios greater than 1, the effect of increasing the ratio led to the formation of smaller particles with average sizes between 14.5±1.9 nm and 31.1±5.7 nm. There was not a significant change in particle size upon increasing the C/G ratio from 5 to 7.5, although the colloid was slightly more monodisperse in the case of C/G=7.5. The particle size analysis for each C/G ratio is shown in Table 3.1, where sizes were calculated both manually and using the program CellProfiler.

Table 3.1 AuNPs for Thermal Citrate Method

C/G Ratio	Avg. Size (nm)	
	CellProfiler	Manual
10	14.5±1.9	14.2±1.75
7.5	17.3±1.4	17.4±1.52
5	18.1±2.7	18.4±3.28
2.5	31.1±5.7	31.2±4.44
1	*Did not analyze	

Reverse Citrate Method

Similar experiments were performed using a modified reverse citrate method. The methods used for these experiments were based on those reported by Liang and coworkers where the expectation was that equivalent C/G molar ratios should yield smaller AuNP colloids for the reverse citrate method rather than the standard thermal citrate method. As the name implies, the reverse citrate method involves heating aqueous solutions of sodium citrate solution to reflux at 100 °C and adding 5 mL of room temperature 0.001 M $HAuCl_4$ to the hot citrate solution and stirring for 15 minutes. The C/G ratios included 15, 10, 7.5, 5, and 2.5. Here, a C/G ratio of 1 was not included in the experimental design on the basis of the polydispersity observed in the thermal citrate case.

The reverse thermal citrate method did not show a significant trend with respect to particle sizes and the C/G ratio. While the expectation was that particle sizes would increase as the C/G ratio decreased for all samples, this was only observed at a C/G ratio of 2.5 where the average size increased by approximately 10 nm. Additionally, equivalent C/G molar ratios in the reverse thermal citrate case did not yield signifcantly smaller particle sizes when compared to the thermal citrate method. In fact, in certain cases the particle sizes for each method were practically within error of one another. An example of this observation being a C/G ratio of 10 where it was found that the thermal citrate method produced 14.5±1.9 nm particles while the

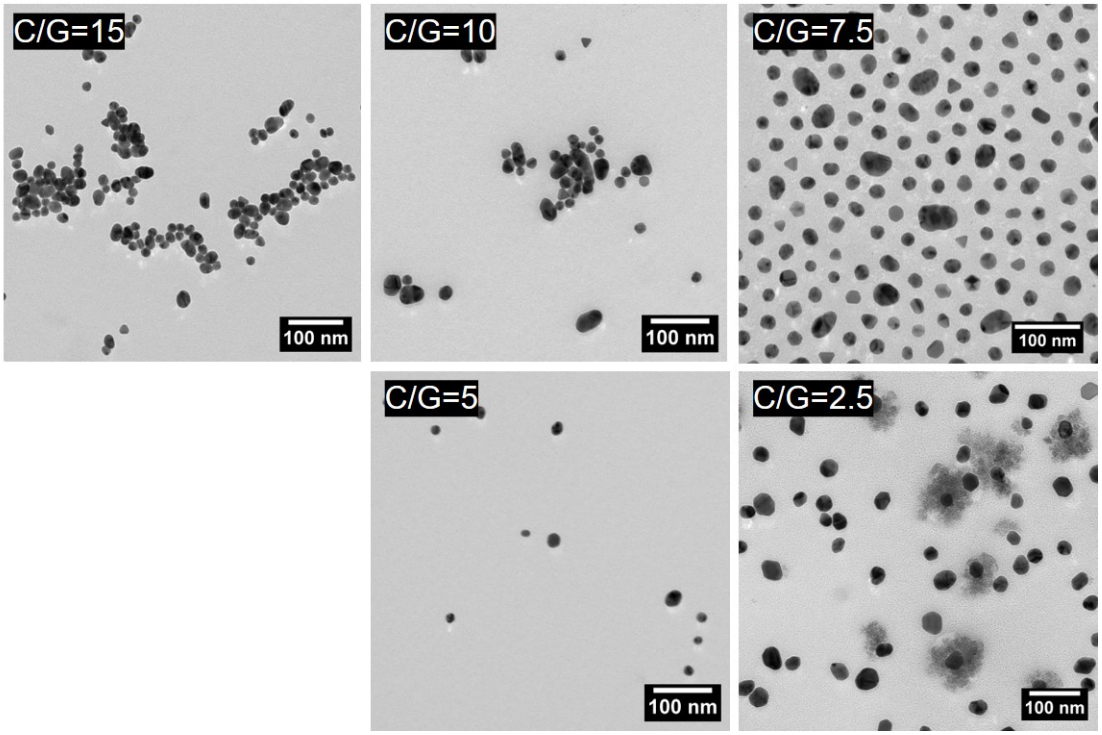

Figure 3.3: TEM micrographs showing size and morphology of AuNPs synthesized with reverse thermal citrate methodology and varied C/G ratio. The author would like to acknowledge Kathleen Mingle for taking the TEM images.

Table 3.2 AuNPs for Reverse Thermal Citrate Method

C/G Ratio	**Avg. Size (nm)**	
	CellProfiler	**Manual**
15	19.4±3.2	19.0±3.2
10	17.3±2.2	17.5±1.8
7.5	22.9±2.7	21.1±3.8
5	19.6±3.1	19.2±3.1
2.5	32.8±4.6	32.4±4.6

reverse thermal citrate method produced 17.3±2.2 nm particles. TEM images of the AuNPs prepared using modified reverse thermal citrate conditions are shown in Figure 3.3. The particle size analysis for each C/G ratio is shown in Table 3.2, where sizes were calculated both manually and using CellProfiler.

Room-Temperature $NaBH_4$-Assisted Method

A final AuNP preparation technique which was investigated was the room temperature $NaBH_4$ assisted method, where the goal was to augment the methodology such that AuNP colloids of larger diameter could be synthesized. To this end, the synthesis technique was modified such that the $HAuCl_4$ concentration was varied from 0.1-0.2 M and the C/G molar ratio was varied from 1.5-4.5. TEM images of the AuNPs prepared using modified reverse thermal citrate conditions are shown in Figure 3.4 and the particle size analysis for each C/G ratio is shown in Table 3.3, where sizes were calculated both manually and using CellProfiler. Irregular sizing and morphology of the AuNP colloids was observed when the higher $HAuCl_4$ concentrations of 0.15 and 0.2 M were used, and a formal particle size analysis was not completed for this reason.

Examination of Figure 3.4 shows that the use of 0.15 M $HAuCl_4$ led to a bimodal distribution of particles including small spheres and large cubes exceeding 50 nm. In the case of 0.2 M $HAuCl_4$ irregular particle morphology and aggregation was observed. It is possible that higher $HAuCl_4$ concentrations lead to higher ionic strength solutions which require increased C/G ratios or $NaBH_4$ concentrations to produce stable monodisperse colloids. Increasing the C/G ratio in the case of 0.1 M $HAuCl_4$ afforded interesting results with respect to particle sizes where the AuNP diameter increased when C/G was increased from 3 to 4.5, but decreased when C/G was increased from 1.5 to 3. It should be noted, however, that the differences in particle sizes for the AuNPs synthesized using C/G ratios of 3 and 4.5 were nearly within error of one another. Thus, a diminishing return on particle size control past a C/G ratio of 3 for the room temperature $NaBH_4$ assisted method could possibly explain the abnormal relationship observed with respect to C/G ratio.

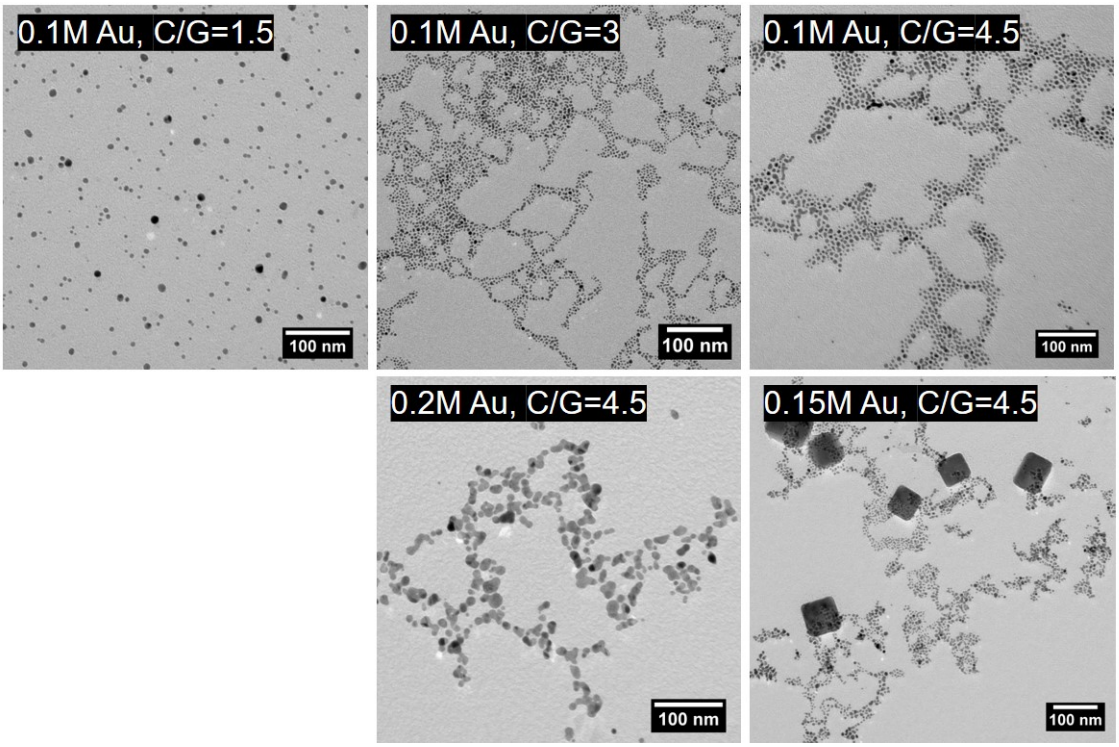

Figure 3.4: TEM micrographs showing size and morphology of AuNPs synthesized with citrate and $NaBH_4$ at room temperature. The author would like to acknowledge Kathleen Mingle for taking the TEM images.

Table 3.3 AuNPs from Citrate/$NaBH_4$ Method

[Au] (M)	C/G Ratio	Avg. Size (nm)	
		CellProfiler	Manual
0.1	**1.5**	10.3±3.8	9.93±1.7
0.1	**3**	3.8±0.9	3.77±0.5
0.1	**4.5**	6.8±2.1	7.07±1.7
0.2	**4.5**	*Didn't analyze	
0.15	**4.5**		

3.2.3 Polyacrylic Acid Synthesis

Reversible Addition-Fragmentation Chain Transfer (RAFT) is a commonly employed living free radical polymerization technique which proceeds through a degenerative chain transfer process mechanism.[77] Due to the versatility of RAFT for the polymerization of a large number of monomers it is frequently applied in a number of applications.[78–81] RAFT is unique from other radical polymerization techniques in that a kinetic control mechanism is operative in controlling the extent of polymerization where the radical is reversibly trapped throughout chain growth rather than radical-radical terminations which are central in other techniques. In addition, RAFT employs dithioester or trithiocarbonate chain transfer agents which facillitate this process via the formation of carbon centered radicals which are able to undergo β-scission or rearrange to form a leaving group. These molecules can be tailored via their Z or R group to yield the desired chemistry and polymer end group functionality, making RAFT ammenable to the fabrication of many unique structures which are inaccesible by other commonly used polymerization techniques like atom transfer radical polymerization (ATRP).[77]

Here, the RAFT polymerization methodology reported by Liang and coworkers was modified in the polymerization of tert-butyl acrylate (tBA) to yield polymers with a large range of molecular weights, ranging from 11 to 397 repeat units.[66]

RAFT Polymerization of tert-Butyl Acrylate

Typically, the RAFT polymerization was carried out using the following procedure.[66] 226.8 mg (0.90 mmol) of methyl-2-(butylthiocarbonothioylthio)propanoate, 14.8 mg (0.90 mmol) of AIBN, and 5.2 ml (36 mmol) tBA liquid monomer were stirred in a round bottom flask for 30 minutes while purging with argon. Reagents were purified prior to use, which included the removal of 4-Methoxyphenol (MEHQ) inhibitor from the tBA monomer using a basic alumina column and the purification of AIBN through

Table 3.4 ptBA Samples from RAFT Polymerization

Sample Key	TBA/CTA	Mn	PDI	N
ptba14a2	16.7	1711	1.06	11.4
ptba5g1	39.4	4834	1.15	35.8
ptba87a1	97.5	9283	1.11	70.6
ptba87a2	127.1	14673	1.05	112.7
ptba87a3	155.5	15663	1.05	120.4
ptba160a1	178.8	24533	1.15	189.7
ptba87a4	179.8	19370	1.06	149.4
ptba160a3	288.2	31552	1.08	244.5
ptba160a2	390.6	51061	1.15	396.9

recrystallization in methanol. After purging the air from the volumetric flask, the mixture was heated to 55 °C until the stir bar stopped indicating that the polymerization was complete. At this time, the hot mixture was quenched using liquid nitrogen. Subsequently, the ptBA was dissolved in a small volume of THF and precipitated using an excess of a cold methanol/water (1/1) mixture. The precipitated polymer was then isolated by decanting the methanol/water mixture and then dried under vacuum at room temperature for 12-18 hours.

Control over the molecular weight of the polymer was elicited by adjusting the molar ratio between the tBA monomer and chain transfer agent (tBA/CTA ratio). For the tBA/CTA ratio employed in the polymerization described above, a polymer with 35.8 repeat units was prepared. This ratio should, in principle, be equivalent to the number of repeat units in the polymer chains since each chain contains just one CTA molecule. Table 3.4 shows the molecular weights (Mn), polydispersion indices (PDI), and calculated number of repeat units (N) measured for each tBA/CTA ratio studied as measured with GPC. The results are shown graphically alongside the theoretical maximum in Figure 3.5.

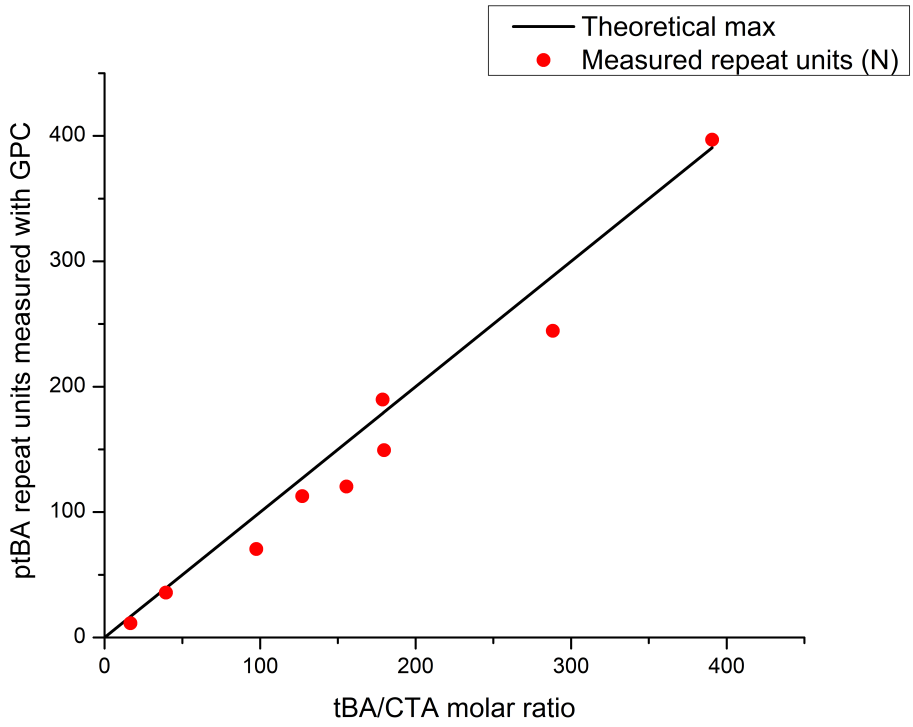

Figure 3.5: Number of tBA repeat units (N) in pTBA samples prepared with RAFT polymerization and varied tBA/CTA ratios. The black line is the theoretical maximum.

Acid Hydrolysis of poly-tert-Butyl Acrylate

Following the RAFT polymerization of tBA, the acrylate groups on the ptBA polymers were hydrolyzed to form PAA. The acid hydrolysis methodology employed was adapted from Wu and coworkers where a solution containing 20 mL of 1,4-dioxane, 2.5g of ptBA, and 3 mL of 37% fuming HCl solution were heated under reflux to 101 °C for >5 hours until a visible layer of tert-butyl alcohol could be seen.[82] The tert-butyl alcohol was then evaporated while stirring at 190 °C and the PAA was isolated via precipitation with ether. The PAA was then dried under vacuum for 12-18 hours after the ether had been decanted.

Preparation of Funtionalized PAA-AuNPs

Finally, the prepared PAA was used to functionalize the AuNP colloids by dissolving 15 mg of PAA in a 3 mL aqueous solution containing 0.1 M $NaHCO_3$.[66] This solution was then added to 100 mL of as-prepared aqueous AuNP solution containining 5 mg of AuNPs. After stirring the combined PAA and AuNPs for 12-18 hours the PAA-AuNP samples were purified and concentrated via repetitive ultracentriguation (100,000 g for 1 hour) and washing with DI water (3x).

3.2.4 Characterization of Funtionalized PAA-AuNPs

For each PAA-AuNP sample, measurements of polymer length with GPC, nanoparticle size distribution with TEM, and concentration with UV-Vis were obtained. More extensive characterization was completed for a single PAA-AuNP sample prepared with 5.98 nm AuNPs and PAA with 35.8 repeat units which included a determination of hydrodynamic radius before and after grafting of PAA using DLS as well as a measurement of PAA grafting density using TGA.

Determination of Hydrodynamic Radius

Hydrodynamic radius was measured for the PAA-AuNP sample prepared with 5.98 nm AuNPs and PAA with 35.8 repeat units both before and after the PAA was grafted. This was accomplished by varying the concentration of each sample and calculating the hydrodynamic radius based on the DLS size distribution measured in the concentration range where the result was least dynamic. The results of the DLS analysis of hydrodynamic radius are shown in Figure 3.6. It was found that after functionalization of the citrate capped AuNPs the hydrodynamic radius changed from 4.92 nm to 8.16 nm.

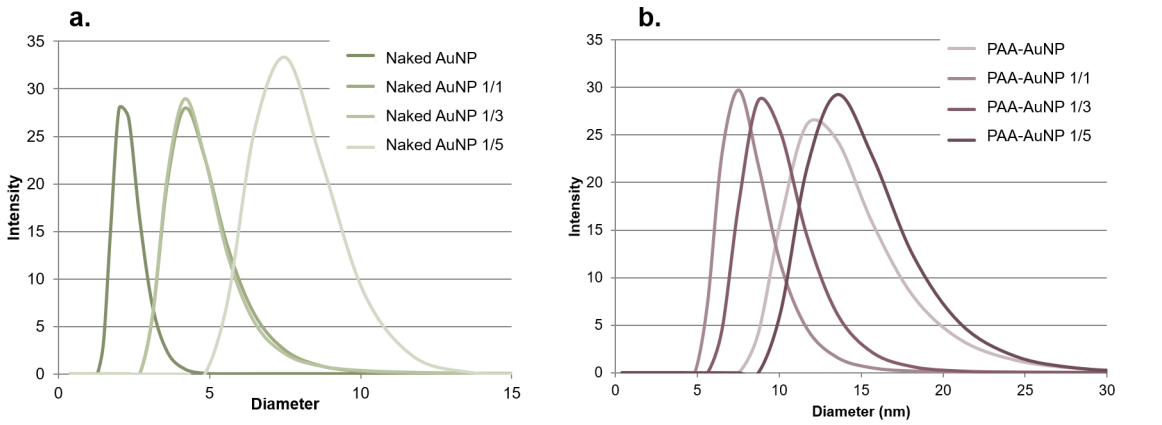

Figure 3.6: DLS determination of hydrodynamic diameter of 5.98±0.18 nm AuNPs a) as synthesized/citrate capped and b) capped with 35.8 repeat unit PAA. The author would like to acknowledge Kathleen Mingle for performing the DLS experiments.

Determination of Grafting Density

The grafting density of PAA on the AuNP surface was determined for the PAA-AuNP sample prepared with 5.98 nm AuNPs and PAA with 35.8 repeat units using a TGA-50 Shimadzu Thermogravimetric Analyzer with a TGA-50H detector. The experimental details were as follows. The weigh boat and balance were tared, 0.716 mg of PAA-AuNP sample was added and the sample was heated under argon from room temperature to 80 °C at 15 °C/min. The sample was then held at 80 °C for 30 minutes such that the temperature could stabilize and volatile organic residues could be removed. The sample was then heated from 80-800 °C at 10 °C/min such that the thermal decomposition of the PAA could be detected via mass loss, as shown in Figure 3.7. The total mass loss of the sample was then used to determine the composition of the PAA-AuNPs (35.8N, 5.98±0.18 nm) to be 11.76% PAA and 88.24% Au.

The composition of the PAA-AuNP sample determined with TGA was then used to determine the PAA grafting density in units of PAA chains/particle and PAA chains/nm^2 using knowledge of the AuNP diameter and PAA polymer length obtained from TEM and GPC studies, respectively. This involved using the AuNP surface area

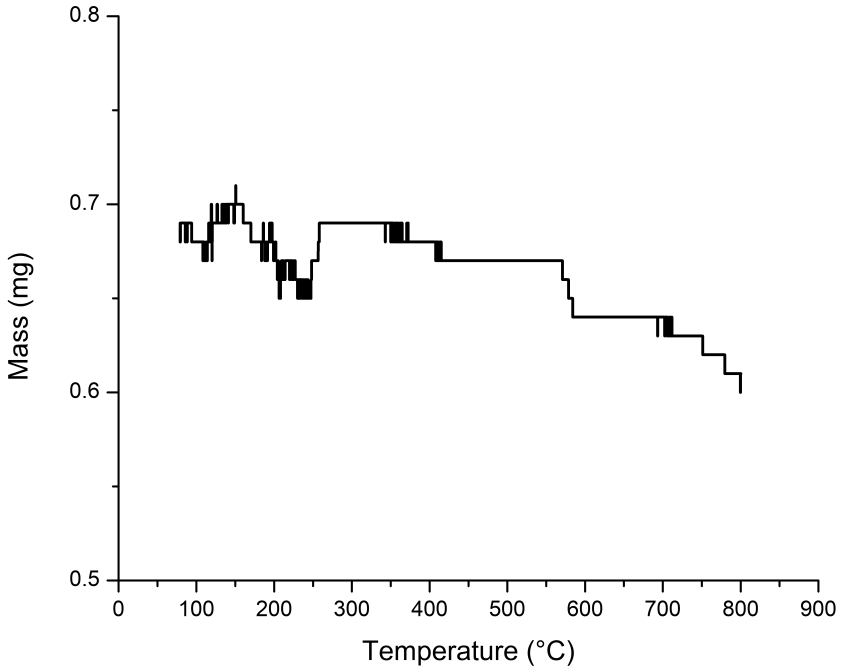

Figure 3.7: TGA profile of PAA-AuNPs. The author would like to acknowledge Kathleen Mingle for performing the TGA experiment.

and volume calculated based on the AuNP diameter together with density of Au metal (ρ_{Au}), 19.32 g/cm^3, to determine the Au particle mass. The PAA mass was then determined based on the Au particle mass and the TGA determined composition. The number of PAA chains per particle, 65.3, and the number of PAA chains/nm^2, 0.58, were then calculated using the PAA mass and molecular weight determined with GPC. This measurement of grafting density is within expectations, where other grafting density measurements of thiolated ligands to gold surfaces have been reported in the range of 0.04-4.35 chains/nm^2.[66, 83, 84]

3.2.5 Central Composite Design of Experiment

Using the discussed synthesis and characterization techniques, we were able to produce the nine NP samples quoated in Table 3.5.

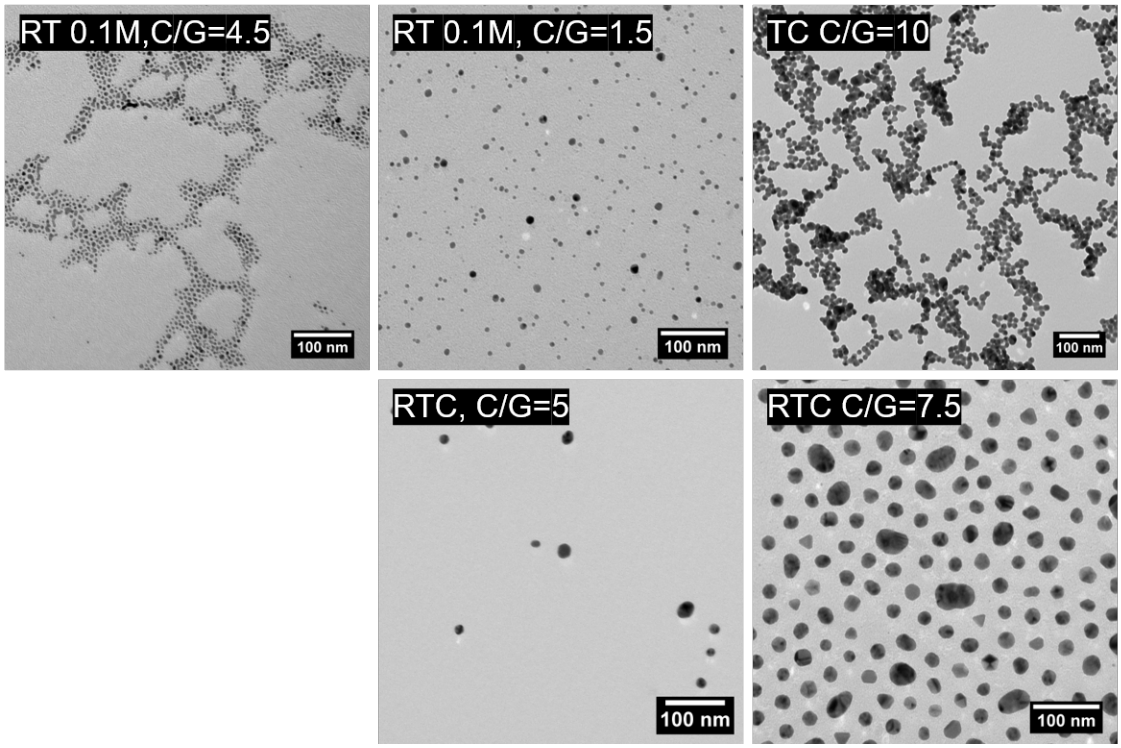

Figure 3.8: TEM images of selected AuNPs for central composite design.

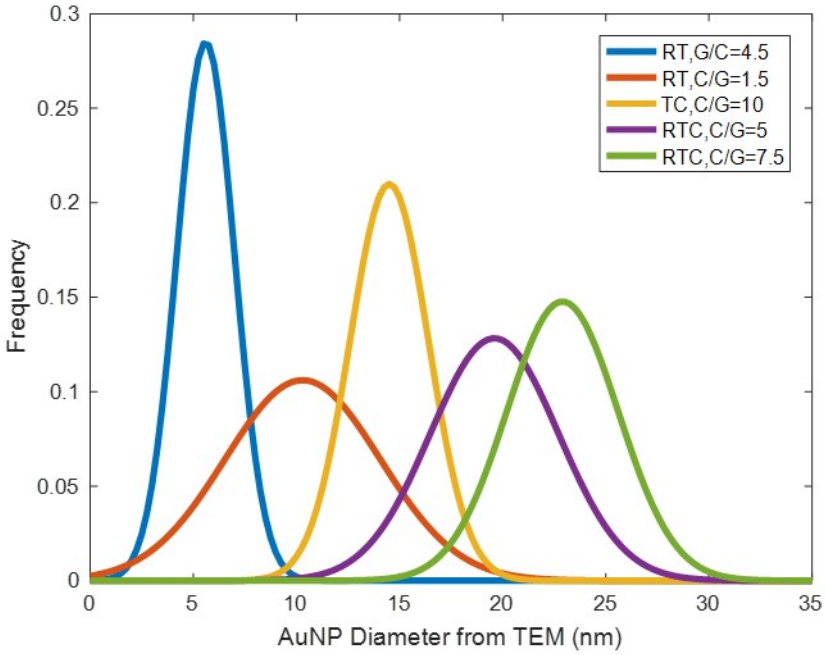

Figure 3.9: Size distributions generated with CellProfiler of selected AuNPs for Aβ aggregation experiments.

Table 3.5 NP CCD Properties

Sample	Design Point Type	Design Points		Experimental Points			
		N	D (nm)	N	PDI	D (nm)	σ (nm)
1	**Factorial**	36	9.2	36	1.15	10.3	3.8
2		112	9.2	113	1.05	10.3	3.8
3		36	19.8	36	1.15	19.7	4.2
4		112	19.8	113	1.05	19.7	4.2
5	**Axial**	11	14.5	11	1.06	14.5	1.9
6		136	14.5	139	1.05	14.5	1.9
7		74	5.8	71	1.11	5.6	1.4
8		74	23.2	71	1.11	22.9	5.0
9	**Center**	74	14.5	71	1.11	14.5	1.9

We were aware of what part of the design space we were trying to sample with the CCD. However, synthesizing the exact properties that we intended proved quite difficult. Nonetheless, by relaxing our exact center point, levels and α value we were able to first synthesize the nine samples in Table 3.5 and then redefine our design points to best fit the experimental points and distributions. The results of this process are plotted in Figure 3.10.

3.2.6 Aβ Aggregation Assay

The effect of the nine configurations of PAA-functionalized AuNPs on Aβ aggregation was assessed via flourescence detection. Thioflavin T (ThT) is a flourescent dye and molecular rotor that displays increased flourescence upon its selective binding to β sheet structures in Aβ.[52, 85] ThT was purchased from Sigma-Aldrich. Aβ monomer (1-42 isoform) was purchased from Peptide 2.0 and purified using size exclusion chromatography. Samples were loaded into 96-well plates with the perimeter wells left empty as with our experimental arrangement, anomalous readings were occasionally observed in these wells. Excluding the 36 perimeter wells left 60 wells that were loaded with 10 μM Aβ, 40mM tris (pH 8.0), 20 μM ThT and either 0 or 150 mM NaCl. Wells also included one of the nine NP samples at a concentration of 1 nM except for several left without NPs which served as controls. This amounted

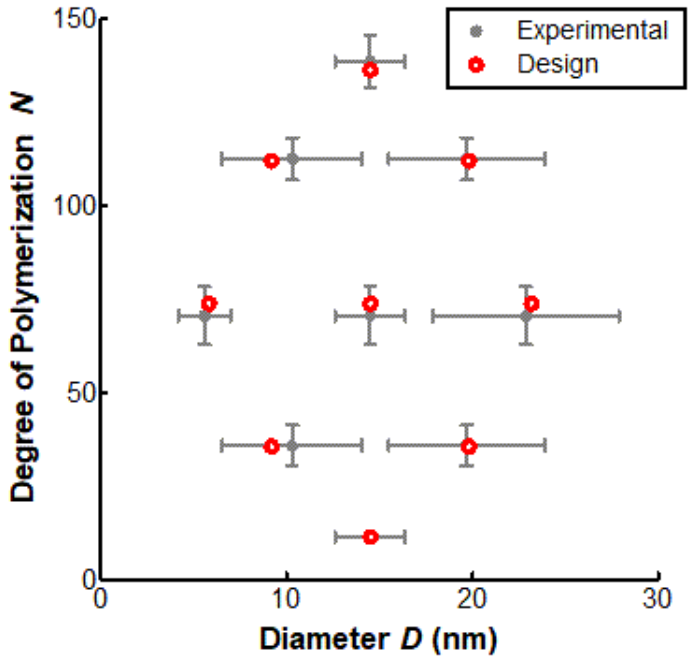

Figure 3.10: CCD of PAA-functionalized NPs with degree of PAA polymerization N plotted versus NP core diamater D. Experimentally measured points are plotted as gray circles with horizontal error bars indicating standard deviation of D and vertical error bars indicating PDI of PAA. Open red circles indicate design points used for analysis of experimental results.

to 10 unique samples with 0mM NaCl and another 10 with 150 mM NaCl. Each of these 20 configurations was replicated 3 times in each experiment. A depiction of the plate layout used in these assays is shown in Figure 3.11.

Fluorescence measurements were taken using a Biotek Synergy 2 Microplate Reader at 15 minute intervals until plateau was reached for all samples. This plate reader was also configured to agitate the plate during the entire duration of the experiment. Lag time was quantified for each individual sample using a simple algorithm implemented in the Python programming language. This algorithm entails identifying the measurement indexed by i which maximizes the function $F_{i+1} - F_{i-1}$ for the data set. Lag time is then defined as:

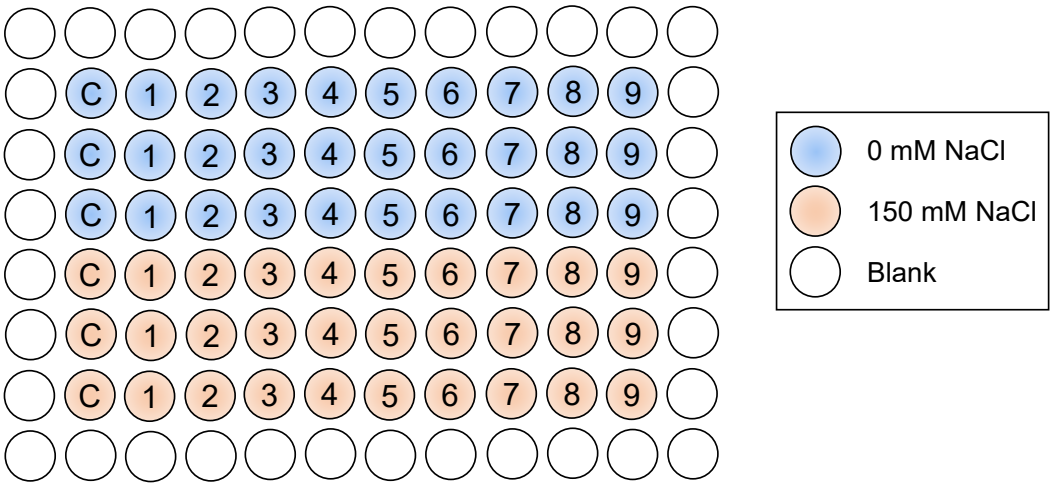

Figure 3.11: Layout of 96 well plate for Aβ aggregation assays. NP sample numbers are shown in their respective wells.

$$t_{lag} = \left(\frac{1}{n}\sum_{j=1}^{n} F_j - F_i\right)\frac{t_{i+1} - t_{i-1}}{F_{i+1} - F_{i-1}} + t_i \tag{3.1}$$

Here, n has been set to 4 thus specifying the baseline fluorescent signal as the average fluorescence observed in the first hour of aggregation. This methodology essentially amounts to the discrete analogue of the definition of lag time for idealized sigmoidal growth curves as explained and depicted elsewhere.[86] A schematic of this algorithm in practice is shown for sample data in Figure 3.12.

At this point, plots of flourescent signal as a function of time were generated and subjected to visual inspection for anomolous behavior. This is a process that needs to be conducted with care to avoid excluding physically relevant data. To assuage this risk, plots for individual samples were only excluded from further analysis when they exhibited unequivocal deviation from accepted behavior or the wells were improperly prepared. For several experimental data points, ThT was erroneously omitted from a well and for others aggregation proceeded to an extent in excess of all other wells

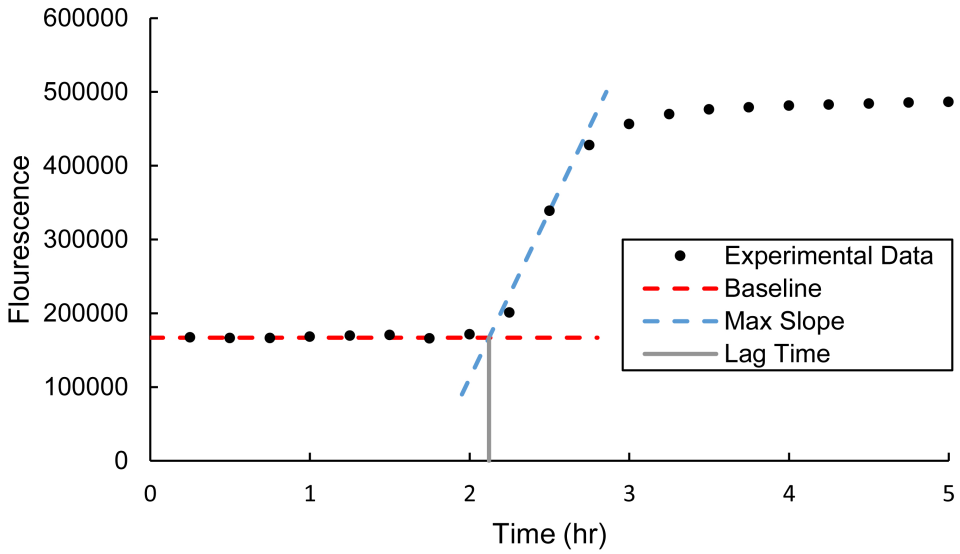

Figure 3.12: Lag time determination for sample aggregation data. Lag time is defined as the time at which tangent of the point with the greatest time derivative of flourescence intersects the baseline flourescence.

on the plate by a factor greater than two. This latter situation may be explained by a preformed nuclei present in the stock Aβ solution having been transferred to a well. In such a situation, the flourescence cannot be reliably compared to others on the same plate. It should be noted that for the previously stated reasons, only 3.0% of the flourescence curves were excluded.

Following data acquisition and screening, all calculated lag times for a given NP sample and salt concentration were averaged and normalized to the average of the corresponding controls. In proceeding discussions we refer to the resulting normalized, average value as lag extension factor.

3.3 Experimental Results and Discussion

3.3.1 Results

We performed the described Aβ aggregation assay on the nine NP samples of the CCD a total of five times. The results for the lag extension factor as well as the standard error of mean are shown in Figure 3.13.

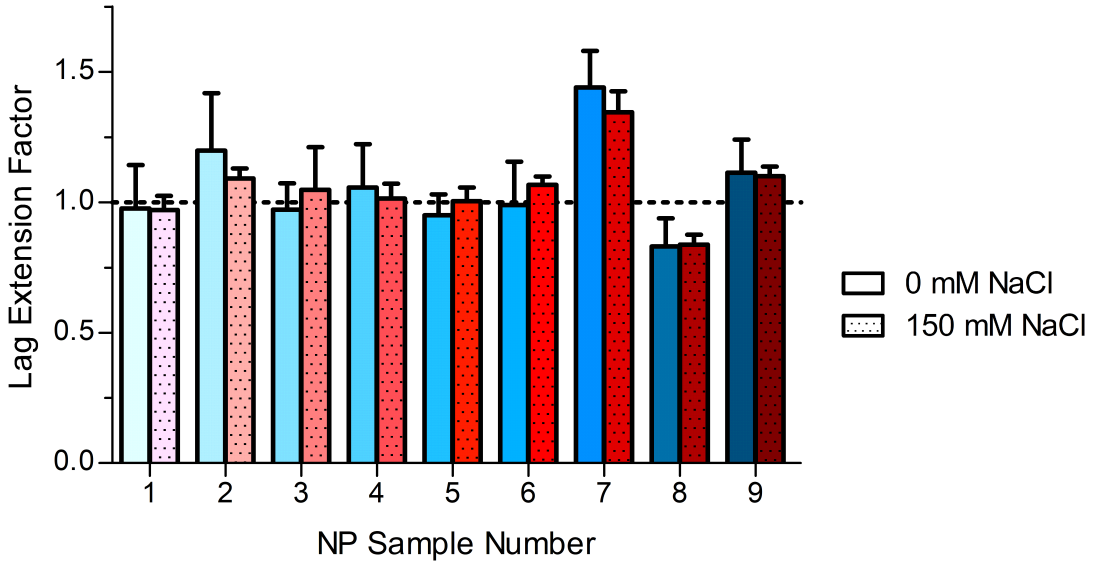

Figure 3.13: Lag extension factor for the nine NP samples of the CCD. Blue, unpatterned bars represent lag extension factor for the 0 mM NaCl while red, dotted bars indicate that for 150 mM NaCl. Both data sets were obtained at pH 8.0. Error bars represent the standard error of the mean.

Immediately, one can tell from Figure 3.13 that the 0 mM NaCl experiments generally featured more variability across all samples. This is true for all samples excepting sample number 3. The most efficacious NP samples were sample numbers 7, 2 and 9 (in descending order) and for these samples, lag extension factor was greater when the solution contained 0 mM NaCl versus 150 mM NaCl. In spite of the differences between the low and high ion concentration cases, the means do appear to trend together. In fact, there was only one sample which displayed a disparate effect between inhibition and promotion when comparing the low and high ion concentration cases (sample number 3). It should be noted that, for this sample, neither effects were statistically significant.

To further analyze the data, we performed a regression analysis to elucidate any potential relationships between the independent variables and the response. The regression analysis revealed that N, D and N^2 had significant effects on the lagtime

extension factor. Equation 3.2 shows the regression model fit for the experiments conducted at 0 mM NaCl in coded units.

$$LEF_{0\ mM\ NaCl} = 1.1145 + 0.0502N - 0.1225D - 0.0476N^2 \tag{3.2}$$

The most significant effect on lag extension factor was the diameter of the NP. The coefficients of Equation 3.2 indicate that the nature of this effect was such that increasing NP diameter decreased lag extension factor. The degree of polymerization N and N^2 were also significant effects for 0 mM NaCl though to a lesser extent than D.

The same protocol was used to conduct a regression analysis on the data obtained for 150 mM NaCl. This analysis revealed that only D had a significant effect on the lagtime extension factor. Equation 3.3 shows the regression model fit for the experiments conducted at 150 mM NaCl in coded units. In this instance, only the D had a significant effect on the lag extension factor. Equation 3.3 shows the regression model fit for the experiments conducted at 0 mM NaCl in coded units.

$$LEF_{150\ mM\ NaCl} = 1.0532 - 0.0884D \tag{3.3}$$

The results of the two regression model equations are shown in the contour plots of Figure 3.14.

3.3.2 Discussion

The first point to raise in the discussion of these experimental results is in regards to the efficacy of NP sample 7. This NP sample bore the smallest gold core diameter (D

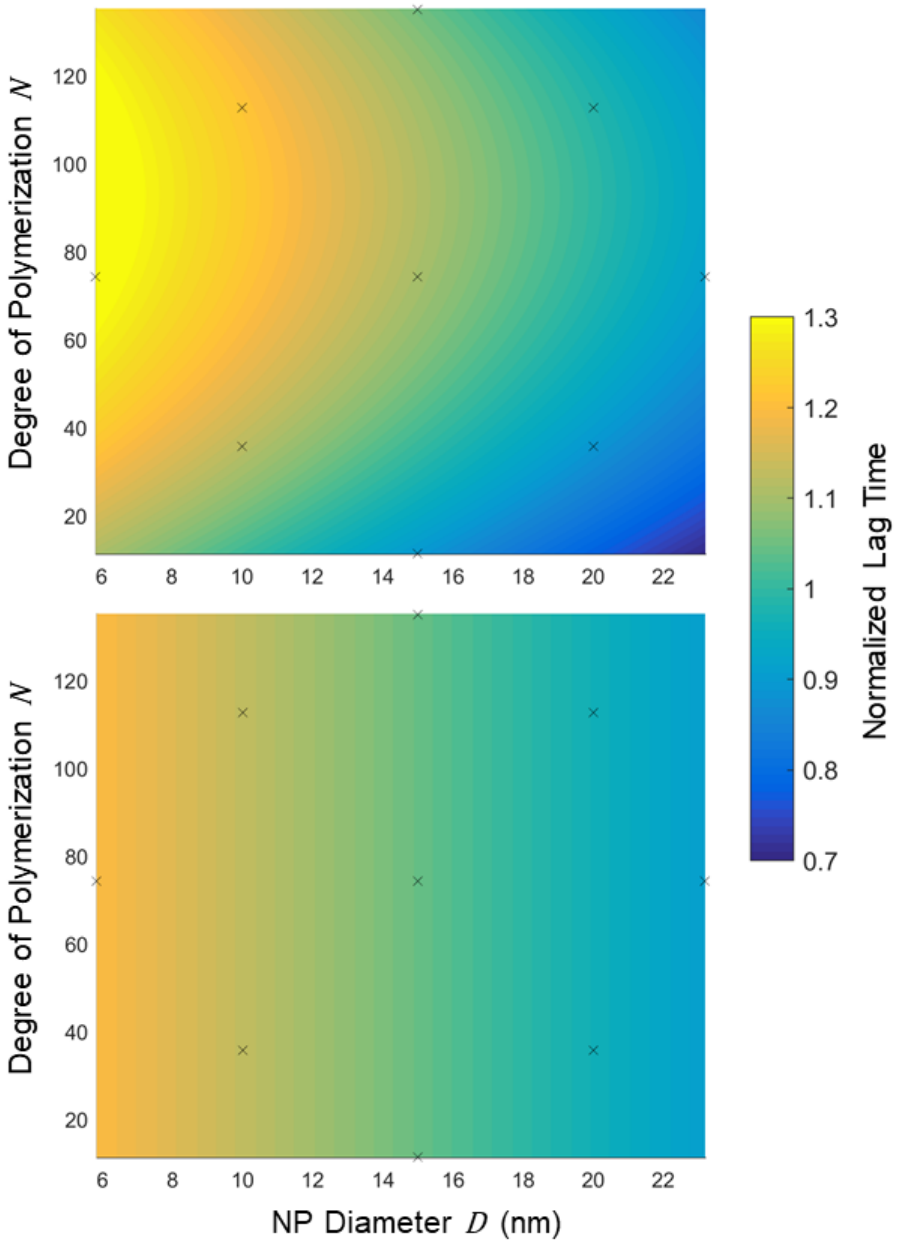

Figure 3.14: Contour plots of degree of polymerization (N) versus NP diameter (D) for the regression analysis of the NP CCD data. In these plots, the model predictions for lag extension factor are rendered different colors according to the color bar at right. The top subplot shows the regression model for 0 mM NaCl while the bottom subplot shows that for 150 mM NaCl. Both data sets were obtained at pH 8.0. Design points are represented by x's on the contour plot.

= 5.8 nm) and the central degree of polymerization ($N = 74$). This configuration of NPs in particular bore a significant increase in lag time extension with a sample mean of 1.44 for the 0 mM NaCl case and 1.35 for the 150 mM NaCl case. This result is noteworthy as it indicates that we were able to use essentially the same chemistry for the materials of construction but change the molecular architecture on the surface of the gold NPs and, for certain configurations of physical properties, preserve the lag extending behavior that originally piqued our interest in this system. Furthermore, it should be emphasized that this effect has been achieved with stoichiometric ratios of NP to Aβ of 1:10,000 which is a remarkable potency for an Aβ aggregation inhibitor molecule.

Both the raw Aβ aggregation data of Figure 3.13 and the results of the regression analysis, Figure 3.14, show that there is greater variability in lag extension factor for the 0 mM NaCl case than for the 150 mM NaCl case. Another fact that was mentioned in Chapter 2 is that Aβ aggregates more rapidly in the presence of greater ion concentration.[51] This effect was also observed in the raw lag times calculated from the flourescence curves. These macroscopic observations are consistent with the microscopic phenomenon of altered electrostatic screening. It should be mentioned that in the case of 0 mM NaCl, the solution still possesses ions capable of effecting electrostatic screening including the aqueous hydronium and hydroxide ions as well as the tris buffer molecule which is capable of bearing net charge depending on its protonation state. Additionally, there is inevitably some concentration of chloride ions in solution that enter with the addition of tris-hydrochloride that is mixed with the tris free base in order to achieve the desired solution pH of 8.0. Nonetheless, the difference in effective ionic strengths between the two cases has a profound effect on both lag extension effects of the NPs.

Equations 3.2 and 3.2 as well as the contour plots presented in Figure 3.14 indicate that there was a striking difference in statistically significant effects for the lag

extension factor. What was true for both cases (0 and 150 mM NaCl) was that reducing NP diameter increased lag extension factor. This independent variable had the greatest standardized effect for both cases. One possible explanation for this trend across the CCD space could be a disparity in diffusivities of the NPs. While a neither a direct nor indirect measurement of diffusivity has been made at this point for any of the NP samples, one could reasonably assert that the diffusivity of 5.6 nm diameter NPs exceeds that of 22.9 nm diameter NPs and that the there exists a proportional gradient in between thes points. Furthermore, the difference in NP diameter dictates the radius of curvature that the PAA molecules are equilibrating in local to the NP surface. If one were to hold the degree of polymerization and grafting density of PAA fixed and increase the diameter of a NP, the PAA would essentially become increasingly squeezed in a manner dependent on distance from the NP surface. This effect is similar to the behavior of the bristles of a rug as it is rolled. Though the analogy features a cylindrical geometry rather than the spherical geometry of the real system, the principle holds true. This effect will be discussed further in a subsequent analysis. For the present discussion, it should suffice to acknowledge that the described curvature effect will result in disparate equilibrium molecular organization for PAA featuring different effects on solution and abilities for Aβ to intercalate within the polymer array.

The effect of the degree of polymerization of PAA on lag extension is more difficult to immediately rectify with physical intuition than that of NP diameter. Equation 3.2 indicates that both N and N^2 have a significant effect on the lag extension factor for 0 mM NaCl. This relationship implies that lag extension factor will be maximized when the degree of polymerization is approximately 93. The emergence of a predicted optimum under these conditions is intriguing for several reasons.

The emergence of a novel phenomenon in general for the low ionic concentration condition could be explained as before as the result of a reduction in electrostatic

screening revealing a polymer effect that was previously too dull to be statistically significant. The fact that this would occur with degree of polymerization but not with NP diameter is also unsurprising. The influence of the electrostatic properties of the bulk solution on the characteristic physical size and spatial extent of influence of the functionalized-NP system will be more sensitive to the length of PAA on the surface than the diameter of the metal core. This is because PAA is capable of being charged, the degree to which it is of course being a function of the solution in which it is bathed, and it is capable of changing its ensemble average shape in response. Though a metallic NP is capable of accruing charge, it will not significantly rearrange its shape in response.

The fact that the phenomenon that emerges upon the reduction of bulk ion concentration is an optimum degree of polymerization was not unexpected from an experimental perspective. A preliminary study testing NPs with three different degrees of polymerization had hinted to us that an optimum may exist for certain NP diameters. A theoretical explanation of this phenomonon is objectively more speculative. To aid in this analysis we have developed a theoretical model for the PAA on the surface of the NP.

Before ending the discussion of these experimental results it should be pointed out that undoubtedly more complex relationships exist between D and N and the lag time extension factor than is indicated by Equations 3.2 and 3.3 and presented graphically in Figure 3.14. It is the nature of the regression analysis methodology that in some cases constrains the powers of the independent variables to be evaluated and retains only those terms that are statistically significant. As an example of how these results may be misinterpreted without appreciating this concept, consider if one were to increase the degree of polymerization of PAA on the NPs by ten orders of magnitude. This would certainly have an effect on lag time; indeed the system may be better classified as a polymer melt at that point. Though Equation 3.3 does

not contain N it makes no prediction of the effect of that variable outside the design space. It is in this spirit that one should bear in mind that the regression analysis only allows us to make definitive statistical statements on the effects of the design space variables with positive integer powers. This aids us in the interpretation of the trends and curvature of the response surface. However, the best that we can produce with this methodology is an approximation. If one were to construct the *true* response surface by taking an infinite number of measurements, it would differ from Figure 3.14 due to the lack of similar natural constraints.

A Note on Comparison with Previous Studies

It is worth elaborating upon the disparity between the NP concentration used in the present study and that used in the original work by our group using electrostatically-associated PAA.[56] In this study, NPs were tested with a solution concentration of 1 nM while the concentration of Aβ used was 10 μM. However in the previous study, the Aβ concentration was held fixed at 40 μM while the NP concentration was varied from 200 pM to as low as 20 pM. Even at the lowest concentrations tested, the original study found that 8 nm and 18 nm PAA-functionalized NPs could inhibit aggregation over the course of the experiment. This observation constitutes a significantly higher observed efficacy than that tested in the present study.

The decision to use a higher concentration of NPs in the present study amounted to a compromise necessary to more efficiently sweep the design space. The essence of our reasoning is that we did not want to test the NPs at concentrations so low that we would question whether or not increasing their concentration would reveal an effect that had yet to present itself. The notion counterbalancing this logic was that if we tested NPs at concentrations higher than was necessary to see effects, we would not be able to tell how low we could reduce their concentration while preserving said effects. Our compromise was to perform an initial screening experiment (i.e. the present

study) to determine which parts of design space showed particular promise and to focus on those parts of design space in further work via dose-response experiments *et cetera*.

On a final note, it is not appropriate to draw direct quantitative comparisons between these two experimental designs. While the trends and correlations between these two studies certainly deserve examination and discussion, the fact that they were conducted years apart and with Aβ obtained from different suppliers precludes direct quantitative comparison with respect to potency and lag extension factor.

3.4 Self-Consistent Field Theory for Polyacid-Functionalized Nanoparticles

We have developed two SCFTs to model the PAA molecules on the surface of the NPs. These models account for the size, shape and charge properties of all of the species that were present in solution experimentally excluding Aβ . The only difference between the two models is the polymer model that is used. In one instance, we employed the rotational isomeric state model while the in another we employed the continuous Gaussian chain model. It is our goal to use this SCFT to gain a thermodynamic perspective on the equilibrium properties of the solution proximal to the functionalized surface and compare this understanding with experimental observations to clarify a mechanism of action.

3.4.1 Rotational Isomeric State Model

The rotational isomeric state model (RIS) is a polymer model for which the angle that is created between three consecutive polymer monomers is held fixed.[87] This polymer model is one that has been used by Szleifer and coworkers in many of their implementations of SCFT for different types of polymeric layers.[88–90] This

realization follows the classical formulation of the SCFT's developed by Szleifer for end-grafted polymeric layers much more closely than that used to model Aβ.[30]

Theoretical Development

We begin our derivation of the SCFT by writing another generalized free energy functional.

$$\begin{aligned}\frac{\beta F}{A(R)} = \frac{N}{A(R)}\sum_{\alpha} P(\alpha)\ln P(\alpha) + \int dr\ G(r)\beta\Big[\langle\rho_q(r)\rangle\psi(r) - \frac{1}{2}\epsilon_o\epsilon(r)\big(\nabla\psi(r)\big)^2\Big] \\ + \sum_{i=\{H_2O,Na^+,Cl^-,H^+,OH^-\}}\int dr\ G(r)\rho_i(r)\Big(\ln\rho_i(r)v_{H_2O} - 1 + \beta\mu_i^o\Big) \\ + \sum_{i=\{p,\,tr\}}\int dr\ G(r)\langle\rho_i(r)\rangle\Big[f_i(r)\Big(\ln f_i(r) + \beta\mu_{i,c}^o\Big) \\ + \big(1-f_i(r)\big)\Big(\ln(1-f_i(r)) + \beta\mu_{i,o}^o\Big)\Big] \qquad (3.4) \\ - \int dr\ G(r)\beta\Big(\sum_{i=\{Na^+,Cl^-,OH^-,tr\}}\mu_i\rho_i(r) \\ + \mu_{H^+}\Big(\rho_{H^+}(r) + f_{H^+,\,tr}\rho_{tr}(r) + f_{H^+,\,p}\langle\rho_p(r)\rangle\Big)\Big) \\ + \int dr\ G(r)\beta\pi(r)\Big[\langle\phi_p(r)\rangle + \sum_{i=\{H_2O,Na^+,Cl^-,H^+,OH^-,tr\}}\phi_i(r) - 1\Big]\end{aligned}$$

where $A(R)$ indicates the area of the NP surface. R represents the radius of the NP core. The first term contributing to the free energy accounts for the configurational entropy associated with the PAA molecules. Here, N is the total number of PAA molecules on the NP. $P(\alpha)$ indicates the probability of configuration α. In this formulation of an SCFT, which is similar in many ways to that employed for the Aβ model, we do not distinguish between different PAA molecules as we did for the case of Aβ. This is because we are invoking a more far-reaching and in fact more classical notion of a self-consistent field. Specifically, we focus on a single PAA molecule that is influenced by an external mean field representing the influence of all

other molecules that is *self-consistent* with respect to its own properties. In order to make this approximation, we enforce spherical symmetry. Accordingly, all physical properties vary only in the radial coordinate and all integrals are taken with the geometric factor $G(r) = (r/R)^2$ accounting for the geometry of coordinate system.

The second term in Equation (3.4) accounts for the free energy of electrostatic interactions. $\psi(r)$ is the electrostatic potential, ϵ_o the permittivity of free space and $\epsilon(r)$ the relative dielectric constant. We define the relative dielectric constant at r as a weighted sum of the average bulk relative dielectric constants of water ϵ_{H_2O} and PAA ϵ_p: $\epsilon(r) = \epsilon_p\langle\phi_p(r)\rangle + \epsilon_{H_2O}(1 - \langle\phi_p(r)\rangle)$. The dielectric constant has been taken to be 4.0 for PAA. Here, $\langle\phi_p(r)\rangle$ is the ensemble average volume fraction of PAA and can be expressed as:

$$\langle\phi_p(r)\rangle = \frac{N}{A(r)} \sum_{\alpha} P(\alpha) n_p(\alpha; r) v_{mon} \tag{3.5}$$

Where $n_p(\alpha; r)$ is the number density for configuration α at r and has dimension of per length. v_{mon} is the volume of an acrylic acid monomer. Using this definition we now define the ensemble average charge density:

$$\langle\rho_q(r)\rangle = \sum_{i=\{Na^+, Cl^-, H^+, OH^-\}} \rho_i(r) q_i + \langle\rho_p(r)\rangle f_p(r) q_p + \rho_{tr}(r) f_{tr}(r) q_{tr} \tag{3.6}$$

The total position-dependent charge density is the sum of the charged mobile species (Na^+, Cl^-, H^+, OH^-) multiplied by their respective charges, q_i. Note that all densities denoted with the symbol ρ have dimension of per length cubed. The charge contributed at a given position in space by the PAA molecules and tris molecules are accounted for in the final two terms. Both the PAA and tris molecules bear

chemical equilibrium sites that we represent as an average state of charge denoted by $f_p(r)$ and $f_{tr}(r)$. The relationships between fraction of charge and fraction of protonation are distinct for PAA and tris. For PAA, $f_p(r) = 1 - f_{H^+,\,p}(r)$ while for tris, $f_{tr}(r) = f_{H^+,\,tr}(r)$.

The third term in Equation (3.4) accounts for the translational entropy of all of the mobile species in solution. $\rho_i(r)$ denotes the density of species i at position r and v_{H_2O} the volume of the solvent molecule.

The fourth term in Equation (3.4) accounts for the free energy of chemical equilibria. $\mu^o_{i,c}$ and $\mu^o_{i,o}$ denote the standard state chemical potentials of the charged and neutral states of site i, respectively.[42] The incorporation of the tris molecule into this theoretical framework is unique due to the fact that it is both a mobile species and a site for chemical equilibrium. To our knowledge the incorporation of such a buffer model into this type of SCFT has never before been implemented.

At this juncture, we establish that the PAA molecules that we are treating within the SCFT are grafted at one of their ends to a smooth surface, by fiat fixing the number of PAA molecules in the system. However, all other species should be free to enter and leave the system effecting variation in their total quantity. To achieve this property, we constrain the chemical potentials of these species by subtracting these values from the free energy. This modification is manifest in the fifth term.

Finally, the remaining term of Equation (3.4) constitutes an enforcement of incompressibility at all positions in space through the field of Lagrange multipliers $\pi(r)$. In this context, these Lagrange multipliers represent the lateral pressure in the spherical shell specified by r.

Functional minimization of Equation (3.4) with respect to the densities of the mobile species leads to the following expressions for the mobile species:

$$
\begin{aligned}
\rho_{H_2O}(r)v_{H_2O} &= \exp\Big[-\beta\pi(r)v_{H_2O}\Big] \\
\rho_{H^+}(r)v_{H_2O} &= \exp\Big[-\beta\Big(\mu^o_{H^+} - \mu_{H^+} + \pi(r)v_{H^+} + \psi(r)q_{H^+}\Big)\Big] \\
\rho_{OH^-}(r)v_{H_2O} &= \exp\Big[-\beta\Big(\mu^o_{OH^-} - \mu_{OH^-} + \pi(r)v_{OH^-} + \psi(r)q_{OH^-}\Big)\Big] \\
\rho_{Na^+}(r)v_{H_2O} &= \exp\Big[-\beta\Big(\mu^o_{Na^+} - \mu_{Na^+} + \pi(r)v_{Na^+} + \psi(r)q_{Na^+}\Big)\Big] \\
\rho_{Cl^-}(r)v_{H_2O} &= \exp\Big[-\beta\Big(\mu^o_{Cl^-} - \mu_{Cl^-} + \pi(r)v_{Cl^-} + \psi(r)q_{Cl^-}\Big)\Big] \\
\rho_{tr}(r)v_{H_2O} &= \frac{1}{1-f_{tr}}\exp\Big[-\beta\Big(\mu^o_{tr^+} - \mu_{tr} + \pi(r)v_{tr}\Big)\Big]
\end{aligned}
\tag{3.7}
$$

Minimization of Equation (3.4) with respect to the ensemble average fraction of protonation of either tris or PAA yields the expression:

$$
f_{H^+,i}(r) = \frac{1}{1+\frac{K^o_{a,i}\phi_{H_2O}(r)}{\phi_{H^+}(r)}} \tag{3.8}
$$

As afore mentioned, there is a distinction between the chemical equilibria of PAA and that of tris. This distinction is manifest in the definition of the acid dissociation constant for the two species: $K^o_{a,p} = \exp[-\beta(\mu^o_{c,p}+\mu^o_{H^+}-\mu^o_{o,p})]$ for PAA while $K^o_{a,tr} = \exp[-\beta(\mu^o_{o,tr}+\mu^o_{H^+}-\mu^o_{c,tr})]$ for tris.

Minimization of Equation (3.4) with respect to the electrostatic potential yields the familiar Poisson equation:

$$
\epsilon_o\nabla\Big(\epsilon(r)\nabla\psi(r)\Big) = -\langle\rho_q(r)\rangle \tag{3.9}
$$

Minimization of the generalized free energy expression with respect to the probability of configuration α yields:

$$P(\alpha) = \frac{1}{Q}\exp\Big[-\int dr\ \rho_p(\alpha;r)\Big(\pi(r)+\ln(1-f_p(r))\Big)\Big] \times\ \exp\Big[\int dr\ \frac{1}{2}\beta\epsilon_o\frac{\partial\epsilon(r)}{\partial P_j(\alpha)}\Big(\nabla\psi(r)\Big)^2\Big] \tag{3.10}$$

Where Q represents the full single chain partition function.

We now generate chains using a Monte Carlo (MC) algorithm that is consistent with the RIS model but further restricts the polymer configuration space by randomly selecting only trans, gauche (+) or gauche (-) configurations for consecutive PAA monomers. Note that this type of treatment has coarse-grained the nature of the single-stranded carbon backbone such that the notion of trans and gauche has been abstracted to describe the relative positions of double the number of carbons when compared to the traditional sense. Nevertheless, an analysis of the steric considerations of PAA has indicated that including only these configurations is a reasonable assumption to make and greatly reduces the possible configuration space. Once a full configuration is generated, a check is made to ensure that the configuration does not overlap itself. Finally, the configuration undergoes random rigid body rotations that are only accepted if they do not penetrate the NP surface. In this way, a configurational ensemble of 10^6 configurations is generated.

As was the case with the SCFT used to model Aβ dimerization, the continuous Equations 3.5 through 3.10 are discretized in order to convert them into a system of equations. Specifically, the Poisson and incompressibility equations are the coupled non-linear equations to be solved and the lateral pressures $pi(r)$ and electrostatic potential $psi(r)$ are the independent variables. Space is discretized to 0.2 nm in the radial coordinate. Additionally, the polymer configurations are converted into a discretized representation, the number density $n_p(\alpha;r)$, by specifying that all of the volume of a PAA monomer is concentrated in the spherical layer in which the

center of that monomer unit is located. This system of equations is then solved using KINSOL.[48]

Results and Discussion

We have used the described SCFT with the RIS chain model to calculate the equilibrium properties of the PAA-functionalized NP system. We have specifically performed these calculations for NPs with a diameter of 14.5 nm, a degree of polymerization of 11 and a PAA grafting density of 0.58 nm^{-2}. These properties are consistent with NP sample number 5 from our CCD experiments. This sample condition was selected due to the fact that it bore the smallest PAA molecules of all of the NP samples. In fact, the RIS model can only accurately be applied to polymers of 20 monomer units or less. This is due to the exponential increase in size of the configuration space of the polymer. Although an ensemble of 10^6 configurations can accurately capture the behavior of polymers of 11 monomer units in length, so few configurations provide too sparse of a representation of the astronomical configuration space to be reliable. A sufficiently sized ensemble is easily verifiable. Too few configurations may manifest as the predicted equilibrium properties varying wildly for different ensembles of the same size. This was not the case for our calculation of NP sample number 5 though undoubtedly would be for any of the other samples.

We have solved the equilibrium expressions for a bulk pH of 8.0, a tris concentration of 40 mM and two separate salt concentrations: 0 mM and 150 mM NaCl. These conditions were selected to match those used in the CCD experiments. We discretized space in the radial coordinate to 0.2 nm spherical shells and treated space up to 10 nm away from the NP surface.

The volume fractions of PAA, Na^+, water, and tris at thermodynamic equilibrium have been calculated as a function of distance from the NP surface. These functions are plotted in Figure 3.15.

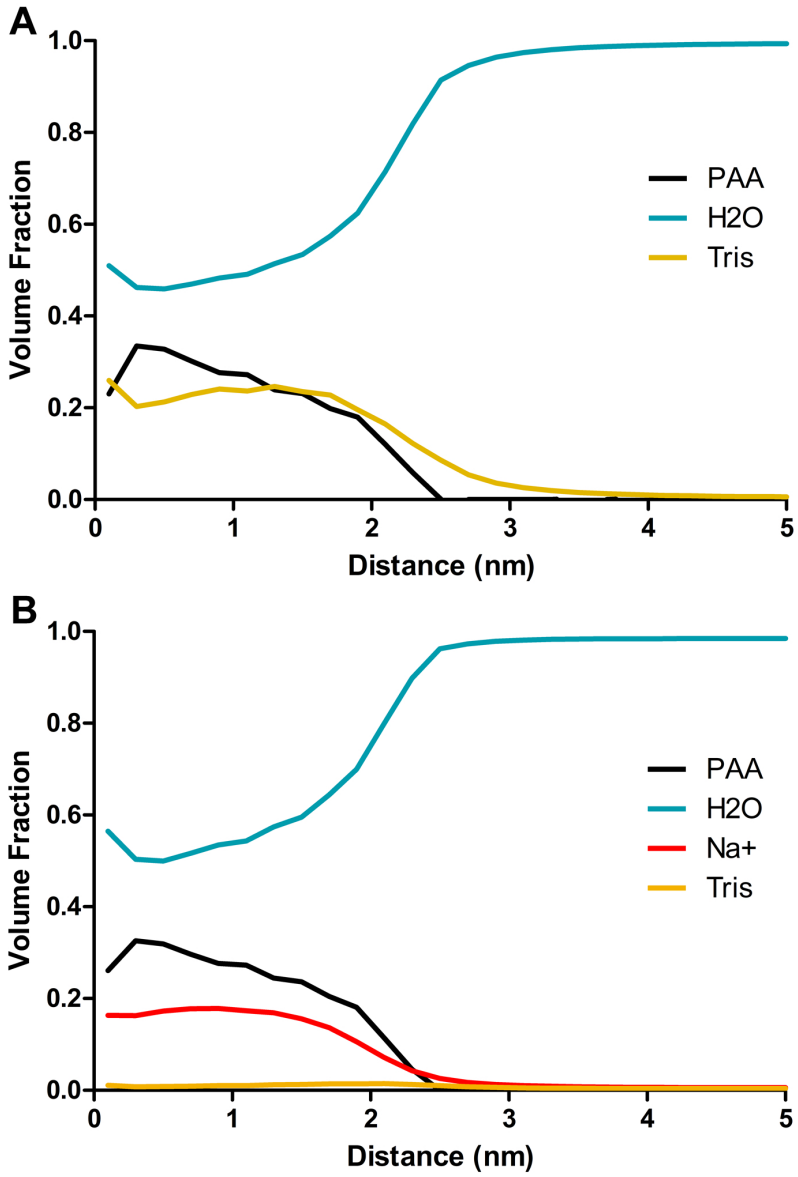

Figure 3.15: Volume fractions of molecular species as a function of distance from the NP surface calculated using the RIS chain model. Both plots show these results for a NP with a diameter of 14.5 nm, a degree of polymerization of PAA of 11 and a PAA grafting density of 0.58 nm^{-2}. Both plots have been calculated for a bulk pH of 8.0 and a temperature of 25 °C. Panel A shows the volume fractions for the case of a bulk concentration of 0 mM NaCl and Panel B for 150 mM NaCl.

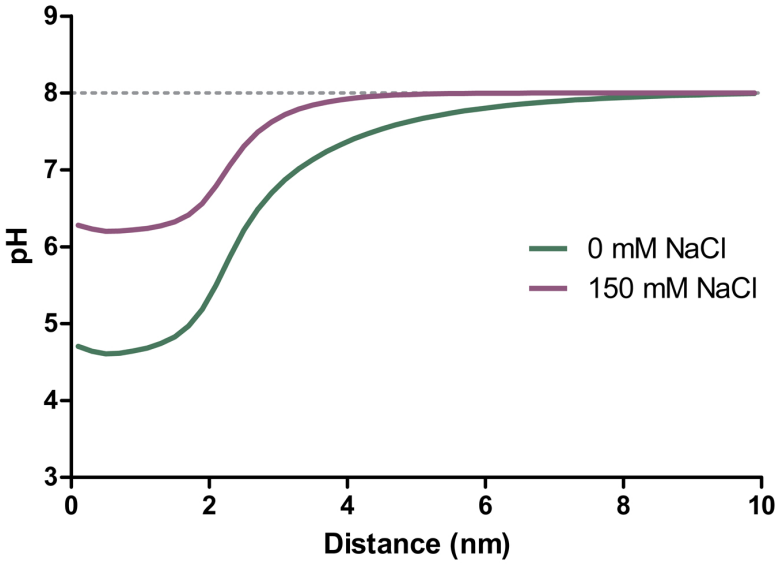

Figure 3.16: pH as a function of distance from the NP surface calculated using the RIS chain model. pH functions were calculated for a bulk pH of 8.0 (indicated by a dotted line) and a temperature of 25 °C.

The equilibrium concentration of hydronium ions, and consequently pH, as a function of distance from the NP surface have similarly been calculated and are plotted in Figure 3.16.

Figures 3.15 and 3.16 demonstrate very clearly the manner in which the system is responding to the localized negative charge present on the PAA. This localized negative charge effects energetically unfavorable electrostatic repulsions. The system has several mechanisms through which it can mitigate this situation, the extent to which it does so is dictated by the SCFT equations. The system can probabilistically favor more extended PAA configurations, in a sense, stretching the equilibrium polymer ensemble to keep the charges as far away from each other as possible. This phenomenon is counterbalanced by the unfavorable impact that it has on the configurational entropy of the polymer. Additionally, the system can localize counterions. Likewise, this effect is countered by the impact on the translational entropy of the counterions being localized as well as the need to push through the increased lateral pressure that

inevitably forms due to the presence of the PAA. Finally, the system can localize hydronium ions to shift the chemical equilibrium on the PAA molecules effectively neutralizing them. This final mechanism is at a comparatively great expense to the translational entropy of hydronium ions that will be incurred due to their extremely low concentration in bulk solution at pH 8. We observe that the optimal balance of these effects takes on distinct forms depending on the bulk concentration of NaCl.

In panel A of Figure 3.15, at 0 mM NaCl, a strong localization of tris molecules is apparent. However, due to the action of tris as a buffer, its state of charge is dependent on local pH. That is at higher pH, the fraction of tris molecules that are charged is higher. Conversely, at higher pH, a larger fraction PAA molecules are neutral. Furthermore, hydronium ions are positively charged; a property that can further mitigate the local negative charge effected by the presence of the PAA. For these three reasons, the system localizes a large amount of hydronium ions at the PAA molecules in effect shifting the chemical equilibrium of the tris and PAA to mitigate the energetically unfavorable electrostatic repulsions of the localized polyacid. This is evidenced by the drastic drop in pH as presented in Figure 3.16.

When there are more salt ions in solution, at 150 mM NaCl, the system mitigates the localized charge of the PAA much differently. We see in Panel B of Figure 3.15 that the system is preferentially localizing Na^+ near the surface over tris. In fact, there is very little localization of tris at all. This preference makes perfect sense in light of the fact that sodium ions are always charged whereas tris is charged to a fractional extent dependent on local pH. Additionally, the sodium ion is approximately one half of the size of the tris buffer molecule making it considerably less susceptible to expulsion from the polymer layer by the increased lateral pressure field. Finally, the bulk concentration of sodium ions exceeds that of tris making its localization less of a strain on its translational entropy. It also appears that the localization of sodium ions is more effective at mitigating the charge on the PAA in an overall sense. This

observation is supported by the higher minimum pH predicted for the 150 mM NaCl case. The more successful electrostatic counterbalancing by the sodium ions means that the system need not pull in as many hydronium ions to neutralize the PAA molecules.

A significant prediction made by this model is the large disparity in the spatial extent to which the pH is shifted from its bulk value. Figure 3.16 shows that the pH is shifted to a lower value and farther when there is no sodium present. This result is not surprising as the greater ion concentration will screen the influence of electrostatic charges more rapidly away from the charge. However, this theoretical prediction makes quantitative this qualitative intuition.

As was mentioned, the RIS model is unsuitable for use with the longer polymer lengths used for the other NP samples. We now therefore present the development of a similar SCFT utilizing the continuous Gaussian chain model which is suitable for arbitrarily long polymers.

3.4.2 Continuous Gaussian Chain Model

The continuous Gaussian chain model has a rich history of development and implementation and readers are referred to the excellent text by Fredrickson for more details.[91]

Theoretical Development

We shall now derive the equilibrium expressions the PAA-functionalized NP system making use of the continuous Gaussian chain model. We shall not assume from the outset that we are treating a spherically symmetric system. Our free energy functional in this case is written as:

$$
\begin{aligned}
\beta F = \frac{\phi_p}{N v_p} \int D\boldsymbol{r}_j \; P[\boldsymbol{r}_j] \Big(\ln P[\boldsymbol{r}_j] + \beta E([\boldsymbol{r}_j]; 0, 1) \Big) \\
+ \sum_{i=\{H_2O, Na^+, Cl^-, H^+, OH^-\}} \int d\boldsymbol{r} \; \rho_i(\boldsymbol{r}) \Big(\ln \rho_i(\boldsymbol{r}) v_{H_2O} - 1 + \beta \mu_i^o \Big) \\
+ \int d\boldsymbol{r} \; \beta \Big[\langle \rho_q(\boldsymbol{r}) \rangle \psi(\boldsymbol{r}) - \frac{1}{2} \epsilon_o \epsilon(\boldsymbol{r}) \Big(\nabla \psi(\boldsymbol{r}) \Big)^2 \Big] \\
+ \sum_{i=\{p,\, tr\}} \int d\boldsymbol{r} \; \langle \rho_i(\boldsymbol{r}) \rangle \Big[f_i(\boldsymbol{r}) \Big(\ln f_i(\boldsymbol{r}) + \beta \mu_{i,c}^o \Big) \\
+ \Big(1 - f_i(\boldsymbol{r}) \Big) \Big(\ln(1 - f_i(\boldsymbol{r})) + \beta \mu_{i,o}^o \Big) \Big] \qquad (3.11) \\
- \sum_{i=\{Na^+, Cl^-, OH^-, tr\}} \int d\boldsymbol{r} \; \beta \mu_i \rho_i(\boldsymbol{r}) \\
- \int d\boldsymbol{r} \; \beta \mu_{H^+} \Big(\rho_{H^+}(\boldsymbol{r}) + f_{H^+,\, tr} \rho_{tr}(\boldsymbol{r}) + f_{H^+,\, p} \langle \rho_p(\boldsymbol{r}) \rangle \Big) \\
+ \int d\boldsymbol{r} \; \beta \pi(\boldsymbol{r}) \Big[\langle \phi_p(\boldsymbol{r}) \rangle + \sum_{i=\{H_2O, Na^+, Cl^-, H^+, OH^-, tr\}} \phi_i(\boldsymbol{r}) - 1 \Big]
\end{aligned}
$$

The first term contributing to the free energy accounts for the configurational entropy associated with the PAA molecules. Here, ϕ_p is the total volume fraction of PAA (indicated herein with the subscript p), N the total number of statistical segments in a single chain and v_p the volume of a statistical monomer. The precise manner in which statistical segments have been determined for PAA will be elaborated upon later in this work. A path integral is performed over all space curves $\boldsymbol{r}_j$, where j indicates an arbitrary PAA molecule, represented by $\int D\boldsymbol{r}_j$. Here, we have tacitly assumed that the ensemble average configurational entropy and internal energy of all unique PAA molecules are identical.

Accordingly, the internal energy for a fragment of a space curve $\boldsymbol{r}_j$ of a continuous Gaussian chain extending along the contour (parameterized by s) from s_1 to s_2 is given by:

$$\beta E([\boldsymbol{r}_j]; s_1, s_2) = \int_{s_1}^{s_2} ds \ \frac{3}{2a^2 N} \left| \frac{d\boldsymbol{r}_j}{ds} \right|^2 \tag{3.12}$$

Where the unsubscripted a represents the statistical segment length. Note that the parameter s has been non-dimensionalized such that $s = 1$ at that full polymer contour length. The total internal energy of PAA molecule j is given by the second term in Equation (3.11).

The remaining terms in Equation 3.11 are identical to those in Equation 3.4 excepting the more general spatial dependence of variables on $\boldsymbol{r}$ rather than r. However, the use of the continuous Gaussian chain model necessitates a redefinition of the ensemble average volume fraction as:

$$\langle \phi_p(\boldsymbol{r}) \rangle = \int D\boldsymbol{r}_j \ P[\boldsymbol{r}_j] \ \int_0^1 ds \ \delta\Big(\boldsymbol{r} - \boldsymbol{r}_j(s)\Big) \tag{3.13}$$

Where $\delta()$ is the Dirac delta function. The ensemble average density of PAA is related to the volume fraction through $\langle \rho_p(\boldsymbol{r}) \rangle v_p = \langle \phi_p(\boldsymbol{r}) \rangle$.

Equilibrium expressions obtained upon functional minimization of Equation (3.11) with respect to the relevant physical variables results in the same expressions shown in Equations 3.7 through 3.9.

Functional minimization of the generalized free energy expression with respect to the probability of a space curve for an arbitrary molecule, $P[\boldsymbol{r}_j]$, is slightly more involved than the other variables discussed so far. Before we elucidate this probability expression, we define a field $w(\boldsymbol{r})$:

$$w(\boldsymbol{r}) = \beta\pi(\boldsymbol{r})v_p + \frac{v_p}{v_{mon}}\ln\Big(1 - f_i(\boldsymbol{r})\Big) - \frac{v_p}{2}\beta\epsilon_o(\epsilon_p - \epsilon_{H_2O})\Big(\nabla\psi(\boldsymbol{r})\Big)^2 \tag{3.14}$$

This variable $w(\boldsymbol{r})$ should be interpreted as the self consistent external field acting on an arbitrary single polymer chain. It now allows us to define the probability obtained upon functional minimization in the following manner:

$$P[\boldsymbol{r}_j] = \frac{1}{Q[w]}\exp\Big[-N\int_0^1 ds\,\Big(\frac{3}{2a^2N}\Big|\frac{d\boldsymbol{r}_\alpha}{ds}\Big|^2 + w(\boldsymbol{r}_\alpha)\Big)\Big] \tag{3.15}$$

Where we have introduced the full single chain partition function $Q[w]$ which has an explicit functional dependence on the external field. We now introduce the two complementary partial partition functions, $q(\boldsymbol{r}, s)$ and $q^\dagger(\boldsymbol{r}, s)$, which quantify the statistical weight for the presence of a Gaussian chain at $\boldsymbol{r}$, for s along the contour and acted upon by the field $w(\boldsymbol{r})$. These two partition functions are distinguished by the direction along the contour in which they propagate. Note that the functional dependence of these functions on the external field $w(\boldsymbol{r})$ is implied and not explicitly noted in the remainder of this analysis. These new partition functions allow for a convenient definition of the full single chain partition function:

$$Q[w] = \int d\boldsymbol{r}\; q(\boldsymbol{r}, s)q^\dagger(\boldsymbol{r}, s) \tag{3.16}$$

which retains a constant value for all values of the contour parameter within the domain 0 to 1. Additionally, the partial partition functions allow for a more practical definition of the ensemble average volume fraction of polymer:

$$\langle \phi_p(\boldsymbol{r}) \rangle = \frac{\phi_p}{Q[w]} \int_0^1 ds \; q(\boldsymbol{r}, s) q^\dagger(\boldsymbol{r}, s) \tag{3.17}$$

Furthermore, a Taylor series expansion to second order in space and first order along the polymer's contour for the definition of the partial partition functions implies their satisfaction of the following equations:

$$\begin{aligned} \frac{\partial q(\boldsymbol{r}, s)}{\partial s} &= \left[\frac{a^2 N}{6} \nabla^2 - w(\boldsymbol{r}) \right] q(\boldsymbol{r}, s) \\ \frac{\partial q^\dagger(\boldsymbol{r}, s)}{\partial s} &= - \left[\frac{a^2 N}{6} \nabla^2 - w(\boldsymbol{r}) \right] q^\dagger(\boldsymbol{r}, s) \end{aligned} \tag{3.18}$$

The complementary partial partition function is identical to Equation (3.18) except for the right hand-side being multiplied by -1. A more thorough description of the derivation of this partial differential equation (PDE) is enlightening though, unfortunately, beyond the scope of this work. Interested readers are referred to the helpful review by Matsen upon which our specific implementation has been largely been inspired.[92]

We have now derived a mathematical framework capable of fully describing the equilibrium thermodynamics of PAA end-grafted to a surface in a solution of sodium, chloride, tris, water and the aqueous ions hydronium and hydroxide. In order to solve these equations, we must make specific several points that have been left general as of yet. In particular, we make use of a spherical coordinate system and enforce spherical symmetry. We define the surface of the NP to be at the radial coordinate R and the far-field boundary to be at $R + L$. We then use a non-dimensionalized radial coordinate, $\bar{r}$, which is equal to $\kappa \equiv R/(R+L)$ at the AuNP's surface and 1 at the far-field boundary. Next, space is discretized in this radial coordinate. Together,

the incompressibility constraint and Poisson equation constitute a system of coupled, non-linear equations for which the unknown variables are the Lagrange multipliers $\pi(\overline{r})$ and the electrostatic potential $\psi(\overline{r})$ at every discrete position in $\overline{r}$. For the electrostatic potential in the Poisson equation, we specify a homogeneous Neumann boundary condition at $\overline{r} = \kappa$ and a homogeneous Dirichlet condition at $\overline{r} = 1$. This system of equations designedly has zero degrees of freedom however, solution of these equations requires the finding of a solution to the PDEs in Equation (3.18).

We begin the solution of the first equation in Equation (3.18) by expanding the spatial dependence of the partial partition function in Fourier series: $q(r, s) = \sum_i q_i(s)\Phi_i(\overline{r})$. We shall present a solution method exclusively for $q(\overline{r}, s)$ but note that an identical method is used for $q^\dagger(\overline{r}, s)$ when appropriate boundary conditions are substituted. Next, we extract from the Fourier series representation of the Laplacian term from Equation (3.18) the following eigenvalue problem for spherical coordinates:

$$\frac{1}{\overline{r}^2}\frac{d}{d\overline{r}}\left(\overline{r}^2\frac{d\Phi_i(\overline{r})}{d\overline{r}}\right) = -\lambda_i^2\Phi_i(\overline{r}) \tag{3.19}$$

We then impose the following boundary conditions in the radial coordinate on the eigenfunctions $\Phi_i(\overline{r})$:

$$\begin{aligned}\Phi_i(\overline{r} = \kappa) &= 0\\ \frac{d\Phi_i(\overline{r} = 1)}{d\overline{r}} &= 0\end{aligned} \tag{3.20}$$

These boundary conditions assert that there is no polymer precisely at the surface R and that the derivative the polymer volume fraction with respect to the radial coordinate is equal to 0 at the far-field boundary. A survey of Equation 3.18 and the

definition of the Fourier series expansion makes clear why this assertion follows from the boundary condition specification of the eigenfunctions in Equation 3.20.

Following the imposition of the boundary conditions, the orthonormal eigenfunctions are now specifiable as:

$$\Phi_i(\overline{r}) = 2\sqrt{\frac{\lambda_i}{2\lambda_i(1-\kappa) - \sin(2\lambda_i(1-\kappa))}}\ \frac{\sin(\lambda_i(1-\overline{r}))}{\overline{r}} \tag{3.21}$$

The eigenvalues of which are specified by the following characteristic equation:

$$\tan(\lambda_i(1-\kappa)) = \lambda_i \tag{3.22}$$

Which does not possess a closed form analytical solution and is consequently solved numerically. By expanding the second order PDEs in Equation (3.18) in Fourier series and exploiting the orthonormal property of the eigenfunctions we can express them as first order ordinary differential equations (ODEs):

$$\begin{aligned} \frac{d}{ds}q_i(s) &= \sum_j A_{ij}q_j(s) \\ \frac{d}{ds}q_i^{\dagger}(s) &= -\sum_j A_{ij}q_j(s) \\ A_{ij} &= -\frac{\lambda_i^2 a^2 N}{6(R+L)^2}\delta_{ij} - \sum_j w_k \int_{\kappa}^{1} d\overline{r}\ \overline{r}^2 \prod_{n=i,j,k} \Phi_n(\overline{r}) \end{aligned} \tag{3.23}$$

Where δ_{ij} is the Kronecker delta and w_k is the k^{th} spectral coefficient of the Fourier series expansion for the external field.

We now impose boundary conditions for each of the two complementary partial partition functions:

$$
\begin{aligned}
q(\overline{r}, s=0) &= \tanh(\zeta(\overline{r}-\kappa)) \\
q^{\dagger}(\overline{r}, s=1) &= \frac{1}{\sqrt{2\pi\sigma_g^2}} \exp\left(\frac{-(\overline{r}-\kappa-\epsilon_g)}{\sigma_g}\right)^2 \tanh(\zeta(\overline{r}-\kappa))
\end{aligned}
\tag{3.24}
$$

These boundary conditions deviate quite substantially from those that are typically used in the literature for important reasons that will be elaborated upon later with a discussion of implementation. The first boundary condition, that for $q(\overline{r}, s=0)$, specifies that the $s=0$ polymer end has a practically equal propensity to occupy any part of space except near the surface. This end of the polymer shall be referred to as the free end. The extent of the depletion of the propensity of the free end to be near the surface is governed by the parameter ζ and the incorporation of a hyperbolic tangent function. This function ensures that the volume fraction of polymer be 0 at $\overline{r}=\kappa$ and asymptotically approach 1 away from the surface. The same hyperbolic tangent is multiplied by the boundary condition for $q^{\dagger}(\overline{r}, s=1)$. This boundary condition for $s=1$ specifies that the grafted end be localized to a Gaussian distribution the standard deviation of which is given by σ_g at a distance from the NP surface given by ϵ_g.

Both the depletion of the polymer proximal to the NP surface and the Gaussian distribution of grafted polymer ends a distance from said surface are physically justified by the presence and geometry of the thiol linker molecule. As we are interested in the equilibrium organization of molecular species at length scales smaller than the size of the linker molecular its effect cannot be summarily neglected.

We now use a simple Euler integration method to solve the ODEs in Equation (3.23). The partial partition functions can then be used to determine the ensemble

average volume fraction of polymer using Equation (3.17). This can then be used in the system of equations mentioned previously including incompressibility and the Poisson equation.

The SCFT model outlined herein contains all of the necessary details to calculate the equilibrium properties of polyelectrolyte molecules end-grafted to spherical surfaces. It need only be parameterized using the bulk solution properties and physical characteristics of the system of interest. For this case, we treat PAA end-grafted to spherical NP's and apply all of the necessary physical properties for this system. One final point worth mentioning which is that the statistical segment length a is taken to be the Kuhn length for PAA (0.64 nm) and the number of statistical segments N is taken as the total contour length of the PAA molecule being treated divided by a.[93] This Kuhn length has been experimentally measured and its use is intentional as it is related to what has been referred to as the intrinsic persistence length. The intrinsic persistence length is the total persistence length of a polyelectrolyte at 0% ionization.[94] The persistence length is one half of the Kuhn length.

Implementation Challenges for the Gaussian Chain Model

Implementation of the SCFT incorporating the Gaussian chain model in the manner described in the previous section has so far been frought with obstacles. Namely, for many of the physical parameters of the NP samples and bulk conditions, an oscillatory behavior has presented itself. Oscillations of all variables between consecutive discrete layers arise to a greater extent as the grafting density is increased, the NaCl concentration is decreased or when the diameter of the NPs is increased. All of these shifts in the values of the physical parameters are consistent with the imposition of more strain on the configurational ensemble. This could also be stated as shifting the variables in this way correlates with the PAA equilibrium behavior being dictated more by the external field w. Interestingly, the system of equations is able to converge

on a solution that features these oscillations; they are not just apparent during the solving process. As the variables are shifted such that they induce a stronger external field, these oscillations appear to increase to a point where convergence is no longer achievable. Based on past observations of this effect, a failure to converge never arises without the emergence of oscillatory behavior preceding it.

There are several explanations for the emergence of this oscillatory behavior and they shall be discussed in order of descending perceived likelihood. First, the subroutine that is iteratively executed as part of the KINSOL solver requires the calculation of the integral presented in Equation 3.25 in order to resolve the spectral coefficients of the external field.

$$w_i = \int_{\kappa}^{1} d\bar{r}\ \bar{r}^2 \Phi_i(\bar{r}) w(\bar{r}) \tag{3.25}$$

Due to the fact that the external field is sampled discretely as dictated by the discretization of real space, there is an intrinsic inaccuracy for this calculation. So far, this integral has been evaluated using the well known trapezoid rule with a spatial discretization of 0.1 nm. We hypothesize that it could be that a feedback mechanism occurs in which the inaccuracy of this numerical integration becomes amplified over successive iterations of the solver routine. This would essentially amount to the solution of the equations needing to possess the same numerical inaccuracy in order to converge. If this is the case, incorporating a finer spatial resolution at targeted regions in space may assuage the issue. Furthermore, there exist more accurate numerical integration formulae such as Gaussian quadrature which could also eliminate the oscillatory behavior.[95]

A second potential source of the oscillatory behavior may be in the manner in which the Laplace operator in the Poisson equation is numerically approximated.

Admittedly, this issue seems less likely to be the source of the oscillatory behavior than that of inaccuracies in numerical integration due to the fact that it has never produced this behavior using the RIS model to our knowledge. Furthermore, convergence of the SCFT equations utilizing the continuous Gaussian chain model has been obtained for some configurations of physical parameters (NP sample 5 and 150 mM NaCl) without displaying any oscillations. This indicates that the integration of electrostatics within the framework does not always effect oscillatory behavior. However, it is true that these oscillations are completely absent when the Gaussian chain SCFT equations are solved without the incorporation of electrostatics. In fact, the solver routine converged on solutions without hesitation for all NP sample conditions when electrostatics was excluded. At this point, whether the incorporation of electrostatics is directly causative of the oscillations or merely correlative is unclear. It is possible that the incorporation of electrostatics merely increases the strength of the external field to the point that the solver routine becomes unstable. If this is true, it could indicate that there is nothing that inherently causes oscillations due to electrostatics but that any physical phenomenon that increases the strength of the external field to a certain point will have this effect. This hypothesis could be probed by utilizing a more accurate numerical approximation for the Laplace operator and then excluding electrostatics and increasing the strength of the external field via some simple repulsion between polymer molecules and observing the effect on oscillations.

A final and decidedly more distant explanation for the observed oscillatory behavior is that our implementation of the SCFT equations is flawless and physically justified and that the difficulty that it has had solving for some of the NP configurations indicates that our parameters for them are inaccurate. Basically this argument claims that our theory and its numerical solution are correct and that if it cannot solve for a certain set of parameters, then those parameters are unphysical. This could be valid if our assumption that the measured PAA grafting density is constant

for all NP diameters and PAA lengths is wildly inaccurate. Again, this explanation is unlikely to be the case; however, the veracity of this claim could be tested using TGA to measure the grafting density for every individual sample. Due to our lack of faith in this explanation and the cost of performing TGA with the available facilities, we recommend that this explanation only be seriously entertained when the previous two have been eliminated as possibilities.

It should be noted that solvated Gaussian chain polymers end-tethered to spherical NP surfaces have been successfully modeled before with a SCFT by Kim and Matsen.[96] However, there are important distinctions in the manner in which their SCFT equations were implemented compared to our realization. Specifically, the authors did not expand the spatial dependence of the partial partition function and rather opted to use a numerical algorithm to solve the PDEs in Equation 3.18 rather than the ODEs in Fourier space.[97] Depending on the specifics of the problem, attacking the SCFT equations in the manner that we have outlined can be more efficient.[92]

It should be emphasized that we are unaware of any other attempt to apply the Gaussian chain model to a physical system with the specific characteristics that have been tested experimentally in our study. The physical system includes a solvated polyacid end-tethered to a spherical NP surface exposed to ions and buffer molecules. Such a system requires an accurate treatment of electrostatics and some accounting for the chemical equilibrium sites present on the chain molecule. Due to the absence of any directly comparable treatments in the literature, what has been reported provides us with insightful techniques to attempt but is a far cry from any formal prescription for how to approach this problem.

As has been mentioned, convergence of the SCFT equations that utilize the Gaussian chain model was obtained with an absence of oscillations for certain NP samples. Figure 3.17 shows the volume fractions of PAA, water, $mathrmNa^+$ and tris as a function of distance from the NP surface for NP sample number 5 and at 150 mM

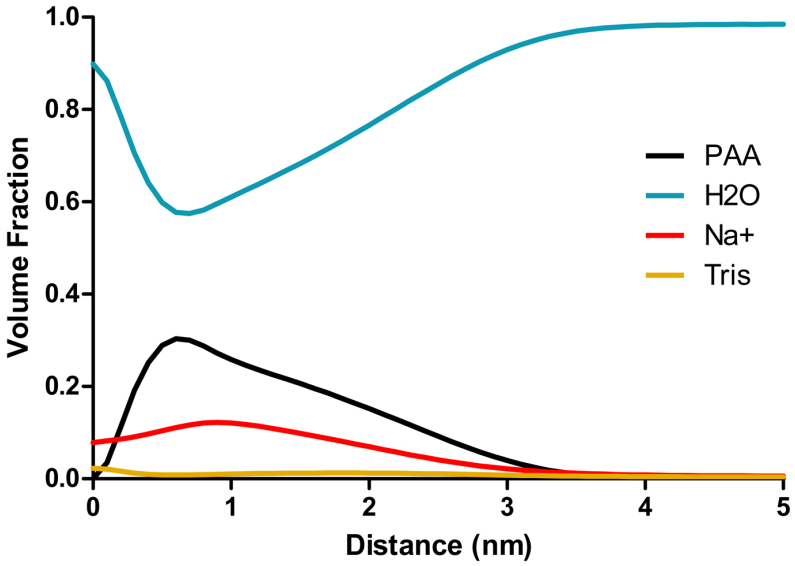

Figure 3.17: Volume fractions of molecular species as a function of distance from the NP surface calculated using the continuous Gaussian chain model for a NP with a diameter of 14.5 nm, a degree of polymerization of PAA of 11 and a PAA grafting density of 0.58 nm^{-2}. This plot has been calculated for a bulk pH of 8.0, a temperature of 25 °C and a bulk concenctration of 150 mM NaCl.

NaCl.

The equilibrium pH as a function of distance from the NP surface has also been calculated for these conditions and plotted in Figure 3.18.

The plots of the equilibrium properties as a function of distance from the NP surface shown in Figures 3.17 and 3.18 are very similar in character to those calculated using the RIS model, Figures 3.15 and 3.16. It is apparent that the same physical mechanisms are manifest in both systems. There are some subtle differences between the two curves. Most notably, the PAA molecules are more stretched out in the Gaussian model. This likely has two distinct causes. First, there may be an issue with the RIS model not adequately sampling the most stretched out configurations, making the predicted PAA configurational ensemble slightly more compact than would be the case with a perfectly sampled configuration space. Secondly, the Gaussian chain model does predict that the there will be a non-zero volume fraction of PAA at all

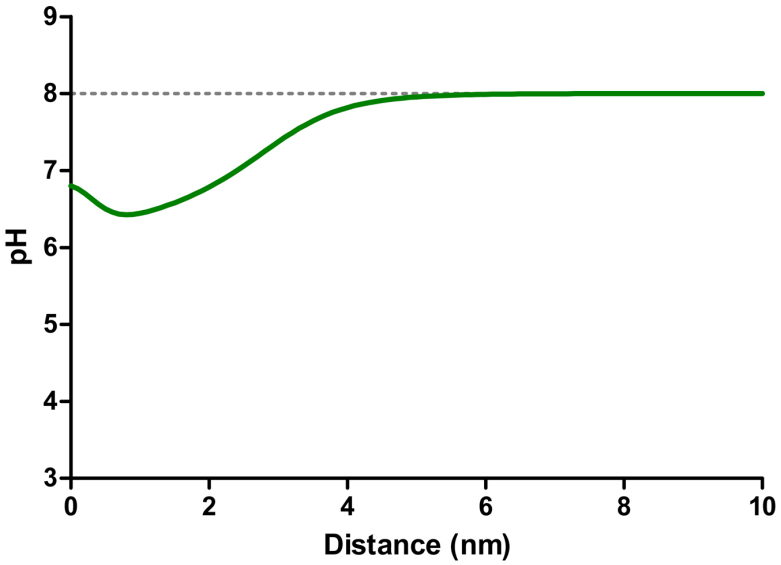

Figure 3.18: pH as a function of distance from the NP surface calculated using the continuous Gaussian chain model. The pH function was calculated for a bulk pH of 8.0 (indicated by a dotted line), a temperature of 25 °C and a bulk concentration of 150 mM NaCl.

distances. The total contour length of the space curves of the Gaussian model can be infinitely long: though the probability of this being the case is infinitesimal, it is not zero. Therefore, we can expect that the Gaussian model may slightly overpredict the extent to which the PAA ensemble may extend from the surface as it is unconstrained by the physical contour length of the polymer and the external field that we are imposing functions to emphasize extended chains.

3.5 Reflections on the Methodology and Future Work

Future work on this project will undoubtedly include an effort to resolve the implementation issues that have emerged for the SCFT employing the continuous Gaussian chain model. Preliminary solutions of the model have shown that it provides similar thermodynamic information relative to the RIS model. However, the oscillatory behavior that has been observed constitutes an obstacle to the exploitation of the theoretical advantage of using the Gaussian chain model: that it can be used to ac-

curately model polymers of arbitrary length. Once these issues are resolved a whole host of information will be accessible regarding the molecular organization of the PAA and local solution effects. This information could then be correlated across the CCD design space to look for correlations with the observed influence on Aβ lag time.

With the theoretical model functional across design space, we could then attempt to optimize the Aβ lag extension factor by experimentally probing the parts of design space predicted to be optimal by our regression model.

Chapter 4

Conclusions and Future Work

In Chapter 2, the development of a statistical thermodynamic model for interactions of Aβ monomers was outlined. This model is unique from those existing in the literature in that it directly addresses the gargantuan multiplicity of Aβ configurations that are significant to these interactions in the language of statistical mechanics. This theoretical apparatus was applied to the Aβ dimerization process for several relevant conditions, identifying key free energy contributions and yielding results that align qualitatively with Aβ aggregation. This theory is capable of quantifying thermodynamic parameters of Aβ interactions that cannot be measured experimentally. Moreover, these thermodynamic relationships facilitate a rich description of the molecular organization and physics that guide these interactions.

Chapter 3 explained how PAA-functionalized NPs were synthesized and characterized with an assortment of diameters and degrees of polymerization of PAA constituting a CCD. Aβ aggregation experiments with these NPs indicate that these physical parameters of the NPs have a significant effect Aβ aggregation and that these effects are a function of bulk NaCl concentration. This study is especially interesting in light of the fact that the most likely explanation for the observed effects on Aβ interactions is through a local modulation of the solutions properties which is the exact phenomenology studied with Aβ statistical thermodynamic model. A similar statical thermodynamic model was developed that treated the end-tethered PAA as the chain molecule of interest rather than Aβ. The resulting SCFT was derived with two distinct chain models, the RIS model and the continuous Gaussian chain model.

Both are capable of making quantitative the manner in which the system mitigates the energetically unfavorable localized negative charge on the PAA. However, challenges have thus far beset the implementation of the Gaussian chain model which have restricted the unlocking of its full potential to model the entire design space.

The work that has been presented here constitutes the beginnings of a powerful platform to engineer molecular systems that can modulate Aβ aggregation. The major components of this platform and their interdependencies are depicted in Figure 4.1. This platform consists of two experimental components: NP synthesis/characterization and Aβ aggregation experiments. These two components inform one another in the sense that the synthesized NPs are tested for their effects on aggregation and these results can be used to determine what NPs should be synthesized to optimize desired effects. The theoretical components of the platform are dependent on the results of the experimental components. The NP model can be parameterized with the physical properties of the experimentally characterized NPs while the Aβ model is compared directly to the experimentally determined effect on the macroscopic aggregation process.

The interdependencies between all other components of the platform and the Aβ model have been rendered gray to indicate that these operative relationships have yet to be realized in practice. The reason that these connections have not been realized on the experimental front is due to the scale of the Aβ interactions that can presently be modeled relative to that which can be probed experimentally. Theoretically, there is no obstacle to performing the same types of calculations that have been implemented for the PMF for interacting Aβ molecules with a polyacid-functionalized NP proximal to their respective centers' of mass throughout the process. This analysis could be performed quite easily if one assumed as a first approximation that the effect of the ABeta molecules on the NPs is negligible and calculated only the effect of the NPs on the ABeta interaction. This assumption would be quite reasonable as

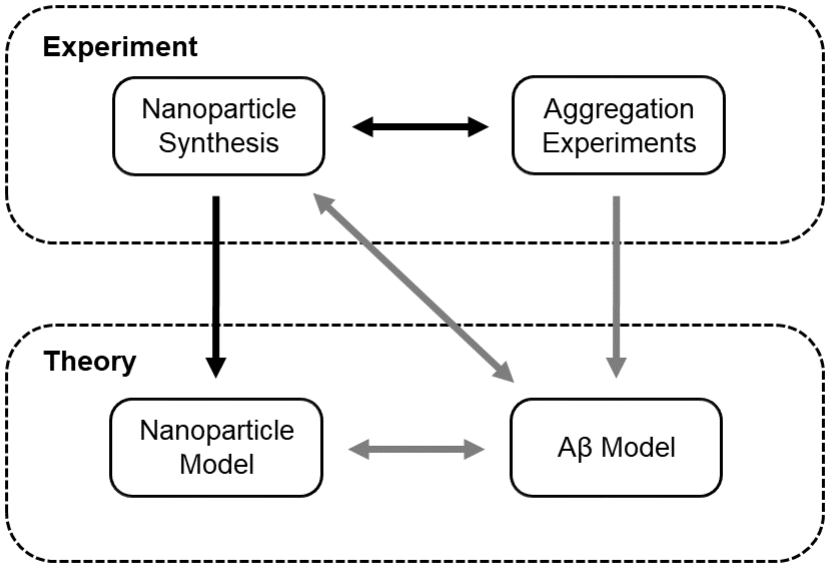

Figure 4.1: Schematic of interplay between components of Aβ aggregation modulation design platform.

the relevant length scales and solution influence are sufficiently disparate.

However, what can be determined experimentally with the described methods is the formation of β-sheet structures possessing affinity for thioflavin-T. The method that we have used for detection of such structures is far too insensitive to detect the formation of dimers regardless of the fact that the extent to which β-sheet structures exist in oligomers in general is debatable. Thus in order to connect the Aβ model to the results of Aβ aggregation, the theory would have to be extended to predictions of much larger structures and ultimately to the treatment of fibrils. Of course, one could simply use the predictions made by the Aβ model as implemented solely for dimerization under different solution conditions to infer what changes should be made to the NPs' physical properties. Though Aβ dimerization is not an accurate surrogate for the intricacies of higher order Aβ interactions, this simpler process may continue to coincide with the macroscopic trends of the overall aggregation process as has been

explained in Chapter 2.

As of now, the groundwork has been laid for a powerful platform with which to design Aβ aggregation inhibitors. A model of Aβ interactions that can accurately predict the thermodynamics of Aβ interactions is now functional. For the first time, a methodical, mechanistic study has been undertaken to uncover the as of yet unclear relationships between functionalized NP properties and their effects on amyloid processes. Continued exercise of the platform will slowly refine our mechanistic understanding and move us closer toward realizing its full potential to engineer therapeutics.

Bibliography

[1] Kenneth D. Kochanek et al. "Mortality in the United States, 2013". In: *NCHS Data Brief; No. 178* 178 (2014), p. 7.

[2] World Health Organization. *International statistical classification of diseases and related health problems*. World Health Organization, 2004.

[3] L. E. Hebert et al. "Alzheimer disease in the United States (2010-2050) estimated using the 2010 census". In: *Neurology* 80.19 (2013), pp. 1778–1783.

[4] Alzheimer Alois. "Über eine eigenartige Erkrankung der Hirnrinde [About a peculiar disease of the cerebral cortex]". In: *Allgemeine Zeitschrift fur Psychiatrie und Psychisch-Gerichtlich Medizin* 64.1-2 (1907), pp. 146–148.

[5] Alzheimer Association. "2017 Alzheimer's disease facts and figures". In: *Alzheimer's & Dementia* 13.4 (2017), pp. 325–373.

[6] John a Hardy and Gerald a Higgins. "Disease : Alzheimer's Cascade Hypothesis Amyloid". In: *Science* 256.5054 (1992), pp. 184–185.

[7] Dennis J Selkoe and John Hardy. "The amyloid hypothesis of Alzheimer's disease at 25 years". In: *EMBO Molecular Medicine* 8.6 (2016), pp. 595–608.

[8] Iryna Benilova, Eric Karran, and Bart De Strooper. "The toxic Aβ oligomer and Alzheimer's disease: an emperor in need of clothes". In: *Nature Neuroscience* 15.3 (2012), pp. 349–357.

[9] Joseph M. Castellano et al. "Human apoE isoforms differentially regulate brain amyloid-β peptide clearance". In: *Science translational medicine* 3.89 (2011), 89ra57.

[10] Peter Hortschansky et al. “The aggregation kinetics of Alzheimer’s β-amyloid peptide is controlled by stochastic nucleation”. In: *Protein Science* 14.7 (2005), pp. 1753–1759.

[11] Rakez Kayed and Cristian A. Lasagna-Reeves. “Molecular Mechanisms of Amyloid Oligomers Toxicity”. In: *Journal of Alzheimer’s Disease* 33 (2012), pp. 67–78.

[12] Luitgard Nagel-Steger, Michael C. Owen, and Birgit Strodel. “An Account of Amyloid Oligomers: Facts and Figures Obtained from Experiments and Simulations”. In: *ChemBioChem* 17.8 (2016), pp. 657–676.

[13] Jessica Nasica-Labouze et al. “Amyloid β Protein and Alzheimer’s Disease: When Computer Simulations Complement Experimental Studies”. In: *Chemical Reviews* 115.9 (2015), pp. 3518–3563.

[14] Leonid Breydo and Vladimir N Uversky. “Structural, morphological, and functional diversity of amyloid oligomers”. In: *FEBS Letters* 589.19 (2015), pp. 2640–2648.

[15] Yuliang Zhang et al. “Self-assembly of the full-length amyloid Aβ42 protein in dimers”. In: *Nanoscale* 8.45 (2016), pp. 18928–18937.

[16] Payel Das, Anita R. Chacko, and Georges Belfort. “Alzheimer’s Protective Cross-Interaction between Wild-Type and A2T Variants Alters Aβ42 Dimer Structure”. In: *ACS Chemical Neuroscience* 8.3 (2016), pp. 606–618.

[17] Viet Hoang Man, Phuong Hoang Nguyen, and Philippe Derreumaux. “High-Resolution Structures of the Amyloid-β 1-42 Dimers from the Comparison of Four Atomistic Force Fields”. In: *The Journal of Physical Chemistry B* (2017).

[18] Song Ho Chong and Sihyun Ham. “Distinct Role of Hydration Water in Protein Misfolding and Aggregation Revealed by Fluctuating Thermodynamics Analysis”. In: *Accounts of chemical research* 48.4 (2015), pp. 956–965.

[19] Wilfred F van Gunsteren and Herman J C Berendsen. “Computer Simulation of Molecular Dynamics: Methodology, Applications, and Perspectives in Chemistry”. In: *Anger,. Chem. lnr. Ed. Engl* 29.Md (1990), pp. 992–1023.

[20] Martin Karplus. “Molecular dynamics simulations of biomolecules”. In: *Accounts of Chemical Research* 35.6 (2002), pp. 321–323.

[21] Donald W. Brenner. “Empirical potential for hydrocarbons for use in simulating the chemical vapor deposition of diamond films”. In: *Physical Review B* 42.15 (1990), pp. 9458–9471.

[22] Jacob D Durrant and J Andrew McCammon. “Molecular dynamics simulations and drug discovery”. In: *BMC biology* 9.71 (2011), pp. 1–9.

[23] David A. Case et al. “The Amber biomolecular simulation programs”. In: *Journal of Computational Chemistry* 26.16 (2005), pp. 1668–1688.

[24] Yassmine Chebaro, Samuela Pasquali, and Philippe Derreumaux. “The coarse-grained OPEP force field for non-amyloid and amyloid proteins”. In: *Journal of Physical Chemistry B* 116.30 (2012), pp. 8741–8752.

[25] Jing Huang and Alexander D MacKerell Jr. “CHARMM36 all-atom additive protein force field: Validation based on comparison to NMR data”. In: *Journal of Computational Chemistry* 34.25 (2013), pp. 2135–2145.

[26] Berk Hess et al. “GROMACS 4: Algorithms for Highly Efficient, Load-Balanced, and Scalable Molecular Simulation”. In: *Journal of Chemical Theory and Computation* 4.3 (2008), pp. 435–447.

[27] Benjamin M. Good and Andrew I. Su. “Games with a scientific purpose”. In: *Genome Biology* 12.12 (2011), pp. 2010–2012.

[28] Vickie Curtis. “Motivation to Participate in an Online Citizen Science Game: A Study of Foldit”. In: *Science Communication* 37.6 (2015), pp. 723–746.

[29] Christopher B Eiben et al. “Increased Diels-Alderase Activity through Foldit Player Guided Backbone Remodeling”. In: *Nature biotechnology* 30.2 (2012), pp. 1–5.

[30] Rikkert Nap, Peng Gong, and Igal Szleifer. “Weak Polyelectrolytes Tethered to Surfaces : Effect of Geometry, Acid-Base Equilibrium and Electrical”. In: *Journal of Polymer Science: Part B: Polymer Physics* 44.18 (2006), pp. 2638–2662.

[31] Mario Tagliazucchi, Mónica Olvera de la Cruz, and Igal Szleifer. “Self-organization of grafted polyelectrolyte layers via the coupling of chemical equilibrium and physical interactions”. In: *Proceedings of the National Academy of Sciences* 107.12 (2010), pp. 5300–5305.

[32] Peng Gong et al. “Behavior of Surface-Anchored Poly(acrylic acid) Brushes with Grafting Density Gradients on Solid Substrates: 2. Theory”. In: *Macromolecules* 40.24 (2007), pp. 8765–8773.

[33] Dawei Wang et al. “How and Why Nanoparticle’s Curvature Regulates the Apparent pKa of the Coating Ligands.” In: *Journal of the American Chemical Society* 133.7 (Feb. 2011), pp. 2192–7.

[34] Joseph T. Jarrett, Elizabeth P. Berger, and Peter T. Lansbury Jr. “The Carboxy Terminus of the β Amyloid Protein Is Critical for the Seeding of Amyloid Formation: Implications for the Pathogenesis of Alzheimer’s Disease”. In: *Biochemistry* 32.18 (1993), pp. 4693–4697.

[35] William L. Jorgensen et al. “Comparison of simple potential functions for simulating liquid water”. In: *The Journal of Chemical Physics* 79.2 (1983), pp. 926–935.

[36] Nikolaos G. Sgourakis et al. “Atomic-Level Characterization of the Ensemble of the Aβ(1-42) Monomer in Water Using Unbiased Molecular Dynamics

Simulations and Spectral Algorithms". In: *Journal of Molecular Biology* 405.2 (2011), pp. 570–583.

[37] Thorsten Lührs et al. "3D structure of Alzheimer's amyloid-β(1-42) fibrils". In: *Proceedings of the National Academy of Sciences* 102.48 (2005), pp. 17342–17347.

[38] David Chandler. *Introduction to Modern Statistical Mechanics*. New York, New York: Oxford University Press, 1987.

[39] Doree Sitkoff, Kim A. Sharp, and Barry Honig. "Accurate Calculation of Hydration Free Energies Using Macroscopic Solvent Models". In: *The Journal of Physical Chemistry* 98.7 (1994), pp. 1978–1988.

[40] Frank Eisenhaber et al. "The Double Cubic Lattice Method: Efficient Approaches to Numerical Integration of Surface Area and Volume and to Dot Surface Contouring of Molecular Assemblies". In: *Journal of Computational Chemistry* 16.3 (1995), pp. 273–284.

[41] Irina Massova and Peter A. Kollman. "Combined molecular mechanical and continuum solvent approach (MM-PBSA/GBSA) to predict ligand binding". In: *Perspectives in Drug Discovery and Design* 18.1 (2000), pp. 113–135.

[42] E. Raphael and Jean-Francois Joanny. "Annealed and Quenched Polyelectrolytes". In: *Europhysics Letters* 13.7 (1990), pp. 623–628.

[43] Mark J. Uline, Shihong Meng, and Igal Szleifer. "Surfactant driven surface anchoring transitions in liquid crystal thin films". In: *Soft Matter* 6.21 (2010), pp. 5482–5490.

[44] Howard Ted Davis. *Statistical Mechanics of Phases, Interfaces, and Thin Films*. New York, New York: Wiley-VCH, 1996.

[45] Andrew Zangwill. *Modern Electrodynamics*. Cambridge, UK: Cambridge University Press, 2013.

[46] Ralph H. Colby and Michael Rubinstein. *Polymer Physics*. New-York: Oxford University Press, 2003.

[47] R. Scott Rowland and Robin Taylor. "Intermolecular Nonbonded Contact Distances in Organic Crystal Structures: Comparison with Distances Expected from van der Waals Radii". In: *The Journal of Physical Chemistry* 100.18 (1996), pp. 7384–7391.

[48] Alan C. Hindmarsh and Allan G. Taylor. *PVODE and KINSOL: parallel software for differential and nonlinear systems*. Tech. rep. Lawrence Livermore National Lab, CA, 1998.

[49] Donald A. McQuarrie. *Statistical Mechanics*. Mill Valley, California: University Science Books, 2000.

[50] Jacob N. Israelachvili. *Intermolecular and Surface Forces*. 3rd ed. Academic Press, 2011.

[51] Seth W. Snyder et al. "Amyloid-β Aggregation: Selective Inhibition of Aggregation in Mixtures of Amyloid with Different Chain Lengths". In: *Biophysical Journal* 67.3 (1994), pp. 1216–1228.

[52] H LeVine. "Thioflavine T interaction with synthetic Alzheimer's disease β-amyloid peptides: Detection of amyloid aggregation in solution". In: *Protein Science* 2.3 (1993), pp. 404–410.

[53] Raimon Sabaté, Montserrat Gallardo, and Joan Estelrich. "Temperature dependence of the nucleation constant rate in β amyloid fibrillogenesis". In: *International Journal of Biological Macromolecules* 35.1-2 (2005), pp. 9–13.

[54] R. Pouplana and J. M. Campanera. "Energetic contributions of residues to the formation of early amyloid-β oligomers". In: *Phys. Chem. Chem. Phys.* 17 (2015), pp. 2823–2837.

[55] Lev Dykman and Nikolai Khlebtsov. “Gold nanoparticles in biomedical applications: recent advances and perspectives.” In: *Chemical Society reviews* 41.6 (Mar. 2012), pp. 2256–82.

[56] Kelly A Moore et al. “Influence of gold nanoparticle surface chemistry and diameter upon Alzheimer’s disease amyloid-β protein aggregation”. In: *Journal of biological engineering* 11.1 (2017), p. 5.

[57] Alaaldin M Alkilany and Catherine J Murphy. “Toxicity and cellular uptake of gold nanoparticles: what we have learned so far?” In: *Journal of Nanoparticle Research* 12.7 (Sept. 2010), pp. 2313–2333.

[58] Marie-Christine Daniel and Didier Astruc. “Gold Nanoparticles : Assembly, Supramolecular Chemistry, Quantum-Size-Related Properties, and Applications toward Biology, Catalysis, and Nanotechnology”. In: *Chemical Reviews* 104.1 (2004), pp. 293–346.

[59] Leonid Vigderman and Eugene R Zubarev. “Therapeutic platforms based on gold nanoparticles and their covalent conjugates with drug molecules.” In: *Advanced drug delivery reviews* 65.5 (May 2013), pp. 663–76.

[60] S S Shiratori and M F Rubner. “pH-Dependent Thickness Behavior of Sequentially Adsorbed Layers of Weak Polyelectrolytes”. In: (2000), pp. 4213–4219.

[61] Stephan T Dubas and Joseph B Schlenoff. “Swelling and Smoothing of Polyelectrolyte Multilayers by Salt”. In: *Langmuir* 11 (2001), pp. 7725–7727.

[62] Rajesh Sardar et al. “Gold nanoparticles: past, present, and future.” In: *Langmuir : the ACS journal of surfaces and colloids* 25.24 (Dec. 2009), pp. 13840–51.

[63] Marek Grzelczak et al. “Shape Control in Gold Nanoparticle Synthesis”. In: *Chemical Society Review* 37.9 (2008), pp. 1783–1791.

[64] Jordi Llorca et al. “Propene epoxidation over TiO2-supported Au-Cu alloy catalysts prepared from thiol-capped nanoparticles”. In: *Journal of Catalysis* 258.1 (2008), pp. 187–198.

[65] Hsin Tsung Chen et al. “Ethylene epoxidation on a Au nanoparticle versus a Au(111) surface: A DFT study”. In: *Journal of Physical Chemistry Letters* 1.4 (2010), pp. 739–742.

[66] Mingtao Liang et al. “Cellular uptake of densely packed polymer coatings on gold nanoparticles.” In: *ACS nano* 4.1 (2010), pp. 403–413.

[67] Dung The Nguyen et al. “Experimental measurements of gold nanoparticle nucleation and growth by citrate reduction of HAuCl4”. In: *Advanced Powder Technology* 21.2 (2010), pp. 111–118.

[68] John Turkevich, Peter Cooper Stevenson, and James Hillier. “A Study of the Nucleation and Growth Processes in the Synthesis of Colloidal Gold”. In: *Discussions of the Faraday Society* 11 (1951), pp. 55–75.

[69] G Frens. “Controlled Nucleation for the Regulation of the Particle Size in Monodisperse Gold Suspensions”. In: *Nature* 241 (1973), pp. 21–22.

[70] Mathias Brust et al. “Synthesis of Thiol-derivatised Gold Nanoparticles in a Two-phase Liquid-Liquid System”. In: *J. Chem. Soc., Chem. Commun.* (1994), pp. 801–802.

[71] J Kimling et al. “Turkevich Method for Gold Nanoparticle Synthesis Revisited”. In: *J. Phys. Chem. B.* 110.95 mL (2006), pp. 15700–15707.

[72] Maria Wuithschick et al. “Turkevich in New Robes: Key Questions Answered for the Most Common Gold Nanoparticle Synthesis”. In: *ACS Nano* 9.7 (2015), pp. 7052–7071.

[73] Kara Zabetakis et al. “Effect of high gold salt concentrations on the size and polydispersity of gold nanoparticles prepared by an extended Turkevich-Frens method”. In: *Gold Bulletin* 45.4 (2012), pp. 203–211.

[74] Sankar Kalidas Sivaraman, Sanjeev Kumar, and Venugopal Santhanam. “Monodisperse sub-10nm gold nanoparticles by reversing the order of addition in Turkevich method - The role of chloroauric acid”. In: *Journal of Colloid and Interface Science* 361.2 (2011), pp. 543–547.

[75] F Schulz et al. “Little adjustments significantly improve the turkevich synthesis of gold nanoparticles”. In: *Langmuir* 30.35 (2014), pp. 10779–10784.

[76] Nikhil R Jana, Latha Gearheart, and Catherine J Murphy. “Seeding Growth for Size Control of 5 - 40 nm Diameter Gold Nanoparticles”. In: *Langmuir* 37 (2001), pp. 6782–6786.

[77] Christopher Barner-Kowollik. *Handbook of RAFT Polymerization*. 2008, pp. 1–543.

[78] Rajesh Ranjan and William J. Brittain. “Synthesis of high density polymer brushes on nanoparticles by combined RAFT polymerization and click chemistry”. In: *Macromolecular Rapid Communications* 29.12-13 (2008), pp. 1104–1110.

[79] Yu Li, Linda S. Schadler, and Brian C. Benicewicz. *Surface and Particle Modification via the RAFT Process: Approach and Properties*. Vol. 423. 2008, pp. 423–453.

[80] Cyrille Boyer, Martina H. Stenzel, and Thomas P. Davis. “Building nanostructures using RAFT polymerization”. In: *Journal of Polymer Science, Part A: Polymer Chemistry* 49.3 (2011), pp. 551–595.

[81] Brent S. Sumerlin et al. “Modification of gold surfaces with water-soluble (Co)polymers prepared via aqueous reversible addition-fragmentation chain transfer (RAFT) polymerization”. In: *Langmuir* 19.14 (2003), pp. 5559–5562.

[82] Tao Wu et al. “Behavior of surface-anchored poly(acrylic acid) brushes with grafting density gradients on solid substrates: 1. Experiment”. In: *Macromolecules* 40.24 (2007), pp. 8756–8764.

[83] Muriel K Corbierre, Neil S Cameron, and R Bruce Lennox. “Polymer-Stabilized Gold Nanoparticles with High Grafting Densities”. In: *Langmuir* 20 (2004), pp. 2867–2873.

[84] Muriel K Corbierre et al. “Preparation of Thiol-Capped Gold Nanoparticles by Chemical Reduction of Soluble Au (I) - Thiolates”. In: *Chem. Mater.* 17.23 (2005), pp. 5691–5696.

[85] Vitali I. Stsiapura et al. “Thioflavin T as a molecular rotor: Fluorescent properties of thioflavin T in solvents with different viscosity”. In: *Journal of Physical Chemistry B* 112.49 (2008), pp. 15893–15902.

[86] Suzanne K. Shoffner and Santiago Schnell. “Estimation of the lag time in a subsequent monomer addition model for fibril elongation”. In: *Phys. Chem. Chem. Phys.* 18.31 (2016), pp. 21259–21268.

[87] Paul J. Flory. *Statistical Mechanics of Chain Molecules*. Hanser Publishers, 1989.

[88] M. a. Carignano and I. Szleifer. “Statistical thermodynamic theory of grafted polymeric layers”. In: *The Journal of Chemical Physics* 98.1993 (1993), p. 5006.

[89] G Garbès Putzel et al. “Interleaflet coupling and domain registry in phase-separated lipid bilayers.” In: *Biophysical journal* 100.4 (Mar. 2011), pp. 996–1004.

[90] I Szleifer. “Protein Adsorption on Surfaces with Grafted Polymers: A Theoretical Approach”. In: *Biophysical Journal* 72.2 Pt 1 (1997), p. 595.

[91] Glenn Fredrickson. *The Equilibrium Theory of Inhomogeneous Polymers*. Oxford University Press, 2006.

[92] Mark W. Matsen. “Self-Consistent Field Theory and Its Applications”. In: *Soft Matter Vol. 1* 1 (2005), pp. 87–178.

[93] Hongbin Li. “Single-Molecule Force Spectroscopy on Poly(acrylic acid) by AFM”. In: *Langmuir* 15.6 (1999), pp. 2120–2124.

[94] Steven W. Cranford and Markus J. Buehler. “Variation of weak polyelectrolyte persistence length through an electrostatic contour length”. In: *Macromolecules* 45.19 (2012), pp. 8067–8082.

[95] Arthur H Stroud and Don Secrest. “Gaussian quadrature formulas”. In: (1966).

[96] Jaeup U Kim and Mark W Matsen. “Interaction between Polymer-Grafted Particles”. In: (2008), pp. 4435–4443.

[97] J. Crank and P. Nicolson. “A practical method for numerical evaluation of solutions of partial differential equations of the heat-conduction type”. In: *Mathematical Proceedings of the Cambridge Philosophical Society* 43.1 (1947), pp. 50–67.

[98] I Szleifer and M A Carignano. “Tethered Polymer Layers”. In: *Advances in Chemical Physics*. Vol. XCIV. John Wiley & Sons, Inc., 1996, pp. 165–260.

[99] Terrell L. Hill. *An Introduction to Statistical Thermodynamics*. Courier Corporation, 1986, pp. 401–410.

[100] Yu-Shan Lin et al. “Investigating How Peptide Length and a Pathogenic Mutation Modify the Structural Ensemble of Amyloid Beta Monomer”. In: *Biophysical Journal* 102.2 (2012), pp. 315–324.

Appendix A

Additional Analysis of Aβ Model

A.1 Excluded Volume Interactions

To avoid the aforementioned self-excluding intramolecular microstate crosstalk which produces unphysical chain stretching in very dilute conditions, we replace the osmotic pressure in the Boltzmann factor with an excluded volume energy density, $E_j(\mathbf{r})$. The derivation of the excluded volume energy experienced by molecule j begins by writing an incompressibility expression that includes all Aβ molecules except j and a fictitious, space-filling solvent denoted with the subscript s:

$$\langle \phi_{A\beta,\neq j}(\mathbf{r}) \rangle + \exp\Big[-\beta(E_j(\mathbf{r})v_s - \pi_{bulk}v_s) \Big] = 1 \tag{A.1}$$

Writing an incompressibility expression in this way allows for analytical isolation of the excluded volume energy density:

$$\beta E_j(\mathbf{r}) = -\frac{1}{v_s}\ln[1 - \langle \phi_{A\beta,\neq j}(\mathbf{r}) \rangle] + \beta\pi_{bulk} \tag{A.2}$$

This property is not true of the osmotic pressure when multiple mobile species are treated. In the previous expressions, π_{bulk} is the osmotic pressure when $\langle \phi_{A\beta}(\mathbf{r}) \rangle$ and $\psi(\mathbf{r})$ are equal to 0. v_s is the value that minimizes the squared difference of $E_j(\mathbf{r})$ and $\pi(\mathbf{r})$ over all space for an isolated Aβ molecule. Essentially, this procedure amounts to approximating the osmotic pressure that would be present if molecule j were ignored and defining this scalar field as the excluded volume energy density affecting all configurations of molecule j.

The replacement of the osmotic pressure in the Boltzmann factor with the excluded volume interaction energy has the additional consequence of decoupling the probability of a conformation from its effect on the translational entropy of the mobile species. This coupling has been present in all previous implementations of the self-consistent mean field theory on which the present model is based.[31, 98] This relationship is more reminiscent of the original Flory-Huggins model in which the probabilities of the chain molecules are determined and the solvent fills the surrounding space, regardless of what may be the translational entropy of the solvent.[99] It is important to note that the two methods of incorporating excluded volume interactions become approximately equivalent in the limit of dense polymer phases in which the influence of a single chain molecule has a negligible effect on the bulk thermodynamic properties of the system. In special situations, in which there is both molecular crowding and relatively compact molecular ensembles, it is mathematically possible for this method of accounting for excluded volume interactions to predict total volume fractions of the protein in excess of 1. For positions in space where this is true, the original interpretation of the excluded volume energy density, $E_j(\mathbf{r})$, as the osmotic pressure $\pi(\mathbf{r})$ should be used to preserve the notion of incompressibility. However, for conditions used in this study, ensemble average volume fractions of protein did not come close to conditions for which this constraint would be necessary.

A review of Equation 2.7 (from the main text) reveals that two terms arise in the probability expression for excluded volume interactions. This is due to the acknowledgement that the probability appears twice in the excluded volume energy as it is implicitly treated in the free energy expression. The two appearances of $P_j(\alpha)$ yield two separate terms upon derivation. Physically, the first of these terms represents the excluded volume energy experienced by molecule j in conformation α, due to the presence of other Aβ molecules, $\neq j$. The second term expresses the excluded volume energy experienced by other molecules due to the presence of molecule j in

conformation α.

Choosing to interpret the excluded volume in this manner rather than simply as the osmotic pressure has profound consequences on the physics of the process being analyzed. This is easily demonstrated by comparing the properties of equilibrated Aβ molecules in isolation. We calculated the equilibrium properties for an isolated Aβ molecule at pH 8.0, 25°C and 150 mM NaCl using two separate methods. For the first method, we interpret the excluded volume interaction in the way described via Equation A.2, referred to as the E_j Method. For the second method, we interpret the excluded volume energy felt by molecule j in conformation α as $-\int \mathrm{d}^3\mathrm{r}\ \beta\pi(\mathbf{r})\phi_{A\beta,j}(\alpha;\mathbf{r})$, referred to as the π Method. Using the E_j Method, the radius of gyration and ensemble average end-to-end distance are found to be 1.07 nm and 2.07 nm, respectively; while for the π Method, these values are 1.84 nm and 4.32 nm. For both methods, we evaluated the spherically-averaged ensemble average volume fraction of Aβ as a function of distance from the molecule's center of mass as seen in Figure A.1:

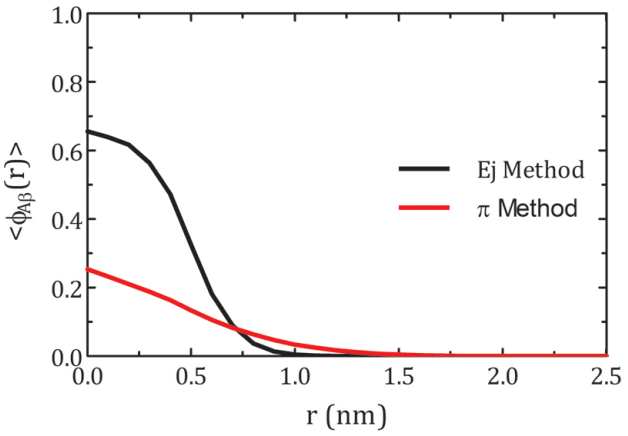

Figure A.1: Equilibrium spherically-averaged ensemble volume fraction of Aβ as a function of distance from the molecule's center of mass using the E_j Method (black) and the π Method (red).

Based on this information, the effect of using the π Method is clear and sub-

stantial. The unphysical self exclusion between intramolecular microstates results in an ensemble that is a significantly more diffuse statistical mechanical object. Unsurprisingly, the interactions of these very different objects, as occurs in a typical Aβ dimerization process, vary considerably in character. Furthermore, the radius of gyration predicted by the E_j Method is in much better agreement with those predicted by a fully-atomistic simulation study for an equilibrated $A\beta_{1-42}$ monomer in isolation.[100]

A.2 Probabilities of Configurations

We have calculated the average probability of configurations obtained from simulations of both isolated monomer and interacting monomers and plotted these values as a function of center of mass separation for the Aβ dimerization process at pH 8, 150 mM NaCl and 25°C, (*Condition 1*), Figure A.2.

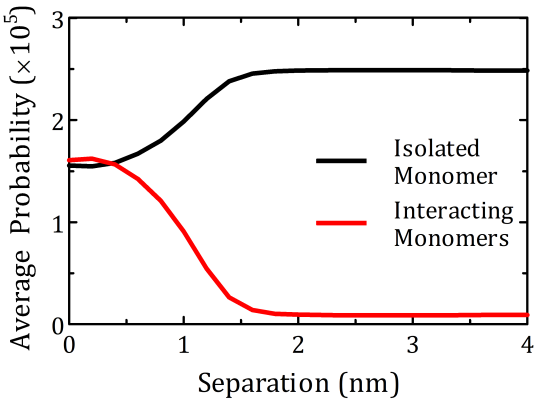

Figure A.2: Average probability of conformations obtained from simulations of both isolated monomer and interacting monomers as a function of center of mass separation for the Aβ dimerization process at pH 8.0, 25°C and 150 mM NaCl, (*Condition 1*).

At far separations (about 4 nm for *Condition 1*), the statistical thermodynamic model predicts much higher average probabilities for configurations obtained from isolated monomer simulations. For these separations, the Aβ molecules do not feel

each other's influence and have configurational ensembles that are indiscriminate from those of isolated monomers. Thus it is to be expected that the configurational properties that were sampled during the simulations of isolated monomers would be emphasized over those obtained from interacting monomers simulations. Also congruent with expectations, we observe that, at closer separations, the average probability of configurations from simulations of interacting monomers increases as that from isolated monomer simulations decreases. At the closest separations (<= 2 nm), the average probability of configurations obtained from the interacting monomers simulations finally overcomes the average probability of configurations obtained from isolated monomer simulations.

Qualitatively, this behavior provides support for the similarity between the way in which configurations are valued in simulation versus in our theoretical model. Additionally, it hints at the potential advantages of establishing a feedback loop between the two methodologies. That is, initializing simulations with those configurations determined most probabable by the model and then bolstering the ensemble with the resulting configurations obtained from those simulations. This is a development that we hope to incorporate in future realizations of the theoretical framework.